Vector Optical Rogue Waves in Mode-Locked Fibre Lasers

Hani Jassim Kbashi

Doctor of Philosophy

Aston University

March 2018

Aston University

Vector Optical Rogue Waves in Mode-Locked Fibre Lasers

Hani Jassim Kbashi

Doctor of Philosophy

March 2018

The project consists of an experimental characterisation of optical vector rogue wave (RW) events by using three different testbed fibre laser setups. The first testbed is a long cavity fibre laser (615 m). Here, we have demonstrated for the first time, a new type of vector resonance multimode instability that inherits some features of modulation and multimode instability. This instability leads to emerging different pulse laser regimes from longitudinal modes synchronization to different types of optical RW events. Using the same testbed fibre laser, we have also shown experimentally for the first time fibre twist-based chiral symmetry breaking. This leads to versatile laser dynamics tuneable from a periodic pulse similar mode-locked regime to chaotic oscillations which are revealed as a mechanism for the emergence of RW events. The observed optical RW events have been classified as fast optical RWs or slow optical RWs depending on the autocorrelation function of the experimental data. The classified optical RWs have been studied by collecting experimental data of a 19x19 grid of polarization positions through tuning both intra-cavity and pump polarization controllers.

The second testbed is a passively mode-locked fibre laser. Using this system, the control, appearance and disappearance of the soliton rain flow were demonstrated for the first time using a low range of pump power. Harmonics soliton rain, soliton fission and soliton-soliton interactions leading to the emergence of optical RWs have also been demonstrated in this experiment at a different pump power and intra-cavity birefringence. High harmonic (902 MHz) mode-locked fibre laser based on acoustic-optic effect has been realized in the same laser experiment.

In the third laser testbed experiment with, a stretched mode-locked fibre laser, vector bright-dark optical RWs were observed experimentally for the first time. These bright-dark RWs have formed in the laser cavity due to modulation instability at close pump power threshold or due to the polarization instability (incoherent coupling) at higher pump power.

Key Words: Optical rogue wave, mode-locked fibre laser, harmonic mode-locked fibre laser, polarization dynamics, and modulation instability.

List of Journals Publications:

1. S.A. Kolpakov, H. Kbashi, and S. V. Sergeyev, “Dynamics of Vector Rogue Waves in a Fibre Laser with a Ring Cavity,” *Optica* 3 (8), 870-875, 2016.
2. S. V. Sergeyev, H. Kbashi, N. Tarasov, Yu. Loiko, and S. A. Kolpakov, “Vector-Resonance-Multimode Instability,” *Physical Review Letters*, 118, 033904, 2017.
3. Hani Kbashi, Sergey V. Sergeyev, Chengbo Mou, Amos Martinez Garcia, Mohammed Al Araimi, Aleksei Rozhin, Stanislav Kolpakov, and Vladimir Kalashnikov, “Bright-Dark Rogue Waves,” *Annalen der Physik*, 530, 1700362, 2018.
4. S. V. Sergeyev, H. Kbashi, C. Mou, A. Martinez, S. Kolpakov, V. Kalashnikov, “Vector RWs driven by polarisation instabilities,” Nonlinear Guided Wave Optics A testbed for extreme waves, Chapter 9, *IOP Publishing, Bristol, UK*, 2017.
5. Maria Chernysheva, Mohammed Al Araimi, Hani Kbashi, Raz Arif, Sergey V. Sergeyev, and Aleksey Rozhin, “Isolator-free switchable uni- and bidirectional hybrid mode-locked erbium-doped fibre laser” *Optics Express,* 24(14), 15721-15729, 2016.

List of Conference Publications:

1. S. Kolpakov, H. Kbashi, and S. Sergeyev, “Slow Optical RWs in a Unidirectional Fibre Laser.” Lasers and Electro-Optics Conference, OSA Technical Digest (online), paper JW2A.56. (2016).
2. Hani Kbashi, Stanislav A. Kolpakov and Sergey V. Sergeyev, “Temporal Scaling of Optical RWs in Unidirectional Ring Fibre Laser,” Tu.B1.2, 18th International Conference on Transparent Optical Networks (ICTON), (2016).
3. S.A. Kolpakov, Hani Kbashi, Yu. Loiko, Nikita Tarasov, Sergey Sergeyev, “Generation of High-Frequency Harmonic Oscillations in Ring Resonator with High Q-factor,” IEEE, R1-30, International Conference Laser Optics, (2016).
4. Hani Kbashi, S. A. Kolpakov, Sergey Sergeyev, “Polarization Mapping of Fast Optical RWs,” IOP, Photon 16, (2016).
5. D. J. Little, H. Kbashi, S. A. Kolpakov, D. M. Kane and S. V. Sergeyev, “Changes in normalized permutation entropy during non-coherent pulsepulse interaction in the laser cavity,” 2017 European Conference on Lasers and Electro-Optics (CLEO) and European Quantum Electronics Conference, (Optical Society of America, 2017).
6. Sergey V. Sergeyev, Hani Kbashi, and Stanislav A. Kolpakov, “Rogue Waves and Mode-Locking Driven by Vector Resonance Multimode Instability,” Tu.A1.4, 19th International Conference on Transparent Optical Networks (ICTON), (2017).
7. S. A. Kolpakov, Hani Kbashi, and Sergey Sergeyev, “Rogue Waves Driven by Polarization Instabilities in a Long Ring Fibre Oscillator,” Proceedings Volume 10228, Nonlinear Optics and Applications, SPIE Optics + Optoelectronics (SPIE-EU), (2017).
8. Hani Kbashi, Stanislav Kolpakov, Amós Martinez, Chengbo Mou, Sergey V. Sergeyev, “Bright-dark RW in mode-locked fibre laser,” Proceedings Volume 10228, Nonlinear Optics and Applications, SPIE Optics + Optoelectronics(SPIE-EU), (2017).
9. Hani Kbashi, Mohamed Al-Araimi, Alex Rozhin, Sergey V. Sergeyev, “Vector rogue waves in a carbon nanotube mode-locked fiber laser,” *European Quantum Electronics Conference, EQEC 2017.* Optical Society of America, Vol. Part F81-EQEC 2017.

Acknowledgements

I would like to express my deep gratitude to my supervisors Dr. Sergey Sergeyev who was extremely supportive throughout my research programme as well as suggesting the project. Also, I would like to thank Dr. Stanislav Kolpakov and Dr. Amos Martinez Garcia for their support throughout my research period at Aston University.

My sincere gratitude goes to Aleksey Rozhin and Mohammed Al Araimi for suppling and fruitful discussions about carbon nanotube saturable absorbers (CNT-SAs).

My thanks are extended to the director of AIPT, Prof. Sergei Turitsyn and all the staff of AIPT, especially Dr. Nikita Tarasov and Dr. Srikanth Sugavanam for fruit spatiotemporal intensity dynamics discussions and Dr. Neil Gordon for useful discussion during the writing stage.

Other thanks and credits need to be extended to Leverhulme Trust (Grant ref: RPG-2014-304) for providing the financial funding to study the topic of my Ph.D. and all staff of Aston University who had a positive impact on my work.

I would like to express my extreme love and appreciation to my parents who supported and encouraged me through thick and thin. Finally, I would like to express my deepest gratitude to my wife and kids for long-suffering and patience with me.

Contents

Glossary of Terms and Symbols

AB	Akhmediev Breather
AF	Autocorrelation Functions
BDRW	Bright-Dark Rogue Wave
CSB	Chiral Symmetry Breaking
CNT	Carbon Nanotube
CW	Continuous wave
DOP	Degree of Polarization
EDFA	Erbium-doped fibre amplifiers
FORW	Fast Optical Rogue Wave
FML	Harmonic Mode-Locked
GVD	Group velocity dispersion
NPR	Nonlinear Polarization Rotation
NALM	Nonlinear Amplifier Loop Mirror
NLSE	Non-linear Schrodinger Equation
NPD	Normal Probability Distribution
MI	Modulation Instability
ML-EDFL	Mode-locked Erbium-doped fibre laser
PC1	Intra-Cavity Polarization Controller
PC2	Pump Polarization Controller
PDF	Probability Distribution Function
PI	Polarization Instability
PS	Peregrine Soliton
SA	Saturable Absorber
SBS	Stimulated Brillouin scattering
SESAM	Semiconductor saturable absorber mirror
SMF	Single mode fibres
SWCNT	Single-Wall Carbon Nanotube
SNR	Signal to Noise Ratio
SOP	State of Polarization
SORW	Slow Optical Rogue Wave
SWH	Significant Wave Height
RW	Rogue Wave
RF	Radio Frequency
VCSEL	Vertical-Cavity Surface-Emitting Lasers
VMMI	Vector Resonance Multimode Instability
WDM	Wavelength division multiplexing
σ	Standard Deviation

List of Figures

List of Charts and Tables

Chapter 1

Introduction and Literature Review of the Rogue Waves

1.1: Introduction

Rogue Waves (RWs) which also have been named freak waves, giant waves, extreme waves, monster waves, killer waves, abnormal waves and massive waves, are a spatiotemporal localized natural phenomenon that can appear to come from nowhere and disappear without a trace. Such waves exhibit a series of events with unexpectedly high amplitudes which are far beyond that of the background waves and which appear more frequently than would be expected. The first recorded description of RWs dates back to the mid-1960s when giant waves were reported by ship's captains and fishermen [1]. However, this phenomenon was first introduced to the scientific community in oceanography in the mid-1990s when the first RWs were detected in the North Sea by the Draupner platform [1, 2]. It was found that abnormally giant waves with great destructive power emerged unexpectedly from nowhere and disappeared very quickly without leaving a trace [3] (the waves are similar to the waves shown in Fig. 1.1 (a)). Such giant waves can reach very high amplitudes. In Fig. 1.1 (b), for instance, it reached a maximum wave height of 25.6m which is high compared to the significant wave height (SWH) of 12 m. Waves which are larger than the SWH, can sink ships during their voyage or cause damage as shown in Fig.1.1 (c). Such disasters from RWs can occur not only in the ocean or deep water, it has been observed also in seaside areas [4] where RWs can cause sudden flooding. These waves, despite being extremely rare can bring destruction for nature and civilization. RWs frequently have a negative impact on nature as well as presenting considerable danger as they are rare, unpredictable, appear suddenly and without warning, and can impact with

tremendous force. It is found that RWs natural hazards related to water flows cause remarkable losses every year in terms of human lives, ships, buildings, and infrastructure.

a) b) c)

Fig. 1.1: (a) RW events appeared unexpectedly, (b) very high amplitude RWs hit the ship, and (c) the RW impact on the ship [adapted from gCaptain newsletter].

During 19th, 20th and 21st centuries, many of RW events have been reported and recorded by many passengers in container ships, oil tankers and fishing boats; some of these disasters have been published in New Scientist Magazine [5]. It is believed that more than 22 super-carriers were lost between 1969-1994 in the Pacific and the Atlantic Ocean because of RWs and 525 have been death caused. Moreover, more than 12 collisions between ships and RWs were recorded in the Indian Ocean near the Agulhas Current and in front of the coasts of South Africa [6, 7]. Furthermore, more than 130 RW events have been reported during 2006–2010 [8]. Fig. 1.2 illustrates the up to date places where the RWs have collided with ships causing a number of fatalities. Up to now, no existing ships have escaped damage following a crash with a high destructive power RW which can reach up to 30 meters [9]. Furthermore, the tendency of RWs to dramatically appear from nowhere increases the level of the hazard and probability of collisions [10].

Despite these destructive effects, RWs may also have some beneficial applications. Most researchers interested in the RWs would like to reduce the probability of RWs emerging in the ocean to salvage ships and people life, but, on the other hands, some others have suggested the use of RW events (if they can be controlled) as defence weapons to protect countries against enemy ships [11].

Compared to other natural phenomena's such as tsunamis and the storms associated with typhoons, which can be predicted hours or sometimes days in advance [12], the oceanic RW events can suddenly appear from nowhere for a few seconds before hitting a ship, as has been confirmed by several observers. Indeed, this behaviour has made RWs difficult to investigate, difficult to predict and some uncertainty still remains on their fundamental origins. Many researchers have deduced that the probability of encountering RWs in the open ocean is much larger than would be expected from the normal distribution of wave-

amplitudes [13-15]. The mysteries behind such waves leads to difficulties in devising a systematic approach to studying their characteristics, including the originating or emergence mechanisms and the predictability of their appearance. However, some ways have been developed for an understanding of the origin of these giant waves such as, the probability of observation and the type of system which is able to generate them [12]. However, RWs are still elusive and intrinsically difficult to predict or monitor, we are a long way from achieving a full understanding and this problem merits further careful study in any physical system.

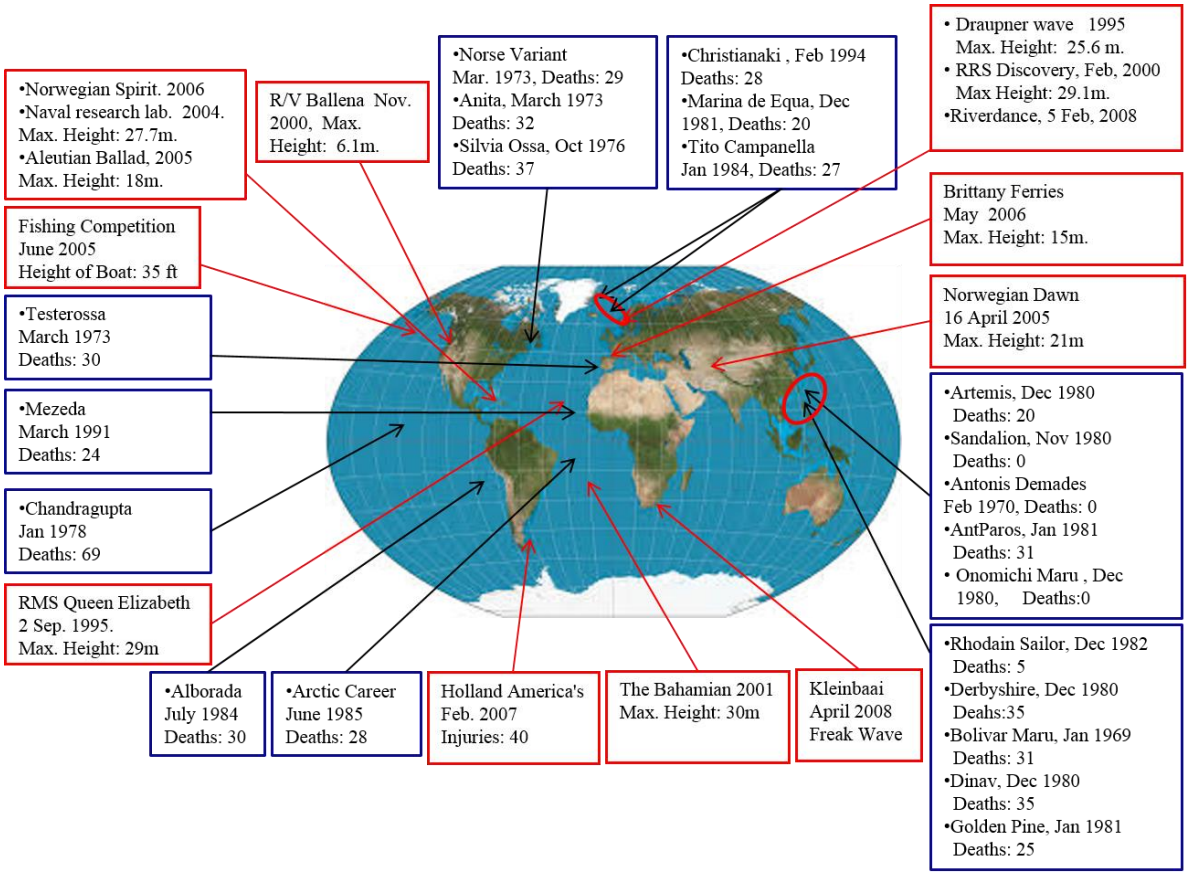

Fig 1.2: Statistics of RW collisions with super-carries since1968.

Nonlinear dynamics provides a good platform for the study of many interdisciplinary nonlinear natural phenomena such as in soliton waves. It has been shown that the nonlinear Schrodinger equation (NLSE) is suitable versatile and efficient theoretical framework that provides the basic features of generating and understanding the RWs. But, experimental difficulties are found in developing and understanding giant waves through collecting data, especially in the open ocean. Therefore, attempts to study this natural phenomenon has spread around other fields of science such as plasma physics, optics, and laser physics. The phenomenological and physical similarities between the RW events in the ocean system with optical systems as both share the same physical laws such as reflection, refraction, diffraction, interference and the interplay of linear and nonlinear effects as well

as the process of the modulation instability which is common in both systems have motivated researchers to study the RWs in optical systems in order to understand similar giant waves that appear and disappear without a trace in the ocean. The analogy between the ocean and optical systems has been studied in detail both theoretically or numerically. This has opened up the opportunity to study this natural phenomenon using testbed optical experiments which can be realised much more easily than ocean waves. In particular, optical fibre systems offer great advantages in studying these nonlinear dynamics that are related to a much faster field evolution and hence a high number of events can be recorded in a relatively short time.

Therefore, the aim of this thesis is an experimental contribution to understanding the mechanisms of optical RWs and their emergence in a testbed fibre laser. Indeed, the mechanism of the emergence of RW events is still under intense discussion [16, 17]. Understanding the physics of RWs is crucial not only to prevent ships from hazardous impacts in the ocean, but it can also offer a promising technique to generate localised intense and high output power generation in optical fibre for supercontinuum generation, and high power fibre laser applications. This chapter begins with a brief introduction to the definition of RWs that are commonly used in oceanography, followed by a brief historical account of documented observations of these unexpectedly emerged giant waves in the ocean. Then, RW identification properties and the criteria commonly used in their characterisation are discussed in section 1.2. In section 1.3, RWs in the various scientific systems are presented. Subsequently, different laser systems are presented in section 1.4. The motivation of this thesis, thesis outline and chapter conclusion are presented in section 1.5, 1.6 and 1.7 respectively.

1.2: Rogue Waves Identification

To identify the high intense events as RWs, the oceanography and optical specialist often uses three main features: First, the dynamics should manifest abnormality of unpredictable rare wave events. The ratio of the wave amplitude or SWH (distance from trough to crest) to the height of the average normal wave amplitude in a time series is measured [18], (i.e. the mean amplitude of the highest third of the waves) [19, 20]. According to this analysis, each event that has an amplitude greater than 2.2 times the SWH meets the extreme wave criterion as shown in Fig. 1.3 (a). Second, to classify the high intense events as RWs, these events should be rare transient waves that appear unexpectedly and disappear very fast without a trace [21, 22]. Third, the extreme events should arise more frequently than predicted from Gaussian or Rayleigh distributions. This means the events occur more frequently than calculated using the standard deviation (σ) of the normal probability distribution. Hence RW events have a long-tail (L shape) probability distribution function (PDF) as shown in Fig. 1.3 (b) and their probability significantly deviates from Gaussian or

Rayleigh distributions for normal ocean events or stochastic events respectively. Therefore, event waves that have an amplitude larger than the mean surface value plus 8 σ are considered RWs [18]. At present, it is more common to use the third criteria of the RWs where the RW's amplitude should exceed the standard deviation of the ocean's surface variations in more than eight times [20].

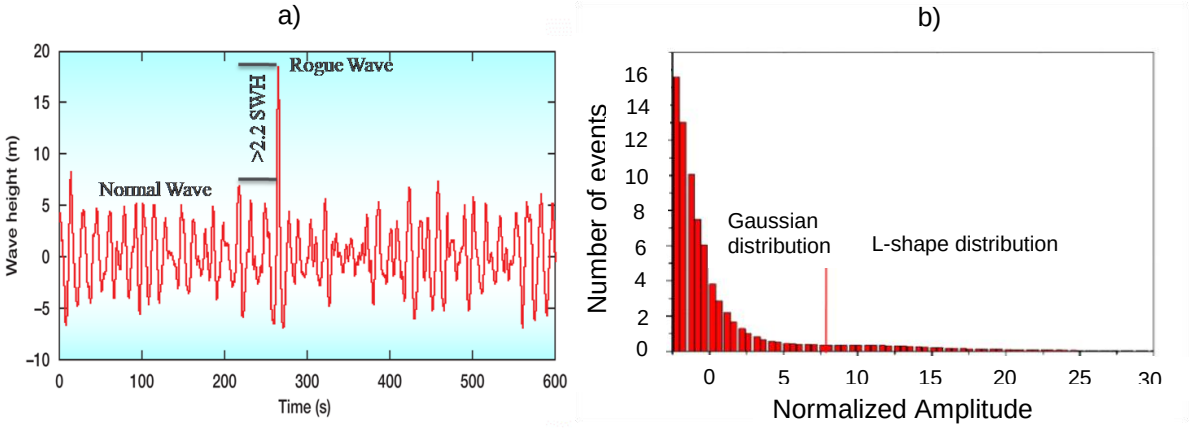

Fig. 1.3: (a) Wave height measurement as a function of recording time showing the RW at the Draupner oil; (b) PDF showing both Gaussian and L-shape distributions [adapted from https://physics.aps.org/articles/v2/86].

1.3: Rogue Wave events in Different Scientific Areas

Theoretically, rational space-time localized amplitude peaks were firstly described by Peregrine breather [23] shown in Fig. 1.4 (a), which are also called a Peregrine soliton through solving the self-focusing NLSE analytically in hydrodynamics. It was found that the amplitude peaks were formed due to the interaction of the nonlinearity and dispersion in the NLSE. After that, some other kinds of NLSE solutions have been presented considering the two solitons interaction for describing the time-periodic solitons named Ma or KM soliton breathers [24] as shown in Fig. 1.4 (b) which were later on classified as a mechanism of the RW events emergence. Thereafter, space periodic soliton named Akhmediev breathers (AB) [25] shown in Fig. 1.4 (c) have obtained which also classified as a mechanism of the RW emergence due to the soliton-soliton interaction in the space domain. Therefore, in the mathematical community, the term of RWs has been linked with these kinds of breathers or the exact rational solutions of partial differential equations of the NLSE.

a) Peregrine breather b) Ma breather c) Akhmediev breather

Fig. 1.4: The differences between (a) Peregrine soliton breather; (b) Ma soliton breather and (c) Akhmediev soliton breather [26].

Indeed, the difference between RW and breathers is that both Peregrine soliton and RW are nonlinear localized structures in both space and time. This is of fundamental significance because these are localized in both time and space, whereas breathers such as the Ma breather or Akhmediev breather are localized in only one domain. The Ma breather is localized in the time domain and the AB in the space domain. The existence of Peregrine was not observed experimentally in any physical system over three decades, until 2010 when it was observed in an optical fibre experiment [26]. Therefore, this confirmed that the Peregrine soliton is a formal prototypical that can describe the origination of RW events. Since then, RWs events have been observed and become a ubiquitous and hot topic in the study of localized waves in various scientific fields, from nonlinear optics [27], capillary waves [28], finance [29], nonlinear waveguide [30] and plasma waves [31], and these studies have supplied a better understanding of the general features and observation of RWs. However, RWs are not restricted to the ocean, and these have been found, for instance, in hydrodynamics in the form of turbulence, hurricanes, tsunamis, geosciences (earthquakes, floods, landslides), power grid and computer networks (black-outs), economics (financial markets), social sciences (distributions of populations), medical sciences (neuronal avalanches, epileptic seizure), material failures, environment and climate sciences (forest fires, evolution and competition of animal and plant species) [32].

As the RWs in different physical systems have the same underlying mechanism, then understanding the emergence and propagation of RWs in one system can be expected to strengthen the understanding in other systems. In addition, the important consequence of the RW studies is that predictability of the existence of such disaster waves, based on the observation of a suitable precursor, could be possible. The observation of precursors could be used to trigger a proper feedback signal before the emergence of the RW which then may allow the controlling or even suppression of such events. However, among these different systems, nonlinear optical systems offer an excellent platform for RW observation and emergence mechanism studies over a wide range of scales due to sharing similarities with ocean waves such as the interplay of linear and nonlinear effects. In particular, optical fibre experiments can provide relatively easily studying of RW emergence which can be beneficial in giving insight into the study of oceanic RWs [33]. Also, concerning the predictability of RWs is very difficult in oceanography system due to the scarcity of available data and measurements compared to the large and fast data collection capabilities in the testbed of a nonlinear optical system. For these reasons, it is important nowadays to study the mechanisms of the RW emergence in an optical system which is an analogy with the oceanography system. The common features between systems or objects of different nature and scale allow the researchers to use laboratory observations to understand the oceanic giant waves that are normally difficult to study in real life due to the dangerous conditions of the oceans. However, the collective efforts of experts from the various

scientific disciplines area are, indeed, providing fast progress in the RWs research field [34]. The optical systems, in particular, are revealing themselves as the most useful field in leading this progress [35]. Therefore, the laboratory physics studies allow a faster data accumulation from smaller scale processes than a real or direct study of the ocean RW evolution.

Therefore, in this thesis, we focus more on vector RW events emergence in optics and particularly in optical fibre laser experiments because of their similarities with ocean systems as well as having a high nonlinear dynamic and the capability to record a high amount of the data. The next section describes the observed optical RWs in different laser experiments.

1.4: Optical Rogue Wave Events in Different Laser Experimental Schematic

Due to the similarities with the ocean system, the studies of the RWs in the optical system have rapid growth over last decade. It can be used as a suitable testbed for the well-controlled investigation of such natural phenomena that cannot be easily investigated in their own environment. In addition, the emergence of the RW in optical systems could also affect the system's technological performance, for instance, it could damage the optical detector in the optical communication systems.

To mitigate the impact of the RWs on the natural life and technology, as well as move towards building the high power localized laser system, it is necessary to have a detailed understanding of the underlying optical RW mechanisms. Therefore, studying these RWs is of great importance for the design of localized output laser pulses.

However, in the optical system, it seems that the nonlinear dynamics are the suitable versatile and highly efficient theoretical frameworks that can be a success in developing the understanding the basic features of RW emergence [10, 36]. In particular, optical fibre systems offer great advantages in nonlinear dynamics which are related to faster field evolution and a higher number of events that can be recorded with relatively short time. Therefore, an extensively studied of the optical RW formation have been done experimentally and theoretically in fibre laser using comprise nonlinearly driven cavities [37], Raman fibre amplifiers and lasers [38, 39], pump-modulated fibre lasers [40]. In addition, it has been found that there was main role of gain active media and dissipative systems in the fibre laser to drive the instabilities in the RW formation such as Q-switching instability pulsating regimes [10], bunched chaotic multiple pulsing interaction [41], multiple soliton collisions [11], and the interaction with dispersive waves [42] which have been identified as a key mechanisms in the formation of RWs in the fibre laser. This has also stimulated research in diverse areas of nonlinear optics to study optical RW in other different optical systems included parametric amplifiers [43, 44], linear light propagation in multimode fibre

[45], optically injected semiconductor lasers [18], Ti:Sapphire mode-locked laser [46] and fibre lasers [47-49]. Therefore, optical systems have become an excellent playground for the studies the RW not only due to the similarity to the oceanic RWs as studied in the NLSE but, indeed, more generally for the study of large and statistically defined events. Thanks to such broader vision, the significance of the field has increased a lot, in particular, the general physical or dynamical concepts which can lead to the emergence RWs.

1.4.1: Optical Rogue Waves in Supercontinuum Fibre Lasers

The Concept of the optical RW has arisen in analogy with hydrodynamics to describe the extreme rare intense fluctuations events in the value of an optical field. Optical RW was first observed experimentally in high nonlinear microstructured optical fibres (Fig. 1.5 (a)) near to the threshold of the soliton fission supercontinuum generation [27]. These events have been studied numerically using the generalized NLSE which explained that optical RWs arise infrequently from initially smooth pulses due to power transfer seeded by small noise perturbation instabilities. However, in this experiment, a new real-time detection technique based on wavelength-time transformation has been used in the detection of such optical RW events. It was found that the output pulses from microstructure fibre are strongly dependent on the instabilities that are generated by the power level as shown in Fig. 1.5 (b-d). The PDF statistic histogram is shown in Fig. 1.5 (e1-e3) confirmed that the events that surpass the RW criteria increased dramatically with increasing the pump power level. The statistical analysis showed that the rare waves have long-tailed PDFs signature statistics characterization which are quite different from Gaussian statistics for the normal waves [21, 22, 27, 50-52]. Based on these statistics, optical specialists have added the PDF as third identity step for identification of the RWs [51, 52]. Then, this term has been generalized to describe many other processes in the field of optics because it provides a convenient platform for the study of RWs, with its fast field evolution and ease of parameter control. Since this initial study, the optical RWs have been observed in other supercontinuum fibre experiments using various external pump modulations from CW to picoseconds to study the evolution of statistical properties [27]. Moreover, optical RW statistics properties have also been studied using stochastic numerical simulations in the supercontinuum generated in two zero dispersion wavelengths photonic crystal fibre. The results of this study showed that the PDF statistics that were characterized in terms of peak power, wavelength and pulse duration strongly depend on the input pulse energy. They used the input pulse energy to control the dispersive wave generation which is the main source for optical RW emergence [51]. However, from most of the experiments, it was found that the strong power fluctuations which appeared and disappeared from nowhere resulted from soliton collisions inside the microstructure fibre [53]. Therefore, soliton collisions and soliton fission have

been recognized as the principal optical RW emergence mechanism in supercontinuum fibre laser systems. To observe such RWs, highly nonlinear fibre, as well as the high pump powers, are required. In contrast, chapter 3 presents the experimental observation of the emergence of optical RW by both soliton fission and soliton collision without the need of the high nonlinear fibre and also at low pump power.

Fig.1.5: (a) Experimental setup of the optical RWs observation in supercontinuum fibre; (b-d) the oscilloscope traces for three different pump power levels (increasing from top to bottom) and (e1-e3) the corresponding PDF histograms [27].

1.4.2: Optical Rogue Waves in Fibre Raman Laser

RW events have also been experimentally observed in the fibre Raman amplifier shown in Fig. 1-6 (a); it was found that a series of temporal extreme intensity spikes can be developed by raising the injected noise of the incoherent pump power that is applied using either a CW or a picosecond pulsed laser as shown in Fig 1.6 (b1, b2) respectively. Therefore, this external modulation instability played a key role in emergence of the spikes intensity and therefore this is classified as an optical RW emergence mechanism. The histograms of the PDF statistical analysis evolution of both Stokes and anti-Stokes bands showed their intensity had the L-shape signature typical of RW events [54]. There was good agreement with a numerical model that was developed using a coupled NLSE [55]. Optical RW has also been found in the Quasi-CW Raman fibre laser as shown in Fig. 1.7. It was found that, depending on the pump power; the laser could operate in different regimes from partial mode-locked to stochastic (Fig. 1.8) that surpass the criteria of the optical RW. The inset of Fig. 1.8 showed that the PDF histogram has developed gradually with increasing the pump

power and became broader with a high-intensity tail confirming the generation of optical RW events [39]. Such statistical properties have also been studied numerically for the same laser. This analysis confirms that the mechanism of the optical RW events was a turbulent-like four-wave mixing of numerous longitudinal generation modes [56].

Fig.1.6: (a) Experimental setup of the Raman amplifier; (b1) output intensity spikes in the case of CW launched with the pump power and (b2) in the case of the pulsed laser launched with the pump power [38].

Fig. 1.7: The experimental setup of the quasi-CW Raman fibre lasers [39].

Fig. 1.8: Temporal dynamics and PDFs (inset) for different pump powers a) 1.5 W of pump power, b) 2.0 W, c) 3.0 W, and d) 3.25 W. All traces presented show stochastic nature of the output emission [39].

1.4.3: Optical Rogue Waves in Fibre Brillouin Laser

Optical RW due to stimulated Brillouin scattering (SBS) in the fibre laser shown in Fig. 1.9 have also been observed experimentally. In this system, high intensity localized structures have been observed that are related to optical rogue events through their statistical behaviour. Highly-skewed intensity distributions are observed when the pump power is twice the laser threshold as shown in Fig. 1.10 (compare c, d with a, b). It was also confirmed that the emergence of these SBS-induced RWs is attributed to the interplay between laser operation and resonant Stokes orders and this has also been confirmed numerically [57].

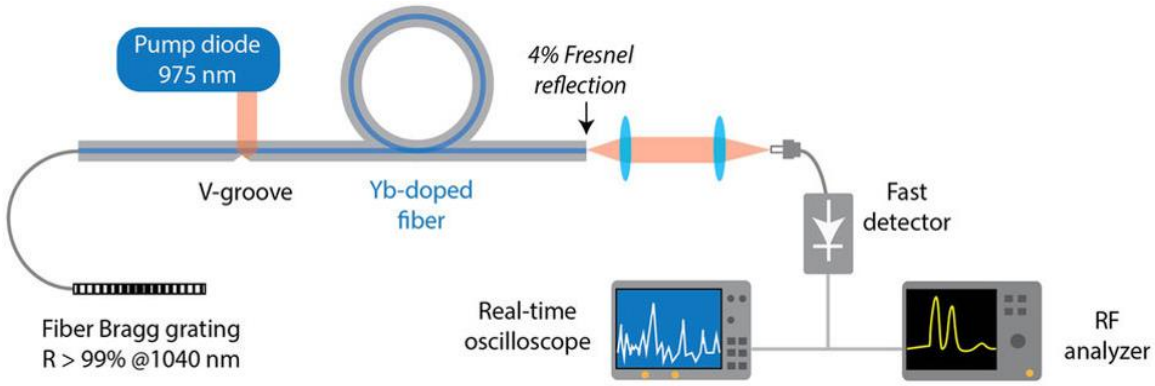

Figure 1.9: The experimental setup of the optical RW generation in SBS fibre laser [57].

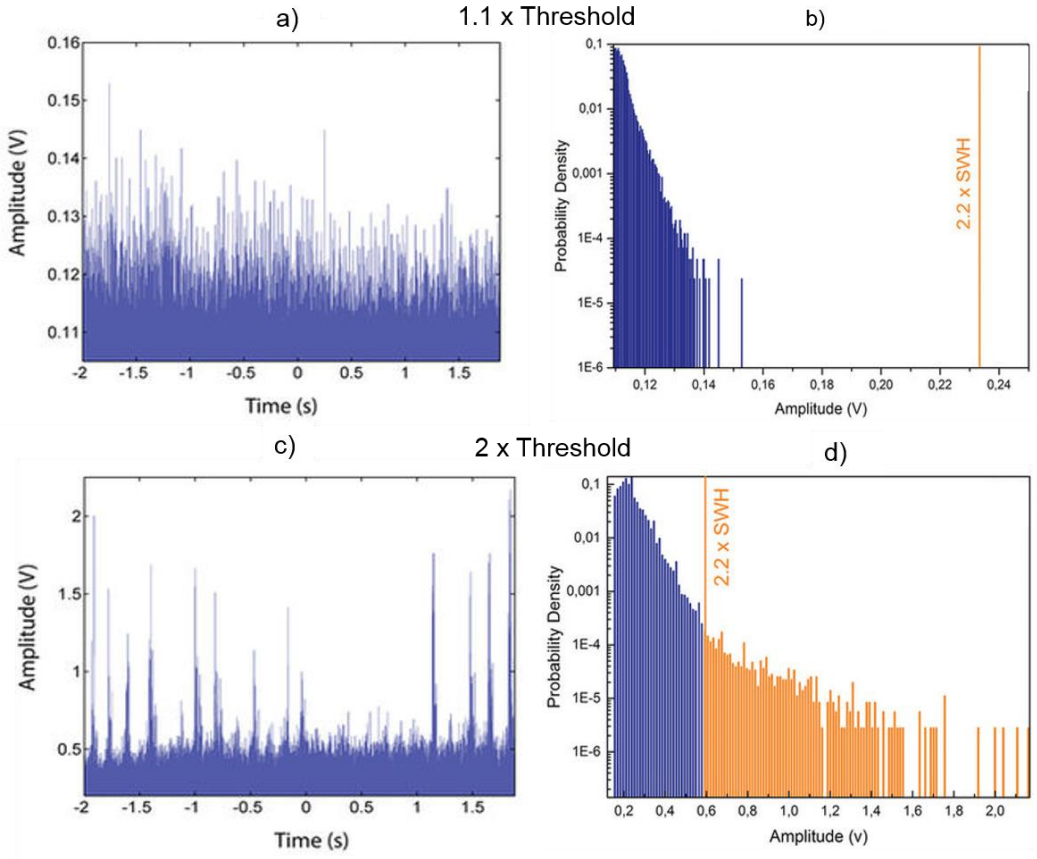

Fig. 1.10: Time traces and PDFs just above laser threshold (a, b) respectively and at twice the threshold (c, d) respectively showing the evolution to an unstable state with intensities exceeding the RW intensity i.e. with intensities exceeding twice of the SWH (solid vertical line) [57].

1.4.4: Optical Rogue Wave Events in Semiconductor Laser

Semiconductor lasers also have rich nonlinear dynamics which make them of interest for optical RW studies. Optical injection into vertical cavity surface-emitting lasers (VCSELs) has been investigated experimentally in the observations of deterministic optical RWs. It was found the optical RW appeared as results of the collision of chaotic pulses that developed due to the electrical pump injection. The long-tailed of the PDF of the pulse amplitude displays clear non-Gaussian features that confirm the RW character of the intensity pulsations. Simulations of a simple rate equation model showed a good qualitative agreement with the experimental results and provided a framework for understanding the observed RW events in semiconductor lasers as the result of a deterministic nonlinear process [18]. It was found that the PDF histogram shape is very sensitive to the injection current as it dramatically changed from Gaussian distribution (Fig 1.11 (a)) to the L-shape distribution (Fig. 1.11 (b)) confirming the emergence of the optical RWs in the output of the laser by just increasing the injection current from 0.972 mA to 0.976 mA (4μA). Furthermore, these events have been observed experimentally in a polarisation-resolved dynamic VCSEL. As such lasers are rich in the nonlinear dynamics, RWs have been observed not only in weak and strong chaotic dynamics but also in different dynamic regimes including a stable mode locking [58].

Fig.1.11: (a) PDF histogram shape of the optical injected VCSEL at (a) 0.972mA, (b) 0.976mA [18].

1.4.5: Optical Rogue Waves in Fibre Laser with Modulation Instability

Fibre lasers with nonlinear dynamics provide a suitable, versatile and highly efficient theoretical framework that can be successful in developing an understanding of the basic features of RWs. The fundamental nonlinear dynamics concepts range from modulation instability (MI) in both scalar [59] and vectorial [59] generated by coherent [59], incoherent [43, 60] or partially incoherent [43] pump source waves, to optical soliton dynamics [61, 62], and self-similarity [63]. Therefore, in this section, the MI role in the form of the different kinds

of breathers is presented as it was addressed in section 1.3 as the RW events emergence mechanism.

MI is a phenomenon that manifests itself in the dynamical exponential growth evolution of weak periodic perturbation in a continuous wave background. It is classified as one of the distinguished features of nonlinearity in the optical fibre; it is a result of striking consequence between the interplay of dispersion and high power Kerr effects. But, indeed, where it has been found that the generation of RWs is not restricted to this condition; it was extended to the normal dispersion regime where it predicted by Berkhoer and Zakharov by considering the extra degree of freedom due to the vectorial nature of light [64]. This MI has appeared in the form of spectral sidebands which exponential amplification in active medium with the expense of the pump power, but the dynamics are more complex and various scenarios of energy exchange between the spectral modes could be possible. Therefore, the exponential growth of weak perturbation of MI at the expense of continuous or quasi-continuous pump wave in the fibre laser can be either frequency-shifted signal wave or quantum noise (i.e., spontaneous MI). In the frequency domain, MI is equivalent to the four-photon parametric mixing process where two pump photons are annihilated to create a Stokes (signal) and anti-Stokes (idler) photon pair. Based on that, the links between spontaneous MI and their effect on the development of optical RW instabilities have been studied in optical fibre supercontinuum generation [27, 52] and in a high order of optical fibre nonlinearity [44]. It was found that the intrinsic characteristics of the RW existence are connected directly to the MI which require high nonlinearity to appear in the optical fibre. Therefore, fourth-order scalar MI nonlinear dynamics in the ultra-broadband optical wavelength converters have been numerically studied [44]. It was supported also the idea that, the spontaneous emergence of solitons and trapped radiation waves during the frequency conversion process, leading to significant blue and red spectral expansions. The statistical analysis of both blue and red spectral frequencies showed an L shape signature of the optical RW. The dynamics of rare pattern formation and intense localized optical peaks have also been studied in an optical system with optical feedback far from the modulation instability threshold. These intense optical peaks have been analysed numerically and experimentally by statistics and shown that their PDF have a long tail indicating the occurrence of rogue events [45].

1.4.6: Optical Rogue Wave Events in Mode-Locked Fibre Laser

The study of instabilities and RWs events in mode-locked fibre lasers is particularly desirable for two reasons. First, mode-locked fibre lasers offer a relatively simple system for complex nonlinear dynamics studies [65] as it has 1D guided-wave which extremely simplifies the theoretical analyses. Second, mode-locked fibre laser system architectures

at different wavelength operation have made such system unprecedentedly attractive to many practical applications [66, 67].

Compared to the bulk, passively mode-locked fibre lasers possess attractive features including compact size, no optical alignment, low cost, high beam quality, and the potential for environmentally stable operation. Therefore, passive mode-locked laser operation with multiple pulses per cavity round trip is also considered as a favoured way for optical RW mechanism investigations. Soto-Crespo et al. [47] have predicted numerically the generation of optical RW events in passively mode-locked lasers which were then observed experimentally by Lecaplain et al. in dissipative fibre laser systems [41]. But, these experiments required the conjunction of both anomalous dispersion and very high pumping power of up to 600mW as in the NPR shown in Fig. 1.12 (a) [41]. Due to the nonlinear dynamic, in addition to the soliton pulses and breathers, a bunch of pulses, can be formed in fibre laser (Fig. 1.12 (b)) which have long tail shape distribution with more than 2.2 of the SWH line compared to the classical distribution in the yellow line in Fig. 1.12 (c). The pulses in the regimes can have different speeds, amplitudes, and phases, which make the possibility of strong interactions and energy exchange between pulses which classified as a mechanism of optical RW events emergence.

Fig. 1.12: a) the experimental setup of the NPR, (b) Output pulse amplitude evolution over round trips showing the RW event; (c) PDF Histogram showing a large deviation above the classical distribution (yellow line) confirmed the RW event [41].

However, the multiple pulses, or dissipative solitons, can interact either weakly or strongly. The weak interaction processes are amplified by an active medium due to the endless recirculation of pulses in the cavity. This kind of interaction of multiple pulses can be through their tails, or through dispersive waves (soliton rain), made a bunch of pulses which have a time shorter than the cavity round trip time [47, 68]. Whereas, strong interactions are

affected by the cavity parameters, controlling these parameters can explore various pulsation behaviours like breathers. Also, optical RW events as intermittent regime have been studied experimentally in all normal dispersion passive mode-locked, fibre laser [49]. In addition to the studied of the mechanism were behind the emergence of the RW event in different laser experiments, there are also some other reviews that have been published on achieving a better understanding optical RW origination.

An overview of the breather, soliton dynamic and RW have been provided in a review by Dudley. This review discussed the optical systems have generated the extreme events with the consideration of defining a feature of RWs through statistical features such as long-tailed probability distributions [33, 69]. Roadmap on optical RWs and extreme events have introduced different original concepts in a single review article to stimulate and encourage further research of understanding RWs emergence [34]. Also, Dudley and co-author addressed a series of challenges and questions relating to understanding optical RW phenomena which were carried out mathematical, numerical and experimental studies in this field [69]. Moreover, a brief review of the RWs and their generating mechanisms in various physical fields have been reported by M. Onorato et al. in 2013 showing the RWs experiments laboratory performed in water basins and in different physical contexts [20].

1.5: Motivations of the Work

Despite the fact that there has been a considerable effort focused towards understanding the physical mechanisms behind the emergence of optical RW events, the complete picture still remains uncertain and unclear. This is because these waves appear from nowhere and disappear without trace as well as having statistical PDF that is completely different from that found regularly in normal waves. Hence, the general consensus is that one unique causative mechanism is unlikely. Based on that, the extreme events have been shown to emerge in many ways: from linear effects such as directional focusing or the random superposition of independent of wave trains to nonlinear effects that are associated with the increase of instabilities and noise to originate the localized wave structures. Also, to develop a capability to forecast RW events, it is necessary to build a testbed experiment that can be compared with previous observations. It would be very interesting to exploit such events in analogue physical systems where well-controlled experiments can be set up, producing large data set as well as allowing fast analysis of the data. The development of testbed experiments as illustrated in section 1-4 was based on the observation that many RW events in optical sciences have been described in scalar terms with the same universal statistical distributions. These statistics are characterized by the presence of RW events, which are associated with the properties of the tail ends of the corresponding distributions. From a theoretical point of view, it has been shown that vector RWs demonstrate a richer

structure than scalar ones, such as bright-dark RWs (BDRW) [70], dark RWs [55, 71], interactions between RWs and other nonlinear waves [70, 72] and four-petaled RWs [73] have been founded. Such studies indicate that nonlinear waves outcome in coupled NLSE systems is much more diverse than the ones in uncoupled systems.

This motivates us to propose a vector testbed fibre laser system which takes into account the laser dynamic instabilities, particularly natural vector instability (polarization) that have been ignored in most of the previous experimental studies. The scope of this thesis is to provide a simply accessible testbed fibre laser system for exploring in a well-controlled system the dynamics of the optical RW events. This could help to study as much as possible of the optical RW events mechanisms, it means, rather than to build one experiment to study only one or two events, we build fibre laser experiments that can observe most of the RW events. Therefore, the outcomes of this testbed experimental study can be beneficial towards predicting and controlling the appearance of optical RWs in optical systems. In addition, understanding the physics behind the RWs emergence is important not only to prevent the particular system from hazardous effects, but it can also provide a promising method for localized (time-space or both time and space) high power laser generation. Therefore, the main objective of this dissertation is an exploration of optical RW emergence mechanisms.

1.6: Thesis Organization

This thesis provides a testbed experiential system to study the optical RW emergence mechanisms in an optical fibre based on different instabilities. Five chapters are organized as follows and presented schematically in Fig. 1.13.

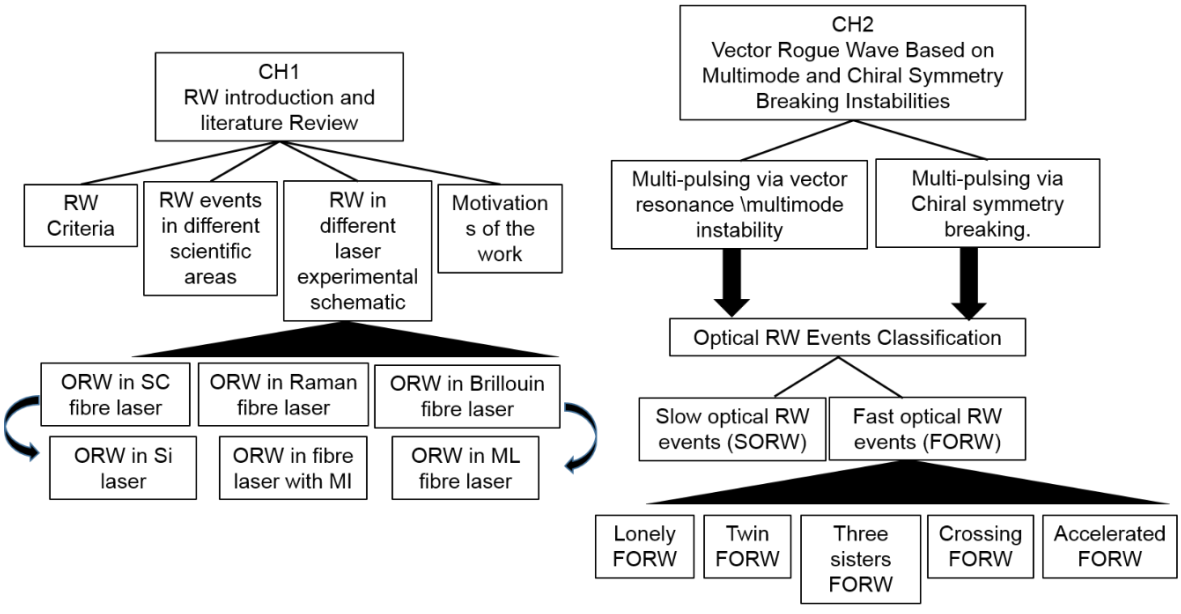

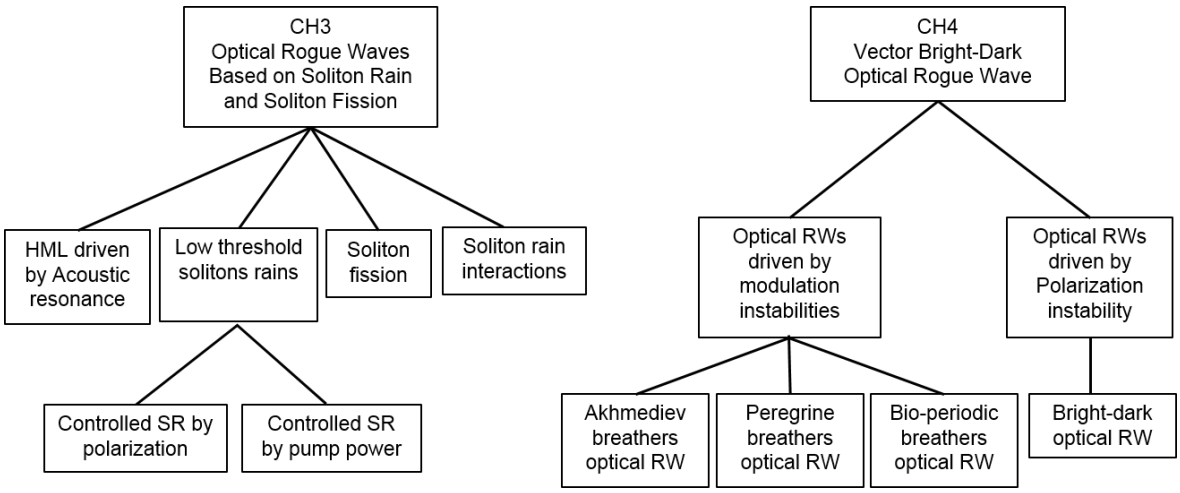

Fig. 1.13: Display the organization of thesis.

We begin with a brief fundamental definition and concepts of RW overview in Chapter 1, focussing on RW emergence in the ocean and disaster effect. We then discuss the statistical properties and the criteria used for identification of extreme events as RWs, followed by their emergence in different physical systems. RWs in the different optical schematic system are discussed showing different emergence mechanisms. Finally, motivation of the work, thesis organization and chapter conclusion are presented.

Chapter 2 is devoted to demonstrating, experimentally, a new type of the low threshold vector resonance multimode instability (VMMI) which inherits features of multimode and modulation instabilities. The instabilities are driven by in-cavity birefringence that is adjusted using an in-cavity polarization controller (PC) in a long fibre laser. Using the same fibre laser, we also demonstrate another vector instability named chiral symmetry breaking (CSB) which drives the laser dynamic by a fibre twist which is induced by an in-cavity PC. We show that both of VMMI and CSB can drive the laser system from periodic longitudinal modes synchronization to quasiperiodic motion and further to the chaotic pulse behaviour satisfying the optical RWs criteria.

The experimental classification of slow and fast optical RWs which were observed using the long laser system as well as different kinds of fast optical RW such as lonely, twin and three sisters are also discussed in this chapter. Finally, the generation mechanisms of optical RWs using the long fibre laser are evaluated based on pulse-pulse interactions.

Chapter 3 presents both soliton rain and soliton fission that are intriguing nonlinear dynamics mechanisms for optical RWs emergence. It is experimentally observed for the first time that optical RWs can emerge as the result of soliton interactions in anomalous passive mode-locked fibre laser at a low threshold of pump power. High harmonic mode-locked fibre laser (~1GHz) also obtained and demonstrated at the beginning of chapter 3. The variation of harmonic soliton rain, soliton fission and soliton interactions as mechanisms

for optical RWs emergence on varying the initial parameters are also observed and discussed in this chapter.

Chapter 4 reveals the importance of the state of polarization as an additional degree of freedom in a fibre laser. It provides for the first time an experimental observation of BDRW in a stretched mode-locked fibre laser. It found that the BDRW can emerge as the result of either MI or polarization instability (PI) or with the contribution of both of them due to the coherent coupling between the polarization components of the light pulse within the laser cavity that results in such complex instabilities. Finally, Chapter 5 draws conclusions from the entire thesis and presents a summary of the results.

1.7 Conclusion

This chapter introduced fundamental concepts of the optical RWs. In the beginning, definition and the concepts of RWs and its identification were introduced. Then, RWs in different scientific fields and also in the optical experimental schematic are presented, as in illustrated in flowcharts 1.1 and 1.2 respectively, showing the mechanism behind the emergence of such rare events. From that, it concludes that mode-locked fibre lasers are the most promising framework for success in developing an understanding of the optical RW emergence.

Flowchart 1.1: RW observation in different scientific areas.

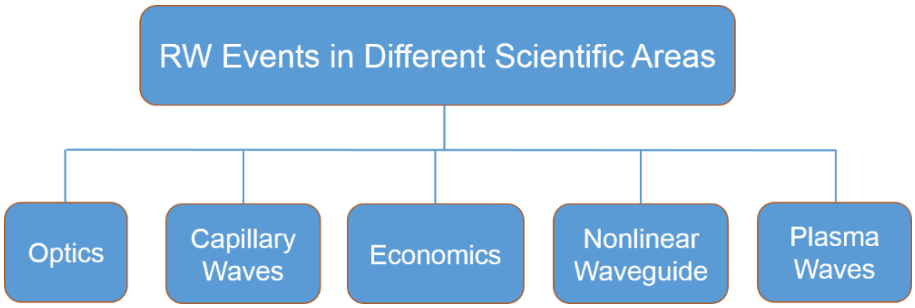

Flowchart 1.2: Optical RW observation in different fibre laser schematic.

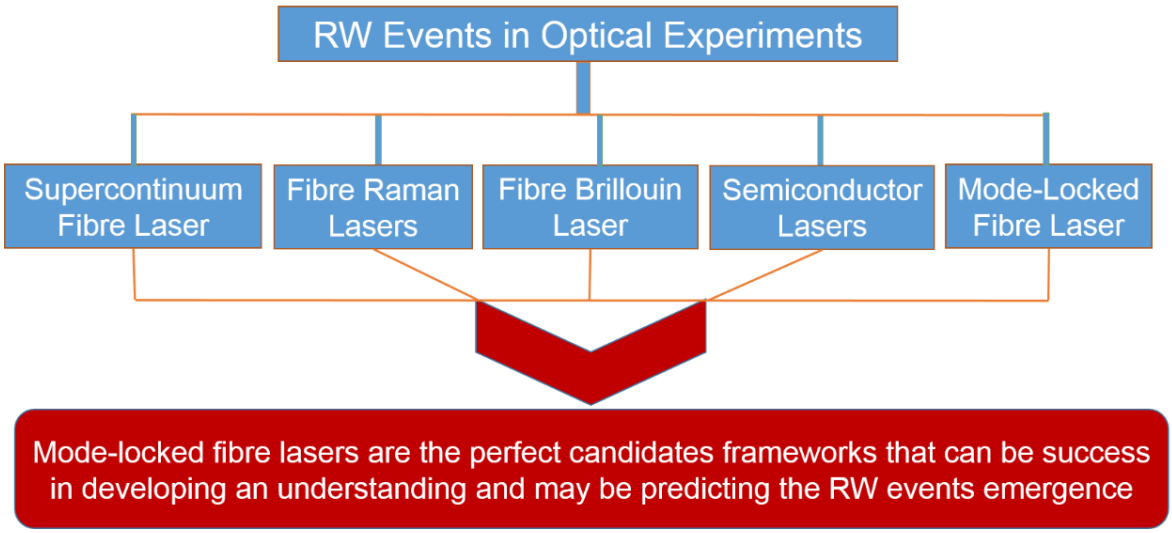

Chapter 2

Vector Optical Rogue Wave Based on Resonance Multimode and Chiral Symmetry Breaking Instabilities

2.1: Introduction

In this chapter, a testbed fibre laser design is proposed to address the challenge of investigation the vector nature of the laser dynamics. We will experimentally demonstrate a new type of vector resonance multimode instability that inherits some features of modulation and multimode instability (VMMI). Using the proposed fibre laser, we have justified for the first time that an increased in-cavity birefringence strength causes spatial modulation of the two orthogonal states of polarization (SOP) with a period equal to the beat length and so leads to different level of coherent coupling (synchronization) depending on the birefringence strength. We have shown that by tuning the interaction of two orthogonal SOPs of the laser cavity, we obtain polarization instability as a feature of MI leading to emergence of different pulse laser regimes including longitudinal mode synchronization and different types of optical RW events.

Using the same testbed fibre laser, we have also demonstrated experimentally for the first time that fibre twist-based chiral symmetry breaking (CSB) leads to a versatile laser dynamics which can be tuned to give periodic pulses similar to the mode-locked regime, harmonic, multi-pulse, and chaotic oscillations. This shows that this is a mechanism for the emergence of RW events and these can be varied depending on the coherent coupling between the left and right polarization modes.

For the optical RW events emergence mechanism, we provide evidence of optical RWs that can emerge due to either multimode instability or chiral symmetry breaking at a pump power of only 18.4 mW which is close to the lasing threshold of 16 mW. This power is much less than the 600 mW that has been demonstrated previously in NPR [74]. Furthermore, we have observed two different classifications of optical RW pattern; fast optical RW (FORW) and slow optical RW (SORW). Both emerge due to the incoherent coupling of polarization components in the laser cavity, but for FORW this coupling is in the form of pulse-pulse interaction; while for SORW it is in the form of attractors. Both the FORW and SORW have been studied by collecting experimental data over a matrix of 19x19 polarization positions (polarization map) through tuning both the intra-cavity and pump birefringence. In addition to the SORW and FORW, different types of the FORW have also observed through polarization mapping including lonely, twins, three sisters and crossing pulses.

The organisation of this chapter is as follows: in section 2.2, we describe the testbed laser experiment and its characterization showing the modulation of the SOP as a feature of MI. The multi-pulsing laser regimes based on both VMMI and CSB instabilities are presented in sections 2.3 and 2.4 respectively. In section 2.5, we discuss optical RW classification as either SORW or FORW based on the characteristic time of the events. This is calculated from the autocorrelation function (AF) of the experimental results. More details of the SORW and FORW are presented in sections 2.6 and 2.7 respectively. Finally, we make some conclusions on the experimental results that are concluded and shown in flow and pie charts in section 2.7.

2.2: The Testbed Experimental Laser Setup

The testbed fibre laser system is based on a 615 m long unidirectional ring cavity oscillator as illustrated in Fig. 2.1.

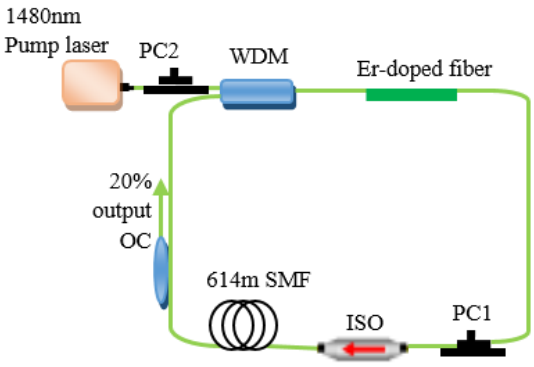

Fig. 2.1: Schematic of the long cavity (615m) testbed fibre ring laser. WDM: wavelength Division multiplexing; PC: polarization controller; ISO: optical isolator and OC: output coupler

In contrast with the mode-locking schemes based on nonlinear polarization rotation, only one in-line cavity polarization controller (PC1) was placed inside the cavity. The second polarization controller (PC2), was used to control the SOP of the pump wave. The angles

of the polarization controllers were measured relative to the vertical position. The whole cavity was assembled with 1 m of Er^{3+} doped fibre Liekki Er80-8/125 ($\beta_{2=}$+59 ps^2/km at 1550nm) and 614 m of single mode fibre SMF-28 (β_2=-21 ps^2/km). The polarization insensitive optical isolator (ISO) was used to ensure unidirectional lasing and had an attenuation of 51 dB. The 80/20 fibre coupler was used to sample a portion of the signal wave. The cavity was pumped via a 1480/1550 WDM using a 1480 nm laser diode which had a built-in isolator. The supplied pump power was measured after the pump polarization controller (PC2) and the wavelength division multiplexing (WDM) but before the Er^{3+} doped active fibre. The output signal of this experiment was detected using an InGaAs UPD-15-IR-2-FC detector with a bandwidth of 17 GHz connected to a 2.5 GHz sampling oscilloscope (Tektronix DPO7254). The oscilloscope has the built-in option of a variable electronic filter for the incoming signal. The oscilloscope was set on 10 Gs/s trace points and 100 ps/pt resolution. For a trace length of 5 ms, this yielded a total of 50x10^6 points and these were processed to detect the RW patterns. An optical spectrum analyser (Yokogawa AQ6317B) with 0.02 nm resolution and an RF signal analyser (FSV signal analyser Rohde Schwarz; 10 Hz-13.6 GHz) were used to record the laser optical spectrum and radio frequency (RF) spectrum respectively. The SOP and the birefringence strength that drives the output to different laser dynamics were studied using an in-line polarimeter (Thorlabs IPM5300). A set of 16 frames with 1024 samples in each frame and 1 µs resolution were collected over an interval of 1 ms (25 – 25000 round trips) in each measurement of the polarization. The data was analysed to measure the normalized Stokes parameters S_1, S_2, S_3 and the degree of polarization (DOP). These parameters are related to the output powers of two perpendicular linearly polarized polarization states $|\mu|^2$ and $|\nu|^2$, and the phase difference between them $\Delta\varphi$ as follows:

$$S_1 = |u|^2 - |v|^2,\ S_2 = 2|u||v|\cos\Delta\varphi,\ S_3 = 2|u||v|\sin\Delta\varphi, \qquad \text{----------2.1}$$

$$s_i = \frac{S_i}{\sqrt{S_1^2 + S_2^2 + S_3^2}}, \quad DOP = \frac{\sqrt{S_1^2 + S_2^2 + S_3^2}}{S_0}, (i = 1,2,3)$$

It was found that the RF spectrum of the output signal has three frequencies as shown in Fig. 2.2 (a). The central peak (325 KHz) corresponds to the round trip frequency which is linked to the laser cavity length; the two satellites labelled as polarization are related to in-cavity birefringence-mediated instabilities. The frequency of this modulation depends on the induced birefringence strength (coherent coupling) in the cavity and this can be adjusted by varying PC1. In addition, there are; another two smaller satellites which are amplified in the right insert. These appear because of pump power inform of modulation instability in the

long ring cavity. The frequency offset of these smaller satellites depends on the pump power as illustrated in Fig. 2.2 (b). The left insert in Fig. 2.2 (a) shows the output power vs pump power with a lasing threshold of 16 mW.

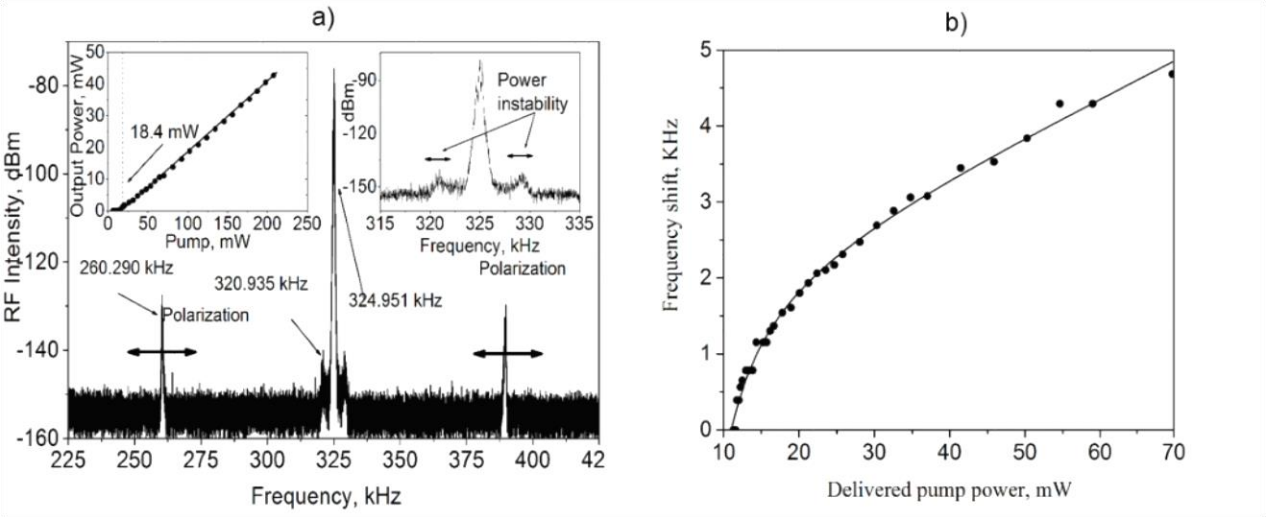

Fig. 2.2: a) The output RF spectrum of the testbed fibre laser; in left insert power versus pump; in right insert the amplified central RF peak with satellites due to power instability; b) power instability satellites distance from the RF central line as a function of the pump power.

2.3: Multi-pulsing Via Vector Resonance Multimode Instability

Using the experimental system discussed in section 2.2, we demonstrated experimentally, for the first time, several new types of low threshold vector resonance multimode instability [75]. These instabilities inherit features of both multimode and modulation instabilities in the form of the polarization satellites illustrated in Fig. 2.2. We found that the pump power at the first lasing threshold for the CW regime was 16 mW and this was followed by a second threshold for multimode instability at 18.4 mW. At this pump power, we observed that the laser can operate in different output laser regimes by changing the laser cavity birefringence (PC1) as shown in Fig. 2.3. At this threshold, a large number of longitudinal modes are excited without synchronization (incoherent coupling) and this leads the laser cavity to emit pulses in a chaotic fashion with few pulses amplitude surpass the RW threshold (red-dotted) as shown in Fig. 2.3 (a). The RW criteria which illustrated in chapter 1 has been used to identify the observed optical RW. However, the periodical amplitudes that are related to the round trip period have excluded in view of predictable nature of the optical RW emergence. To enable multimode instability, we need to modulate the SOP of the lasing signal at the period of the beat length by adjusting the in-cavity birefringence (PC1) and the SOP of the pump power wave (PC2). By adjusting these parameters, we show that the output laser regime could be tuned from chaotic emission to periodic pulses similar to the mode-locked regime which is illustrated in Fig. 2.3 (a1-d1). These output laser regimes are based on the synchronization of the two orthogonal states of polarisation producing resonance

matching between the beat (polarization satellites frequency) and cavity lengths (central frequency line). As can be deduced from Fig. 2-3 (a1-d1), the chaotic operation regime is due to completely incoherent coupling, whereas adjustment to give coherent coupling results in regime stabilization initially towards a less chaotic state and then to an ordered multi-pulsing regime as in Fig. 2.3 (b1, c1). In the case of the partial coherent coupling, the polarization satellites move closer to the central frequency line (Fig. 2.3 (b2, c2)). Periodic single pulsing, similar to mode-locking (Fig. 2.3 (d1)), is obtained in the case where the polarization satellites match the main central laser line (Fig. 2.3 (d2)). These single pulses propagate in the laser cavity due to modes synchronization in the form of coherent coupling between the two orthogonal polarizations. The pulse train in Fig. 2.3 (d1) has a pulse width of 40 ns, which is much less than the round trip time of 3 µs. This indicates the excitation of many longitudinal modes along with their relative phase synchronization.

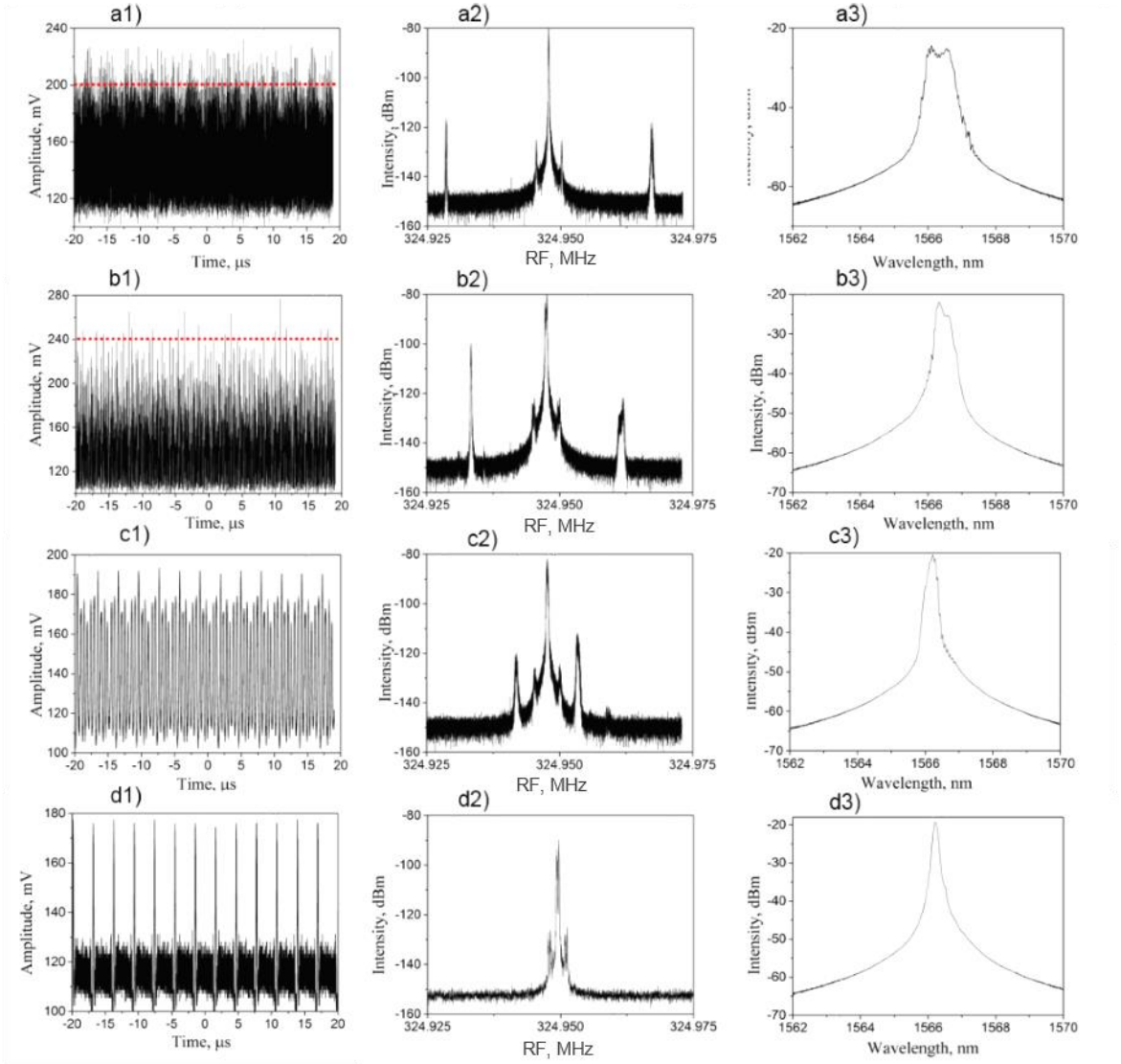

Fig.2.3: The oscilloscope traces (a1-d1) corresponding RF spectrum (a2-d2) and optical spectra (a3-d3) for different setting of the PC1: a1, a2, a3) θ_1=-80^0; b1, b2, b3) θ_1=-78^0; c1, c2, c3) θ_1=-74^0; d1, d2, d3) θ_1=-69^0.

The fundamental frequency seen in the RF spectra was 325.2 kHz and this matches the cavity round trip length. The RF spectrum evolved as in-cavity polarization controller was adjusted and the peak better resolved in the case of the 1000th harmonic, i.e. a pulse frequency of 325.2 MHz (Fig. 2.3 (a2-d2)). As shown in Fig. 2.3 (a2-d2), switching between the different laser regimes was achieved by adjusting the polarization control over a very narrow margin where the birefringence-dependent satellites neighbouring the 325.2 MHz main peak were visible. The orientations of the paddles of the polarization controllers (PC1 and PC2) were measured with respect to the vertical position. The paddle of PC2 was set at θ_2=-59^0 whereas paddle of PC1 was set at four different positions, namely θ_1=-80^0,-78^0,-74^0,-69^0. The corresponding optical spectra are shown in Fig. 2.3 (a3-d3) evolve from a twin-peaked spectrum (Fig. 2.3 (a3)), due to the incoherent coupling of chaotic pulses, to a single wavelength centred at 1565nm. This is because the dynamics are changing from the case where there is a mismatch between the beat length and the cavity length to the case where these are matching.

The results on the polarization dynamics shown in Fig. 2.4 (a, b) support this conclusion. The polarization results are shown in Fig.2-4 (a). The size of the spot on the Poincaré sphere indicates the deviation from the resonance position of the N-fold beat length, i.e. decreasing this size by adjusting θ_1 moves the N-fold beat length towards resonance with the cavity length. When an arc forms in the Poincaré sphere as shown in Fig. 2.4 (a), this demonstrates that the beat length deviates far from any resonance length resulting in a chaotic pulse regime. The variation of the output power and polarization phase difference are shown in Fig. 2.4 (b and c) respectively. There are only small oscillations in the output power S_0 and the phase difference$\Delta\varphi$. The DOP is relatively small at around 40%. These results indicate that in this regime, with the PC1 setting at θ_1=-80^0, the laser dynamics is fast with a time scale less than 1 μs. Further tuning of PC1 suppresses this fast dynamics. The constant output and high (over 80%) DOP for the case when θ_1=69^0 in Fig. 2.4 (b) indicates stable mode locking accompanied with stable SOP locking (i.e. matching the N-fold beat length to the cavity length). We have found that modulation and multimode instabilities are the main mechanisms that drive spontaneous spatial and temporal pattern formation in a vast number of nonlinear systems with complex chaotic regimes which satisfied the criteria of the RW events. Apart from the interest in laser physics for unlocking tunability and stability of dynamic regimes, the proposed mechanism of the vector resonance multimode instability can be of fundamental interest for nonlinear dynamics of various distributed systems.

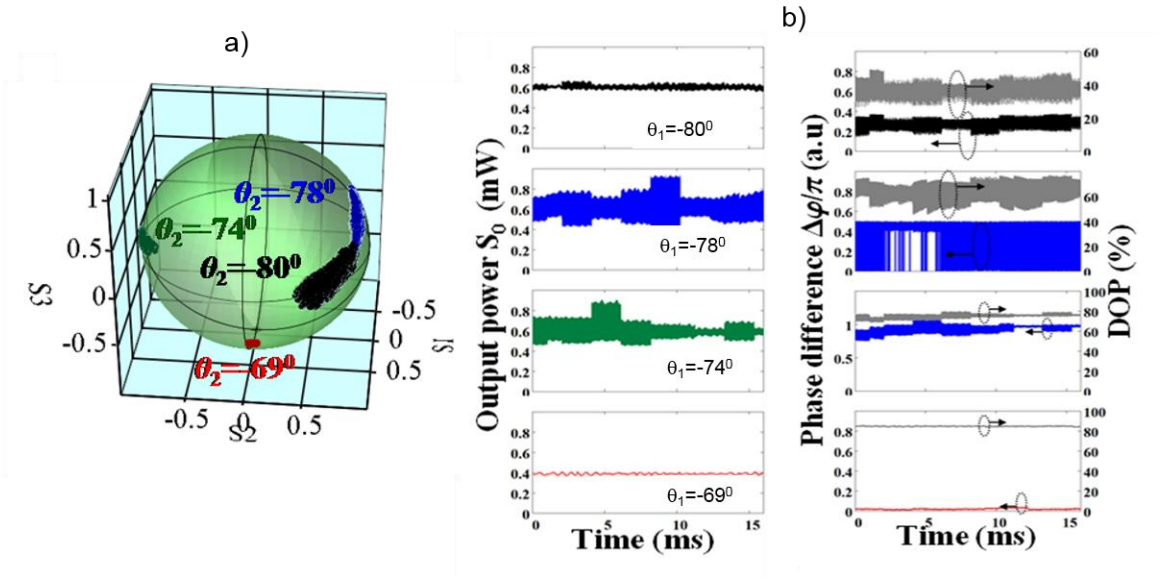

Fig. 2.4: (a) The map of the SOP on the Poincare sphere; (b) output power (So) and the corresponding phase difference between linearly polarized modes(c left) and (c right) DOP for different setting of the PC1: from the top θ_1=-80⁰, -78⁰; -74⁰; -69⁰.

This experimental result has been confirmed theoretically by Sergeyev et al. [75] and has also been validated experimentally using a fibre laser based on high birefringence (HiBi) fibre as shown in Fig. 2.5. The beat length is around 3 mm, and this is much less than the single mode fibres. The experimental setup with HiBi fibre is slightly different from that described in section 2.2 and had a total cavity length of 20 m which includes 10 m of the HiBi fibre and the system was pumped at 980 nm.

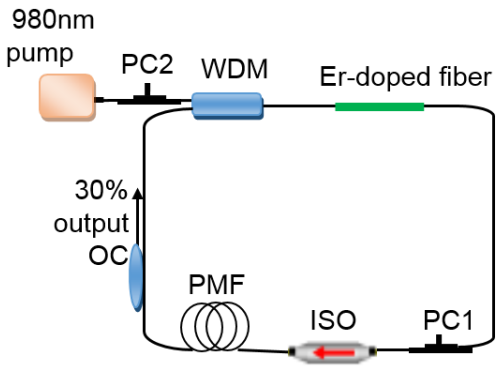

Fig. 2.5: The Experimental setup of the HiBi experiment. WDM: wavelength Division multiplexing; PC: polarization controller; ISO: optical isolator; PMF: polarization maintaining fibre; and OC: output coupler.

We have justified, experimentally, that increasing the in-cavity birefringence strength by using HiBi fibre inside a laser cavity without any saturable absorber element, also causes spatial modulation of the SOP of the in-cavity lasing field so that it can synchronise with the period of the cavity round trip to generate different regimes from a periodic longitudinal mode similar to mode-locked to chaotic regimes.

The cavity can self-mode-lock when the pump power is set to 35 mW which is slightly beyond the laser threshold (~25 mW). Different output laser regimes were observed using the HiBi laser configuration as illustrated in Fig. 2.6. As in previous section, we obtained several different regimes as shown in Fig. 2.6 (a) including single periodic pulse mode, multi-pulsing and chaotic pulses. Switching between the laser regimes was done by changing the laser cavity birefringence through tuning PC1. By tuning the laser cavity birefringence, we induced polarization multimode instability (PMMI) inside the laser cavity which was then further amplified by the gain fibre section in the cavity. The physical principle behind the regime where there is a single pulse per laser cavity round trip emission as in Fig. 2.6 (a) is also coherent mode coupling between the two orthogonal polarization modes. This regime appeared when PC1 was set at 40^0. Thus, if the light is coupled to both fundamental polarization modes of the HiBi fibre and the beat length is matched to the cavity length, the SOP will be repeated after each distance of the beat length. Indeed, if there is a small difference between the beat length and the cavity length, the laser emits an ordered multi-pulses output as shown when PC1 is set at 45^0 (Fig. 2.6 (b1)); while in the high difference case, the laser emits a chaotic regime as in the cases of the PC1 at 48^0 and 50^0 shown in Fig. 2.6 (c1, d1 respectively). This is the case of out of resonance (incoherent coupling) between the modulated SOP with the beat and cavity lengths and this leads to the emergence of more complex regimes.

We found that there was no sign of the emergence of optical RWs in these complex regimes; ORW events were found at higher pump powers (90 mW) in the HiBi laser experiments. Compared with the RF spectra in Fig. 2.3 (a2-d2), the polarization satellites on the RF spectrum in Fig. 2.6 disappeared during the HiBi laser experiment due to this mode coupling which is related to the modulated SOP, beat and cavity lengths. Partial and uncoupled polarization modes have been further investigated by bending the HiBi and this led to re-appearance of the polarization satellites as shown in Fig. 2.6 (c2 and d2). The optical spectrum traces for all these regimes is illustrated in Fig. 2.6 (a3-d3). This confirmed that the mode coupling between the two orthogonal states of polarization give an “M-shaped” optical spectrum (Fig. 2.6 (a3)). The two peaks wavelengths are 1568.5 nm and 1569.87. So, the difference between them is 1.37 nm. The calculated beat length (L_b) for this distance between the two laser lines is equal to about 8.7 mm; this implies that the difference between the two orthogonal polarization refractive indices is equal to 1.79×10^{-4}. Also, as seen in Fig. 2.6 (b3-c3), the optical spectrum at the laser output of other laser regimes appears to have a similar shape to the many soliton lasers with Kelly sidebands clearly visible and with some interesting features which reveal that the two orthogonal polarizations are still coupled suggesting that this is a multi-wavelength soliton emission. But, at high intra-cavity birefringence (chaotic laser regime), this laser system is influenced to generate

spectral filtering like a frequency comb as illustrated in Fig. 2.6 (c3, d3). It also found that the characteristic of these combs can be controlled by both PCs and the pump power.

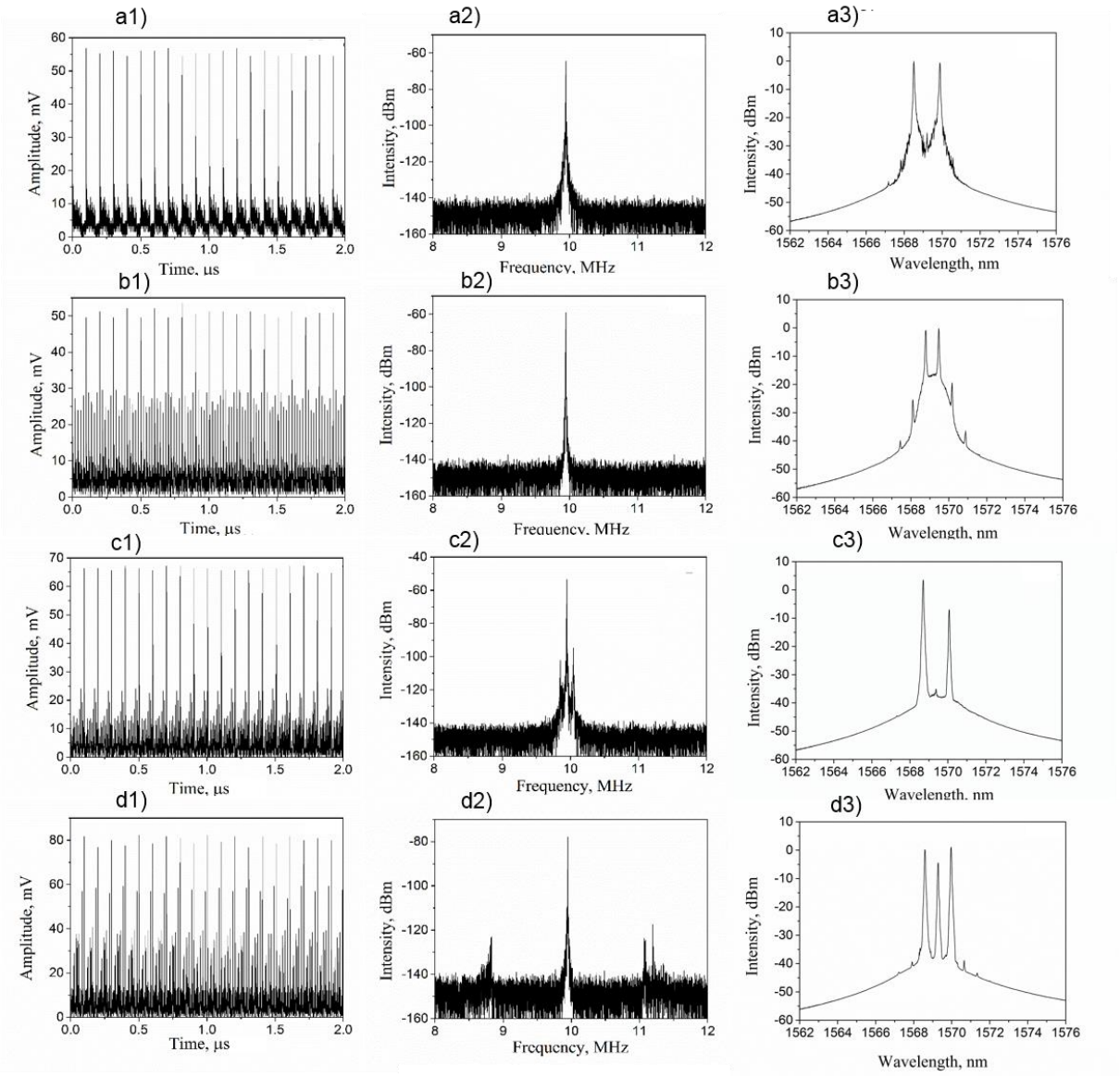

Fig. 2.6: The oscilloscope traces of the lasers regimes at different places of the intra-cavity polarization controller; (b) The RF spectra for partial and uncoupled laser regimes and (c) the corresponding optical spectrum: a1, a2, a3) PC1=-40^0; b1, b2, b3) PC1=45^0; c1, c2, c3) PC1=48^0; d1, d2, d3) PC1=50^0.

2.4: Multi-pulsing operation via Chiral Symmetry Breaking.

Chiral symmetry breaking (CSB), where mirror-symmetry is distorted under perturbation, is an underlying mechanism for many fundamental phenomena in different areas ranging from nuclear physics to nonlinear optics. Here in this section, we have demonstrated experimentally, using the same experiment described in section 2.2, that a fibre twist-based chiral symmetry breaking left and right polarization modes also leads to a versatile laser dynamics which is tuneable between the regimes of longitudinal mode synchronization,

harmonic, multi-pulse, and chaotic oscillations. This symmetry breaking is also a mechanism for the emergence of RW events.

The laser dynamics have been adjusted from the chaotic regimes due to incoherent coupling to mode locking at the fundamental frequency of 325.2 kHz by adjusting both PC1 and PC2 at the same pump power as in the previous section (18.4 mW). These results are shown in Fig. 2.7 (a) shows, multi-pulsing and chaotic oscillations and demonstrate the presence of optical RWs as some output amplitudes exceed the RW threshold (dotted line in Fig. 2.7 (a)). Here, the RW criteria which were discussed in chapter 1 were used to confirm that these are optical RWs. However, the periodical amplitudes that are related to the round trip period have excluded in view of predictable nature of the optical RW emergence. Out of phase and desynchronized excited modes led the laser system to emit multi-pulses in the bunch that propagates chaotically (Fig. 2.7 (a1) or multi-pulses with consistent separation (Fig. 2.7 (b1) in the laser cavity. This regime was observed when the positions of the PC1 and PC2 were 20^0 and 40^0 respectively from the vertical position. The single pulse similar to the mode-locked pulse in Fig. 2.7 (c1) formed as results of the matching between the beat lengths with the cavity length. This regime was observed when both PCs were adjusted to be -80^0. The harmonic oscillations shown in Fig. 2.7 (d1) are obtained as results of the resonance coherence coupling of the two polarization satellites with the central frequency line. The switching between the regimes is indeed driven by the CSB instability. The RF spectra for the different regimes are shown in Fig. 2.7 (a2-d2). For the sequence, a2–d4, the main peak becames wider and two new sets of peaks separated on ~380 Hz and ~95 Hz appeared for the regimes of chaotic bunches of pulses (Fig. 2.7 (a2). The satellites related to the power modulation instability also became wider and more visible. These satellites disappear in the coherent coupling when the two left and right polarization are coupled as shown in Fig. 2.7 (b2, c2). In the case of the harmonic oscillations shown in Fig. 2.7 (d2) demonstrates that the two satellites are in resonance coupling with the central frequency line. The signal to noise ratio (SNR) for most of the laser regimes is higher than 69 dB, which means the laser regimes are quite stable.

The corresponding optical spectra of these different laser regimes are illustrated in Fig. 2.7 (a3-d3). As follows from a3-d3, the optical spectrum of the multi-pulsing chaotic regime has two peaks (Fig. 2.7 (a3)) which means that the laser operates with incoherent coupling between the two polarization modes and emits chaotic pulses. The wavelength difference between the two central peaks is 0.5 nm which implies a beat length L_b is equal to about 19.6 cm; this gives the difference between the two orthogonal polarization refractive indices as 7.97×10^{-6}. We also observed that the right side of the optical spectrum of partial coupling that emits pulses with consistent separation (Fig. 2.7 (b3)) revealed a sideband structure or ripples meanwhile the left side remained smooth which apparently could be related to the soliton energy quantization. A clear single central peak at about 1566 nm and 1565 nm

were found for coherent coupling that emits a single periodic and harmonic pulses as shown in Fig. 2.7 (c3, d3) respectively.

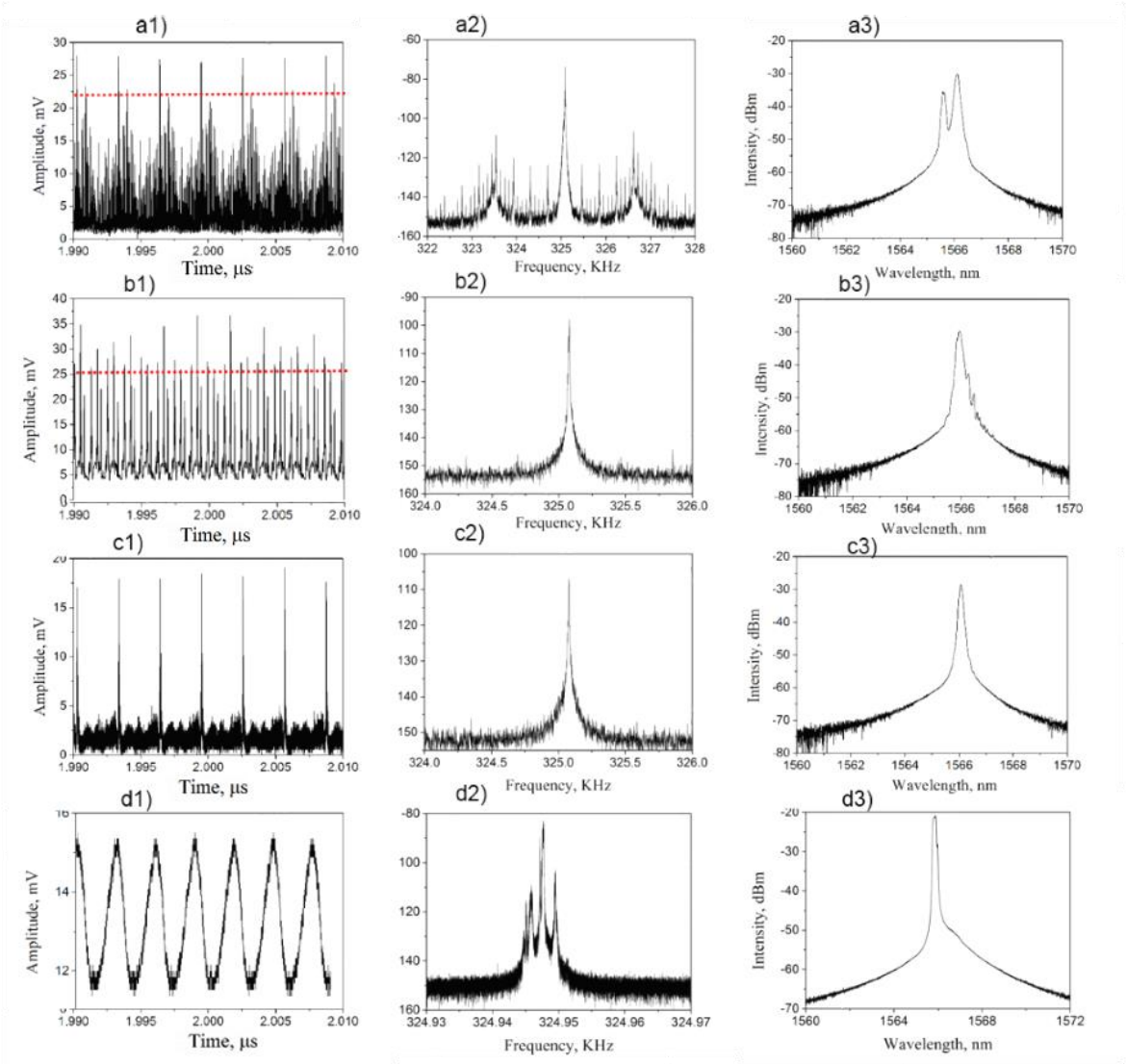

Fig. 2.7: Multi-pulsing laser dynamics observed by CSB; a1-d1) the output power in the oscilloscope measurement for different positions of the PC1 and PC2 (dotted line is the RWs threshold), a2-d2) RF spectrum and a3-d3 the corresponding optical spectra.

The polarization properties of these multi-pulsing regimes have also been studied using the polarimeter. Both PC1 and PC2 were adjusted to achieve polarization dynamics shown in Fig. 2.8.

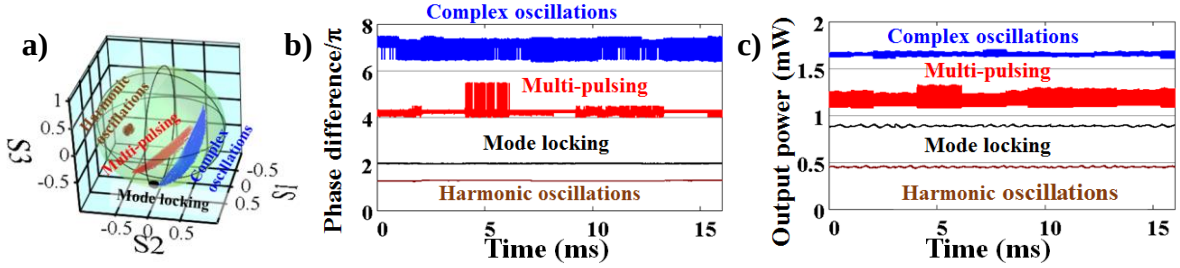

Fig. 2.8: Polarimeter results corresponding to the dynamics in Fig. 2-6: a) trajectories in Poincaré sphere; b) the phase differences $\Delta\varphi$ vs time; c) the output power vs time.

The Stokes parameters on the Poincaré sphere are shown in Fig. 2.8. For single and harmonic pulse regimes, the SOP is shown as a fixed point on the Poincaré sphere. This fixed point indicates a stable polarization with its axis defined by S_1, S_2, S_3 due to the coherent coupling. This means that by controlling PC1 and PC2, it is possible to adjust the anisotropy and in-cavity birefringence to enable strong SOP coupling leading to coupling of the longitudinal modes. The S_1, S_2, S_3 and DOP are changed when the laser is switched to a multi-pulsing regime and the polarization attractor forms an arc shape as can be clearly observed in the multi-pulsing regimes in Fig. 2.8 (a). The periodic variation of the Stokes parameters in this regime is due to fast switching between two polarization states. A chaotic attractor was observed in the chaotic pulses with random switching between orthogonal SOPs in Fig. 2.8 (b), which is connected to the emergence of RWs in Fig. 2.7 (a). This corresponds to the weak coupling between the SOPs resulting in random jumps in the phase difference (Fig. 2.8 (c)) and so to the emergence of spikes in the dynamics of the output power. It was also found that the location of the fixed point on the Poincaré sphere is altered by switching between the single periodic pulse and the harmonic oscillation regimes.

These experimental results are consistent with the theoretical model in reference [75] and similar results have been observed experimentally using low birefringence (spun fibre) instead of the HiBi in Fig. 2.5. Using spun fibre, different laser regimes can also be obtained and some examples showing stable regimes with periodic pulses similar to mode-locked to chaotic pulsing are found at a pump power of 72 mW as illustrated in Fig. 2.9. The power is 2 times higher than was used in the HiBi fibre laser. The switching between the lasers regimes, including single mode, multipulses and chaotic pulses (Fig. 2.9 (a1-d1) respectively) have also been done by changing the coherent coupling between the beat length and the cavity length via changing the PC1. The physical principle behind the generation of mode-locked pulses is mode synchronization due to the matching of beat length with the cavity length. This matching was achieved with PC1=-10^0 and PC2=5^0. In the slightly mismatched case, the laser emits an ordered multi-pulse with a consistent separation (Fig. 2.9 (b1, c1)). While the incoherent coupling when far from resonance leads to chaotic emission (Fig. 2.9 (d1)). These various regimes were formed when the SOP travelled down in the cavity from one point to another when we tuned the intra-cavity polarization and a different polarization mode coupling occur.

The RF spectra in Fig. 2.9 (a2-d2) show no sign of polarization satellites; this is because polarization is prevented by the spun fibre during the propagation and this leads the mode coupling. The SNR of all of these regimes is about 70 dBm which confirms highly stable

laser operation. The central peak of the spectrum is 9.9 MHz, which is matched to the laser cavity round trip and has a spectral linewidth of about 30 KHz. The optical spectra for each of these regimes are illustrated in Fig. 2.9 (a3-d3). The spectra show that the central wavelength peaks at about 1573.53 nm, whereas the distance between the peaks for the first and second is about 2nm (Fig. 2.9 (c1)). We calculate that the beat length L_b is equal to about 12.7 mm; this gives a difference between the two SOP refractive indices equal to 1.23×10^{-4}. The multi-peaks of Fig. 2.9 (b3, d3) confirm multi-pulsing per round trip in the output of the laser. In the case, the distance between the peaks narrows down to about 0.4 nm and confirms the higher birefringence and phase difference (L_b 2.544 mm; refractive indices difference is 6.17×10^{-4}) of the excited modes.

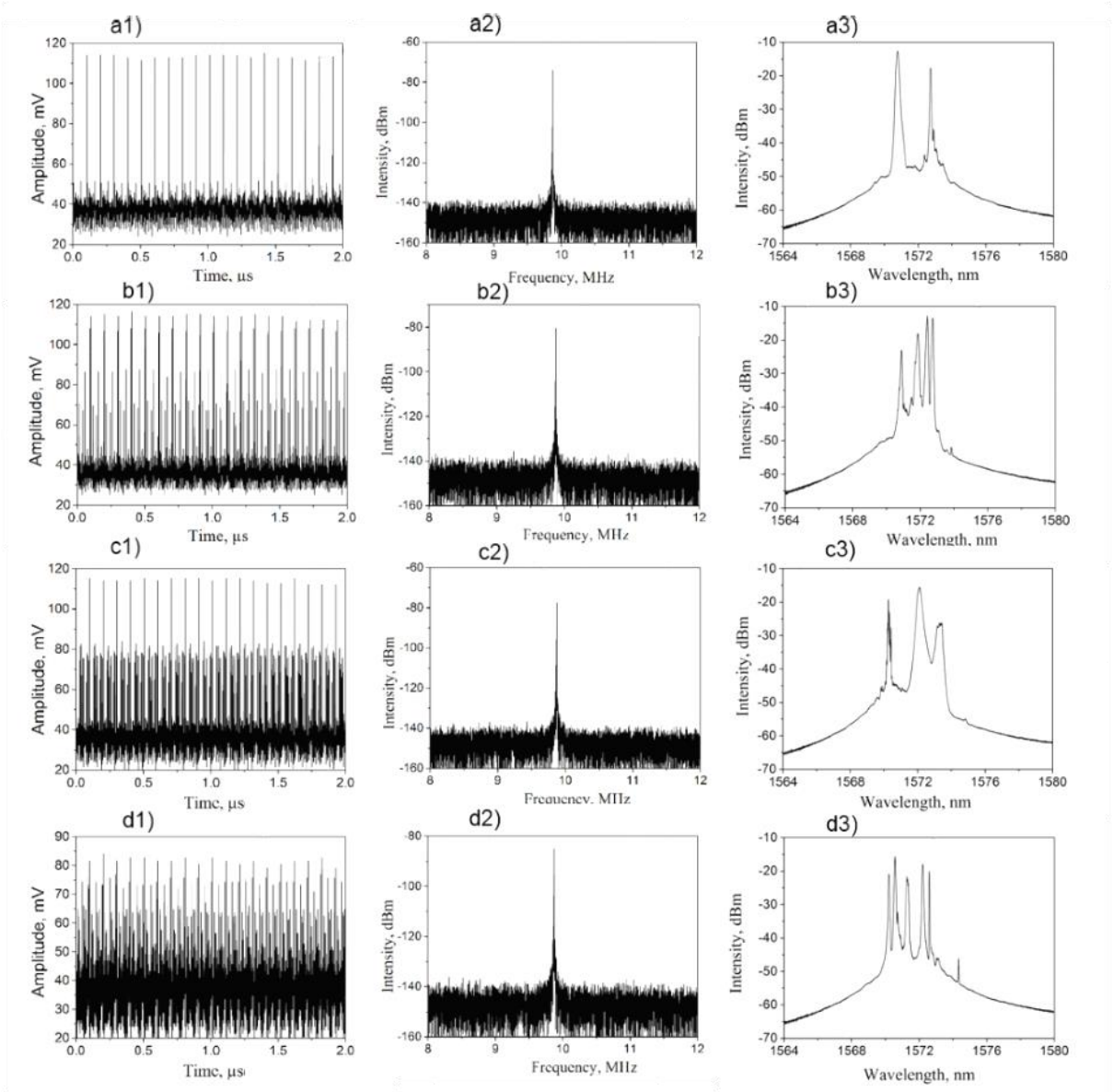

Fig. 2.9: The oscilloscope traces of the spun fibre lasers regimes at different places of the PC1; (b) The RF spectra of the observed laser regimes and (c) the corresponding optical spectrum a1, a2, a3) PC1=-10^0; b1, b2, b3) PC1=90^0; c1, c2, c3) PC1=95^0; d1, d2, d3) PC1=100^0.

2.5: Classification of Optical Rogue Wave Events

For optical RW studies that emerged due to both MMVI and CSB instabilities, the testbed fibre lasers that are described in section 2.2 provide an opportunity to obtain a huge amount of data under laboratory controlled conditions in a relatively short time. This helps to study the mechanisms of optical RW emergence. Several mechanisms were discussed previously for the emergence of fast optical RWs (FORW). These are based on soliton-soliton interactions and soliton-dispersive wave interactions [74] which are obtained in nonlinear optical systems when these operated under high pump power (600mW). Here, we have shown that the FORW also emerged in our long fibre laser which was described in section 2.2 at a very low pump power (18.4 mW) [76]. On the other hand, slow optical RWs (SORW) have previously been observed in a driven laser cavity via modulation of the pump source [40]. However, the SORW in our fibre laser, emerged without needing to modulate the pump power [77]. The classification of RWs as either FORW or SORW has previously been done by a theoretical estimation of the laser photon lifetime. This can be used in a fibre laser. Here, we show that the classification criterion between FORW and SORW is a comparison of the RW event lifetime with the main characteristic time of the system which is calculated from the decay of autocorrelation function (AF) of the experimental results [78]. In this experiment, SORWs have been observed over a long time scale as illustrated in Fig. 2.10 (a), where the events have a lifetime that can be in the scale of many seconds. Whereas, FORW in Fig. 2.10 (b) have been observed in the short time (sub-round trip time) where the event lifetime is in the ms or μs scale.

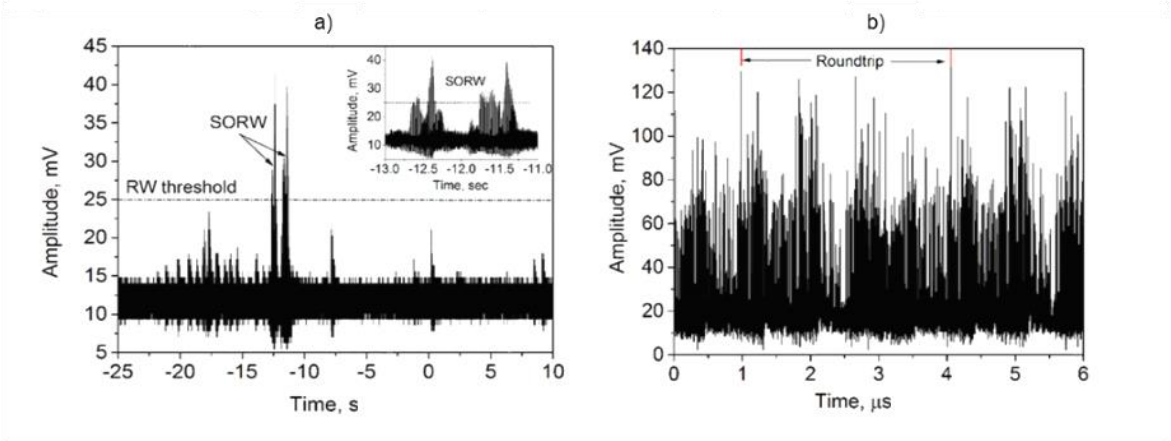

Fig. 2.10: (a) SORW event; (b) FORW event emerged in our proposed fibre laser.

The characteristic times of these observed optical RW events were calculated by using an oscilloscope trace with the length of 50 million points and a resolution of 0.1 ns. We found

that the AF of the SORW event decreased linearly over the measured range (Fig. 2.11 (a)) which allows the characteristic time to be calculated directly from the fitting line. The AF of the FORW pattern has decreased exponentially (Fig. 2.11 (b)); we replotted this data on a log scale to calculate the characteristic decay time of the AF (Fig.2.11 (c)). Indeed, the shapes of AF provide the information about characteristic times of the different processes which take place in the laser cavity. Therefore, the filtered AFs have different shapes in the different laser regimes. The small oscillations on the curves of the AFs in Fig. 2.11 correspond to the oscillations of the power with few 100 Hz or kHz frequencies shown in Fig. 2.7.

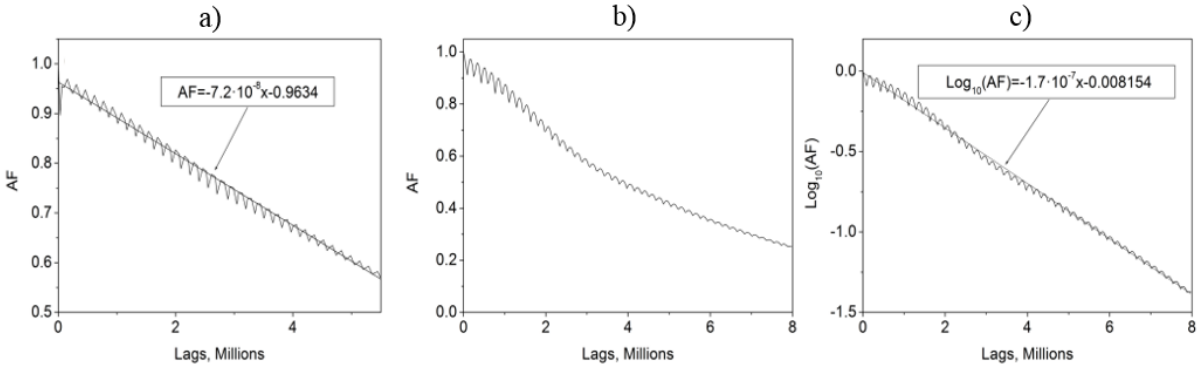

Fig. 2.11: Autocorrelation functions; (a) the AF of the SORW patterns, (b) AF of the observed FORW pattern in linear scale and (c) in Log scale with linear fitting. In all cases, the length on the one Lag was 0.1 ns.

We calculated the characteristic time τ_c of the AF from the fitting line (y=at+b) for both of the SORW and FORW; here (τ_c=1/a) in s. We used *x* instead of *t* in insets of Fig. 2.11 because of the scale of the horizontal axis is in *Lags* (0.1 ns per Lag). We found that the characteristic times were 1.39 ms and 0.59 ms for SORW and FORW respectively (the round trip time was 3.0773 μs). These times are quite similar to the Er^{+3} doped lasing photon lifetime; because of that, the observed events have been classified to the SORW and FORW. The AF also give information about the time the system can remember an initially induced perturbation. For instance, when the lifetime of the RW events is significantly longer than the first characteristic time (1.39 ms) as in the case for SORWs, the system loses information about how the pattern developed and thus the tail of the events is independent on the front of it (the system forgets how the pattern began while the pattern is still active). Meanwhile, in the case of FORW as the event lifetime is shorter than the characteristic time (0.59 ms), the system can remember the shape of the beginning of the RW pattern, and these patterns are affected by the periodic amplification in each round trip which can be considered as a kind of memory. Therefore, we have classified these optical RW events as either SORWs or FORWs depending on the ratio of the events lifetime to the AF decay

time. FORW events have a lifetime duration shorter than the AF decay time and SORW events have a longer lifetime than the AF decay time.

2.6: Slow Optical Rogue Wave Events

The SORWs have been studied by polarization mapping over a matrix of (19x19) positions of PC1 and PC2. We found that the mechanism responsible for the emergence of SORW patterns is polarization hopping as illustrated in Fig. 2.12. We can see that the system jumps from attractor (A0) to another (A1) as shown in Fig. 2.12(a, b) for two different positions of PC1. While the system switches between 3 different attractors in Fig. 2.12(c) which shows clear signs of optical RW events over a long time scale. Fig. 2.12(d) clearly has four amplitude attractors; therefore, hopping between the attractors (with appropriate excited frequencies) can lead to the generation of RW patterns in the second time scale. Actually, the same four attractors were observed in experimental records for water surface elevation in [79, 80] and were partially predicted theoretically [81, 82]. This situation apparently was also observed with external pump modulation [40]. The hopping between the attractors is probably occurring due to intrinsic low-frequency modulation (polarization instabilities) of a signal wave inside the cavity which is exactly coupled to an external pump modulation in [80]. This modulation is generated as a result of incoherent coupling between the two orthogonal polarization interactions inside the laser cavity.

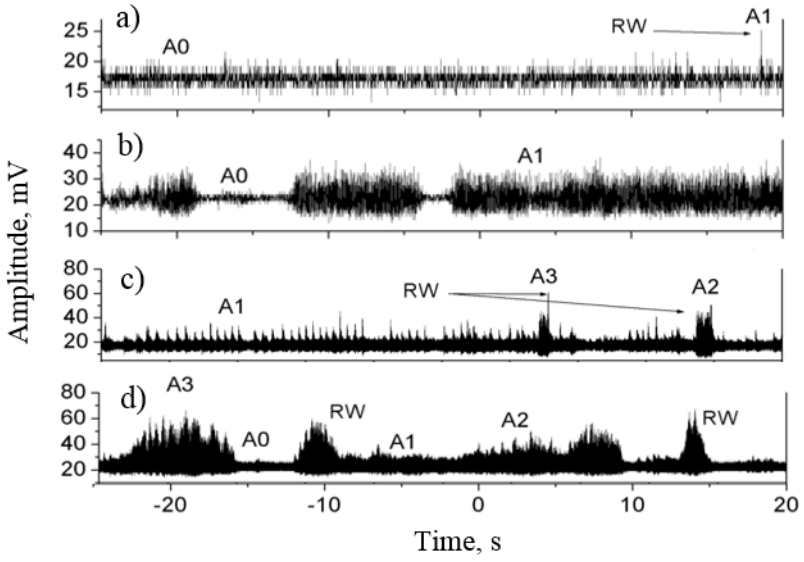

Fig. 2.12: The intermittencies of the SORW, showing the system apparently has four attractors labelled with A0-A3.

The PDF corresponding to the SORW pattern (illustrated in Fig. 2.13) was calculated from saved oscilloscope trace. The units of the horizontal scale were normalized to the output amplitude and expressed in units of standard deviation (σ). It can be seen from the PDF, that due to the optical RW events, the PDF has L-shaped and is significantly different from the PDF of a normal Gaussian distribution. From this result, the probability of SORWs was calculated to be ~0.195%. The PDF curve has a point of inflection when the abscissa is equal to ~4 units of σ. The normal output pulses in PDF were fitted with a Gaussian function, while optical RW event was fitted with a polynomial function.

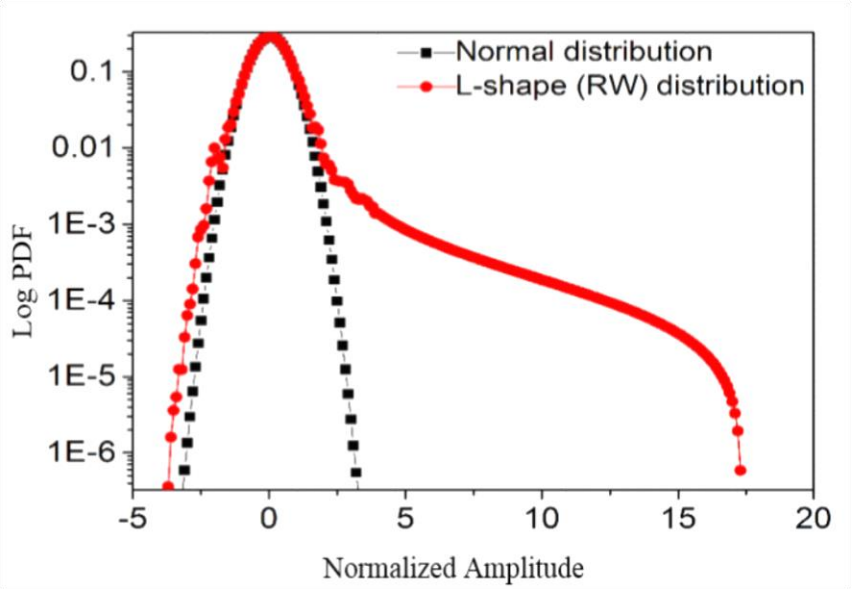

Fig. 2.13: PDF of the SORW events.

SORW events have been observed in many positions of the polarization controllers PC1 and PC2 as illustrated in Fig. 2.14. The blue points show where the SORW events were observed with a high probability (>10^{-4}); the black points show where SORW events were observed with a medium probability (10^{-7}< Probability <10^{-4}); the red points show the positions where the system has SWH or very low probability of SORW events (<10^{-4}); and finally, the empty positions show where the laser operated in the either multi-pulse, CW or FORW regimes.

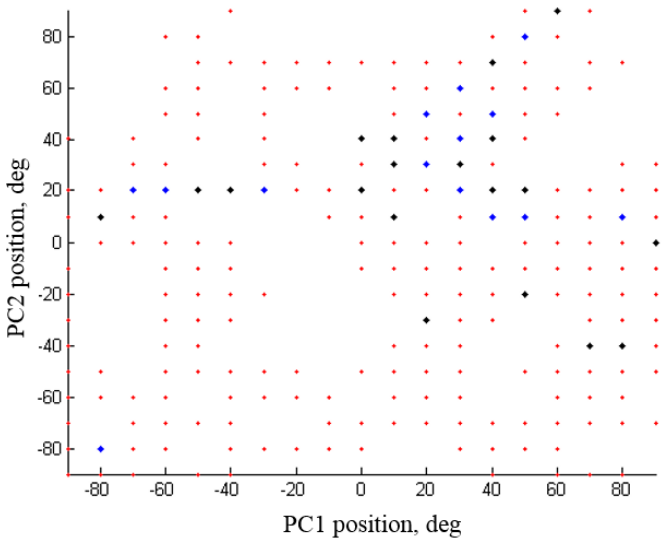

Fig. 2.14: The position of the observed SORW during all of the 19X19 PCs (red) low RW probability<10^{-7}; (black) middle RW probability 10^{-7}< Probability <10^{-4} and (blue) high RW probability>10^{-4}.

2.7: Fast Optical Rogue Wave Events

In the case of the FORW, the events have a lifetime shorter than the characteristic time of the AF (0.59 ms). FORWs were also studied by collecting experimental data of 19x19 polarization positions (polarization map) through tuning both intra-cavity and pump birefringence. We found that the FORW patterns were generated due to a pulse-pulse interaction in periodic amplification in each round trip, which can be considered as a kind of memory because the system remembers the frontier shape of the events. While, in the second scenario (SORW), the system forgets how a pattern began while the pattern is still active. This strongly affects the statistics of the optical RWs. However, in FORW, many events have been observed and then classified into two groups. The first group of patterns are the common patterns that are observed over most of the polarization space with a relatively high likelihood. These common patterns can be classified into three kinds of FORW (lonely, twins and three sisters). The second group of the patterns are rare patterns; inside of this group, two mechanisms of pulse-pulse interaction have been considered: the resonance interaction (the accelerated pattern) and the collision (the cross pattern). This group of the patterns have a relatively low likelihood. The switching between the regimes of interest can be adjusted simply by changing the birefringence in the cavity at pump power (18.4 mW) which is slightly higher than the laser threshold (16 mW). This allows the observation and classification of this wide range of FORW patterns in the same experiment.

2.7.1: The Common Optical Rogue Wave Patterns

2.7.1. A: The Lonely FORW Patterns

The lonely or solitary FORW patterns have been more commonly observed throughout the polarization space of this experiment than the other FORW patterns. This pattern has been observed in regimes similar to ordered multi-pulses and also at variable speed patterns. The oscilloscope trace of the lonely FORW patterns is shown in Fig. 2.10 (b). This pattern was observed with PC2 and PC1 at positions of -50^0 and 20^0 respectively. Also, it appeared for most of the positions of the PCs where FORWs have been observed.

To see the FORW mechanism formation inside the laser cavity, the saved oscilloscope trace results were analysed using the spatiotemporal evolution as shown in Fig. 2.15. The spatiotemporal evolution provide more details in the position of the round trip for 1600 round trips; the number of round trips was calculated from the length of the oscilloscope trace (5 ms) and the round trip time (3.077 µs). The oscilloscope resolution was 100 ps/pt. With these parameters, we have a 50M points from each oscilloscope trace that were processed to detect the FORW patterns. Fig. 2.15 shows the pattern itself in (a), the result of filtering FORW detection in (b), as well as a 3D view of the front (c) and the back (d) of the pattern. The pattern illustrated in Fig. 2.15 corresponds to a cavity polarization birefringence of $1-7.71\text{x}10^{-6}$, this means that the events are propagating at about 1544 m/s faster than the average speed of light. The pattern oscillated during ~200 round trips or ~600 µs (the red-coloured in Fig. 2.15 (a)); after that, the FORW events lost energy to an event with less amplitude (beyond SWH; the yellow-coloured top in front and back views) over 152 µs. After that, the yellow-coloured pulse became unstable over 80 round trips (~240 µs) and finally, after a short period of uncertainty, it split into two different pulses as shown in the encircled area in Fig. 4.15 (a). Both the follower and the precursor were affected during the uncertainty splitting time as labelled 1 and 2 in Fig. 2.15 (a). The precursor showed a similar behaviour, however, the follower just has vanished without oscillating. Fig. 2.15 (b) shows the digital filter of regime indicating the RW event. The ratio between the overall energy and the pulse speed after the interaction also remained approximately unchanged as shown in front and back view of 3D spatiotemporal evolution shown in Fig. 2.15 (c, d). That shows the splitting of this pattern was an elastic process. The estimated likelihood of the pattern as the ratio between the number of observations of this pattern and the number of observations of the FORW patterns is a high value of 0.6.

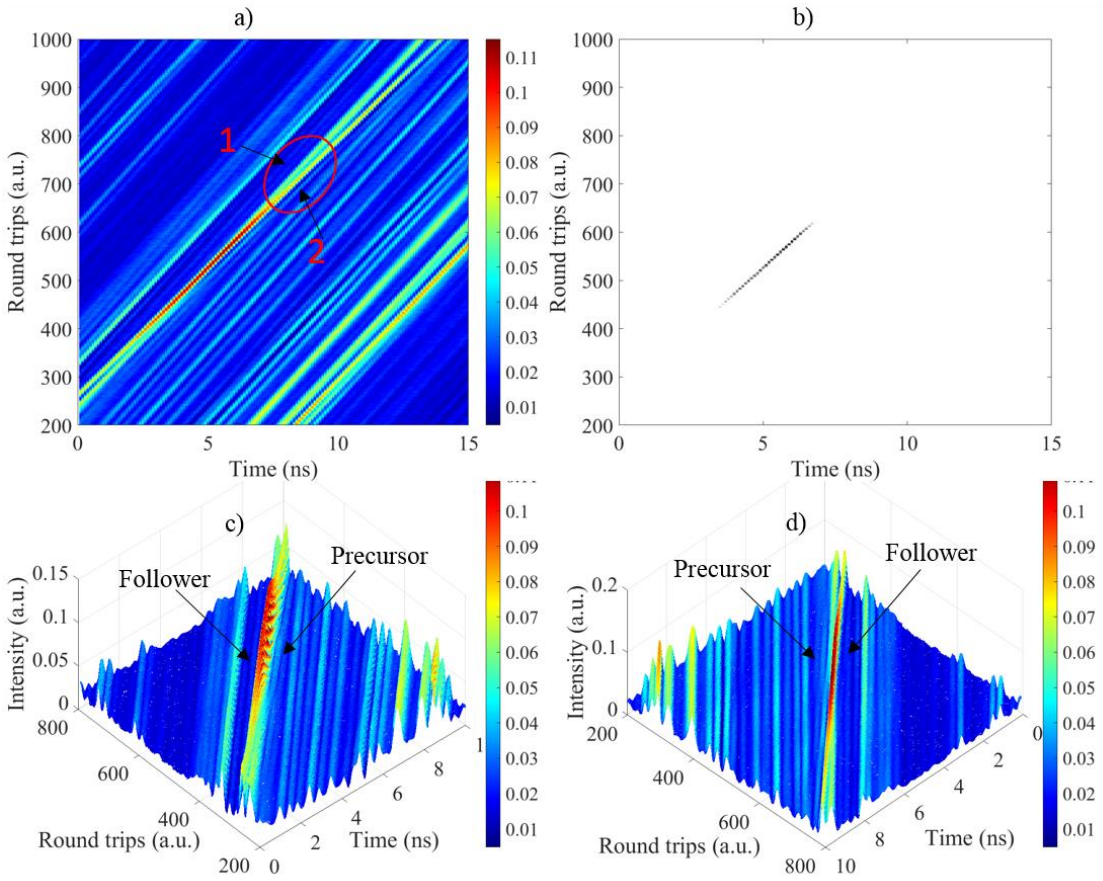

Fig. 2.15: A lonely FORW; (a) 2D spatiotemporal evolution, (b) the pattern after digital filtering; (c) front view of the pattern; (d) back view of the pattern.

2.7.1. B: The Twins FORW Pattern.

The pattern of two ORWs propagating in parallel as twins has been observed in a few positions of the polarization mapping and has a significantly smaller likelihood than the lonely pattern in the previous section. The spatiotemporal pattern of this event is shown in Fig. 2.16 (a), (b) shows the result of digital filtering to indicate the RW events, and 3D views of the front and the back of the pattern are presented in c and d respectively. This pattern was observed when the PC2 and PC1 were set to -70^0 and 40^0 respectively. This behaviour is similar to the two-pulse soliton molecule in reference [83], although the pattern in the illustrated case has a significantly longer lifetime. This pattern shows oscillations in a breather like style with a period of ~0.615 ms (~1.5 kHz). This frequency of oscillation matches the frequency of satellites observed in the RF spectra in Fig. 2.2. At the same time, the pattern of pulses was propagating ~2000 m/s faster than the average speed of light and the polarization birefringent refractive index difference for the pattern was calculated to be $1\text{-}9.6\cdot10^{-6}$.

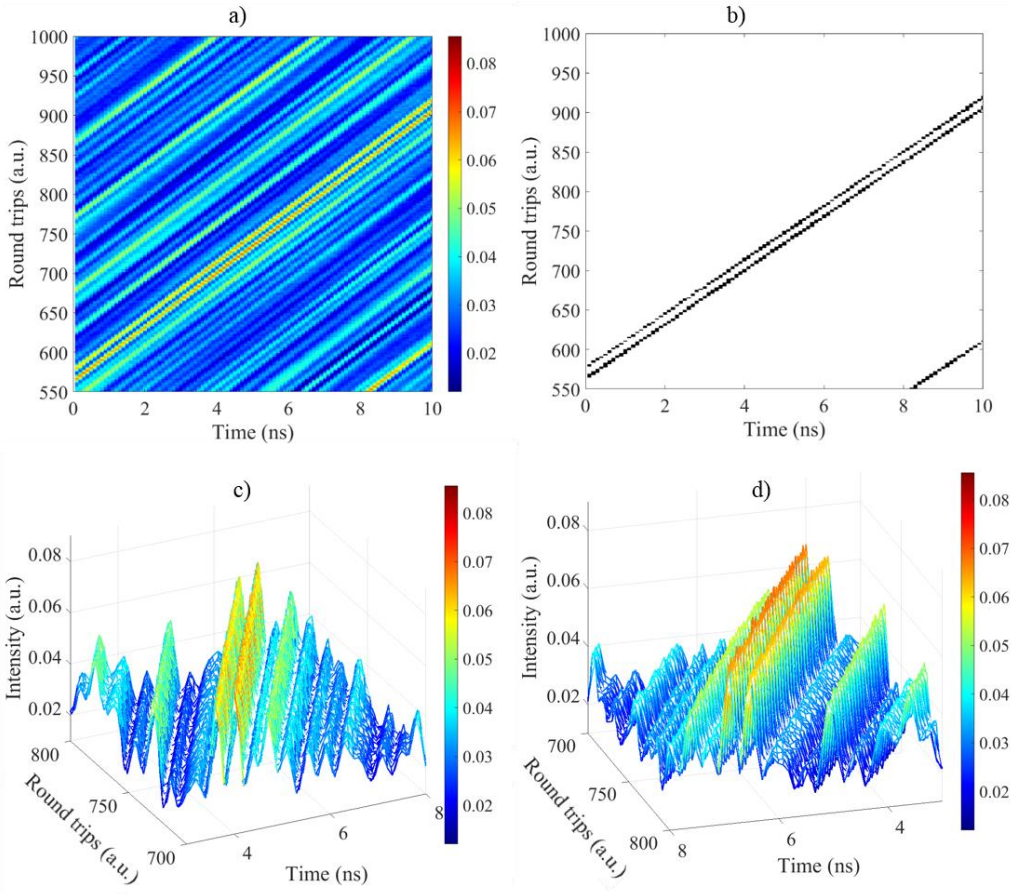

Fig. 2.16: A twins FORW pattern; (a) 2D spatiotemporal evolution, (b) the pattern after digital filtering; (c) front view of the pattern; (d) back view of the pattern.

It can be seen from this figure that the twin FORW events have a typically long lifetime which is approximately 333 round trips (~1 ms). After that, the continuous pattern vanished and the laser surpassed the RW threshold only in oscillation maxima forming kind of a chained or coupled lonely pattern. At the same time, the first pulse of the pattern became split in two. The remains of it interacted with the precursor and the follower forming two practically equal SWH pulses separated with a small pulse in the middle between them. This mechanism of the destruction of a long-living RW pattern when the pulse loses part of its energy after being split in two was observed frequently, being one of the most common ways of the destruction of twin patterns. It was also observed that this kind of pattern appeared either close to the main pulse or close to a high sub-harmonic pulse (in the case of a multi-pulsing regime). The extremely long lifetime of the twin patterns can probably be explained by a periodic amplification of the pattern in each round trip; that is to say, the pattern cannot appear between pulses because the energy of the system is depleted and is not enough to amplify the pulse above the RW threshold. The likelihood of this pattern was ~0.3.

2.7.1. C: Three Sisters FORW Patterns.

The pattern illustrated in Fig. 2.17 shows three FORW propagating in a bunch. The direction of the observer moved in the direction of the time axis which can be observed three consecutive RW events. This was observed when the laser operated in chaotic multi-pulsing per round trip which is not related to the main mode-locked pulse or a periodic sub-pulse. Unlike the twin pattern, this pattern shows a structure quite similar to Akhmediev's breather structure [27].

It can be seen in Fig. 2.17 (a), that the third optical RW event formed from the attraction (A) of two SWH pulses as in the lonely RW; at this time, the amplitude of the precursor of the third RW has increased above the RW threshold. After that, the optical RW split again into two repulsion (R) pulses of SWH. Such attraction and repulsion between pulses have been observed previously [84, 85]. The lifetime of this pattern was about 75 round trips (~225 µs). After the third RW event was split into two SWH pulses, this pattern disappears and did not emerge again. The speed of propagation of the pattern was ~1600 m/s slower than the average speed of light. The period of oscillations of the pattern was similar to the period observed in the case of the twin pattern. The likelihood of this pattern was low (~0.1). Furthermore, it appeared for only a few positions of the polarization controllers.

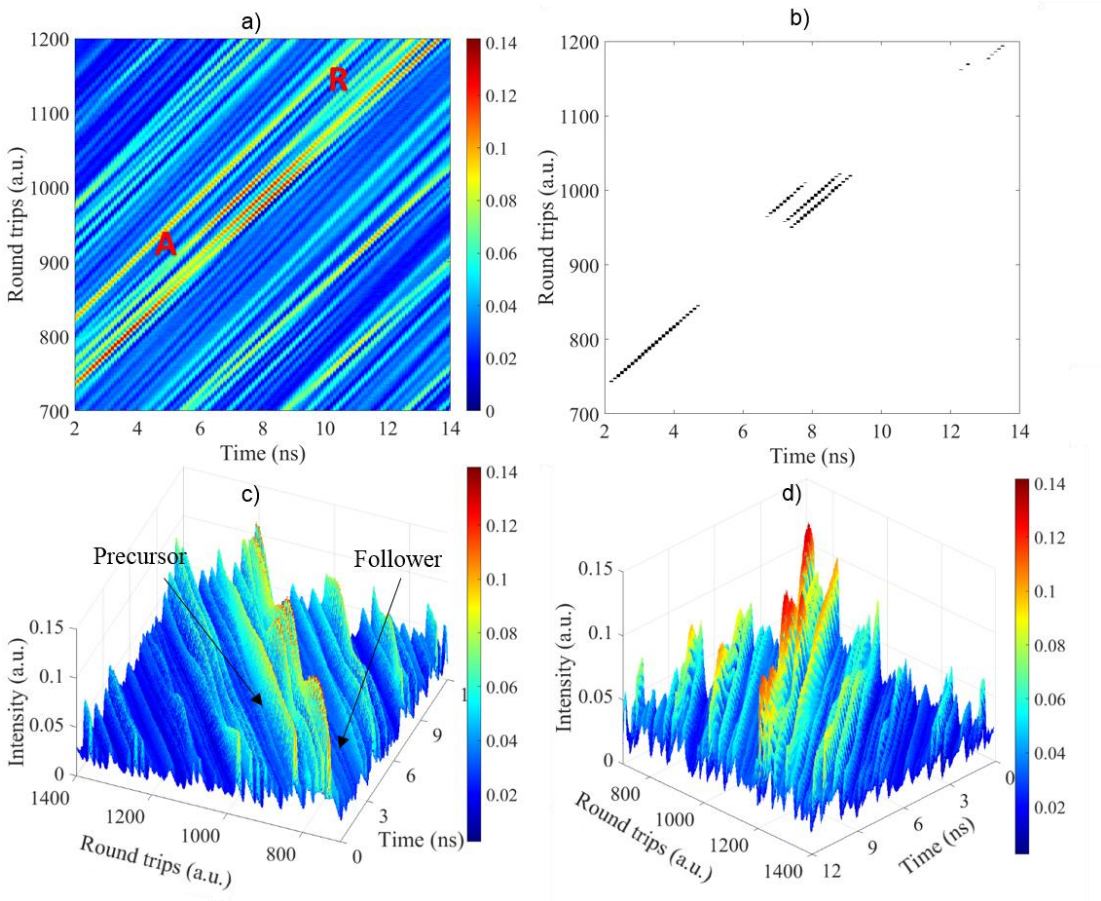

Fig. 2.17: Three sisters FORW pattern. (a) 2D spatiotemporal evolution, (b) the pattern after digital filtering; (c) front view of the pattern; (d) back view of the pattern. The white circle labelled with "A" indicates the attraction of the pulse before merging, meanwhile, the red circles labelled with "R" show the process of the repulsion of pulses.

2.7.2: The Rare optical Rogue Wave Patterns

2.7.2. A: The cross Rogue Wave pattern

When the laser operated in a multi-pulsing per cavity round trip regime, it was found that some pulses could propagate at different velocities leading to pulse-pulse collision and the formation of FORW events as illustrated in Fig. 2.18. At first view, this pattern seems to be similar to the patterns that had been theoretically illustrated by Antikainen in [86] for solitons with a duration of ~30 fs or as also illustrated in second order RW [13]. However, unlike in both of these cases, the observed pattern has a pulse duration of ~400 ps and integration of the oscilloscope traces have revealed that the intensity of the peak is just a sum of the intensities of the collided pulses.

Also, it seems that this pattern is formed only due to the collision of two pulses without any interference between them. There was no sign of energy exchange due to the very high difference in the pulse speeds (~100 m/s). This high speed difference allowed the pulses to collide with each other and form FORWs with an event lifetime of about 10 round trips with a lifetime duration of 30 μs. Therefore, the cross pattern can be considered as the limit case of the same pulse-pulse interaction mechanism. This pattern was observed over a very narrow range of the PCs positions. The likelihood of this pattern was extremely low (<0.01).

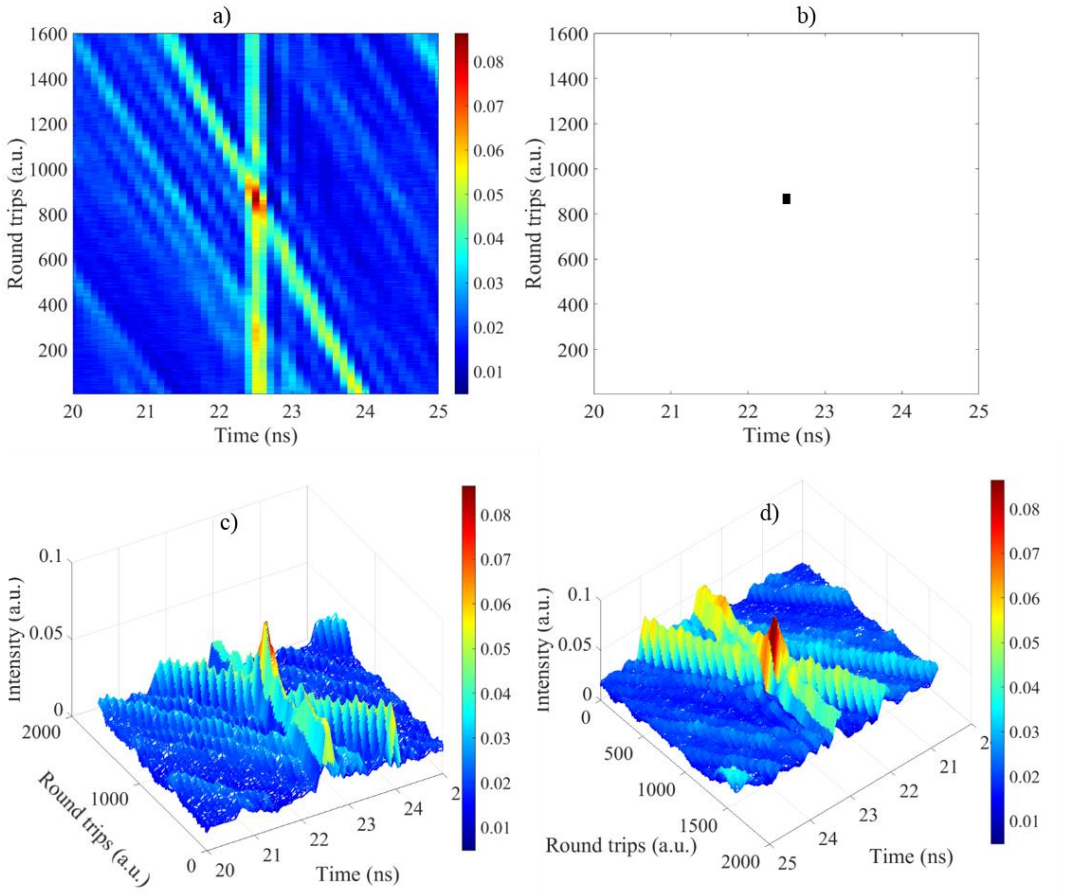

Fig. 2.18: A cross FORW pattern; (a) 2D spatiotemporal evolution, (b) the pattern after digital filtering; (c) front view of the pattern; (d) back view of the pattern.

2.7.2. B: The accelerated Optical Rogue Wave pattern

By analysing our experimental results over the spatiotemporal domain, collision patterns could be observed corresponding to the situation where two pulses collide with each other leading to FORW formation. It was observed that the speed of FORW events can accelerate over time as illustrated in Fig. 2.19. The pulse acceleration has been discussed in [42, 87] where the effect was due to soliton-soliton interactions with a duration of a tenth of a femtosecond and a peak power of a tenth of a kW. Whereas, in our fibre laser, the pulse has a very low pump power (18.4 mW) and a long pulse duration of 40 ns. That means the acceleration of the pulse was probably observed as the result of intrinsic nonlinearities in both the active and the passive fibre. At the beginning of the observation, the RW has propagated far from the oncoming pulse showing oscillations in a breather like style (Fig. 2.19 (c, d)), but when the pulse labelled 2 has interacted with the precursor labelled 1 (relative speed between pulses ~10 m/s) the RW pattern stopped oscillating; after a short transition process, it has acquired an acceleration of ~20 km/s^2, which was lost gradually over approximately 600 round trips (~1.8 ms). Through this process, the speed of the pulse (relative to the average light speed) has increased from ~-74 m/s to ~-54 m/s; the precursor

labelled with 3 has lost energy and the approaching pulse labelled with 4 has gained this energy. The whole pattern has propagated ~10 m/s faster than the average speed of the rest of the pulses.

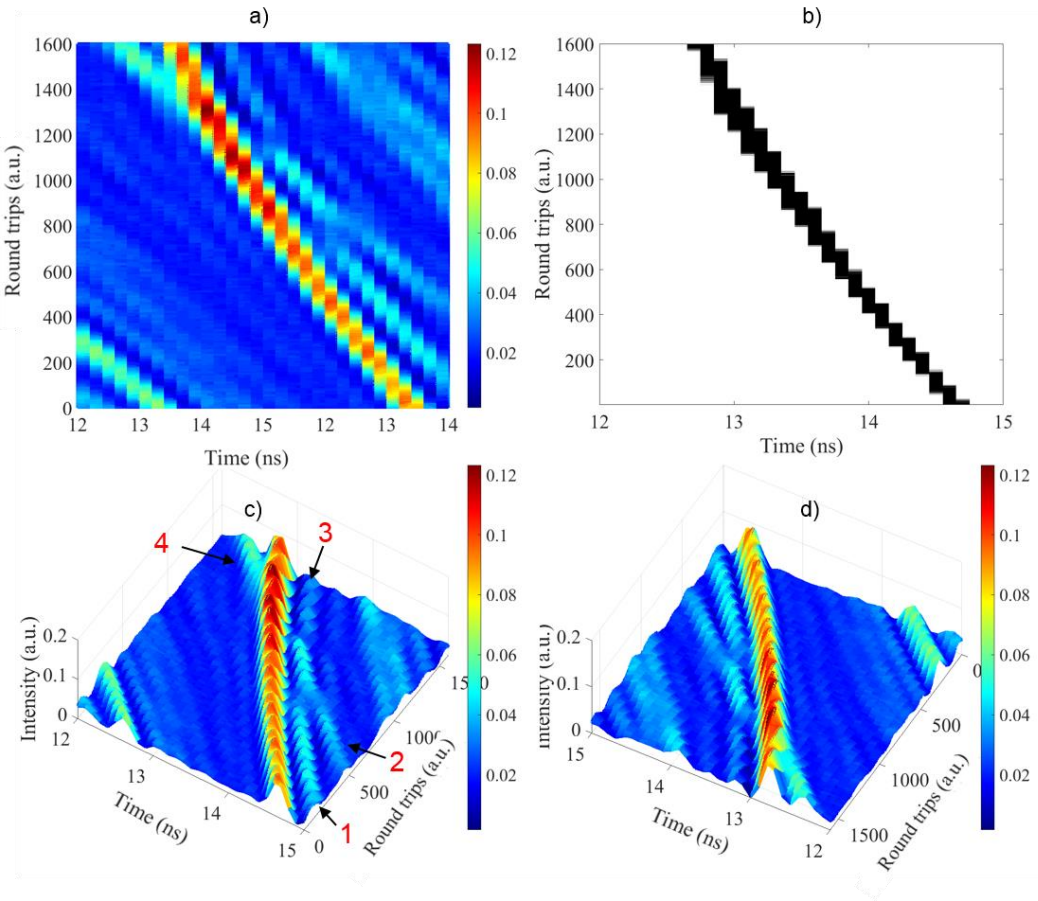

Fig. 2.19: A solitary FORW propagating with acceleration. (a) 2D spatiotemporal evolution, (b) the pattern after digital filtering; (c) front view of the pattern; (d) back view of the pattern. The black arrows show the direction of the pulse propagation.

The most notable characteristic of the RW process events is the highly skewed PDF associated with it. The PDF of the FORW shown in Fig. 2.20 was calculated from the 50M point long record oscilloscope trace. We observed that the FORW patterns have a strongly asymmetric shape and large deviation from a Gaussian distribution with a long tail more than 8 σ from the mean value on the right side of the PDF.

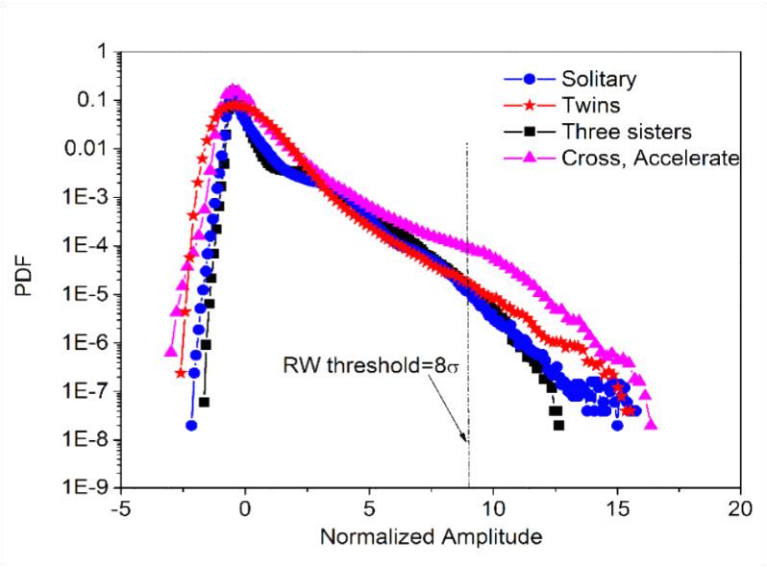

Fig. 2.20: PDF of the all of the FORW patterns.

2.7.2.3: Other Different Optical Rogue Wave patterns.

We have also observed high order FORWs pattern that emerged as the result of many pulses interacting as illustrated in Fig. 2-20. Fig. 2-21 (a), shows 3 pulses which emerged due to interacting with each other and formed FORWs with an amplitude higher than the 8 σ of the normalized amplitude. After a certain time (RW lifetime ~100RT), the RW event starts to lose the energy to SWH which became unstable for about 80RT (246.1 μs) and then separated back to 3 pulses which propagated with the normal amplitude. This classifies this process as an elastic interaction. Fig. 2.21 (b) shows the 3D front view of the pattern. The same scenario has been found for the FORW patterns that emerge when 4 or 5 pulses interact to form FORW and then separate back into the original 4 or 5 pulses.

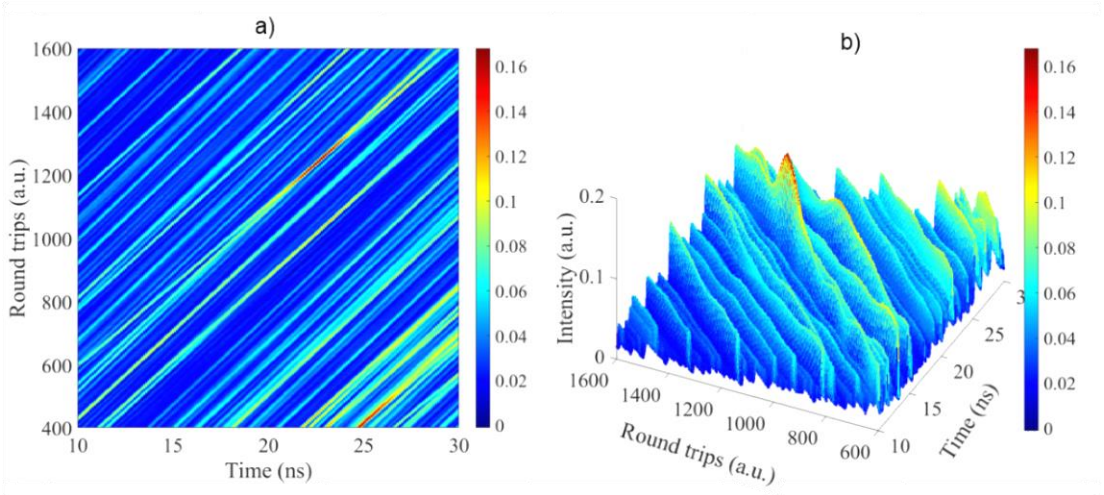

Fig. 2.21: FORW pattern emerged as results of 3 pulses interaction. (a) 2D spatiotemporal evolutions, (b) 3D front view of the pattern.

It was also found that there are some pulses that can lose all of their energy and vanish during the RW formation time. For instance, the FORW in Fig. 2.22(a) shows that the pattern emerged from the interaction of 3 pulses, but it separated back into only 2 pulses confirming inelastic interaction. The same scenario has also been found for the FORW patterns that emerge as the result of the interaction of 2 pulses which formed an optical RW and then lose energy gradually to propagate with the normal amplitude as one pulse.

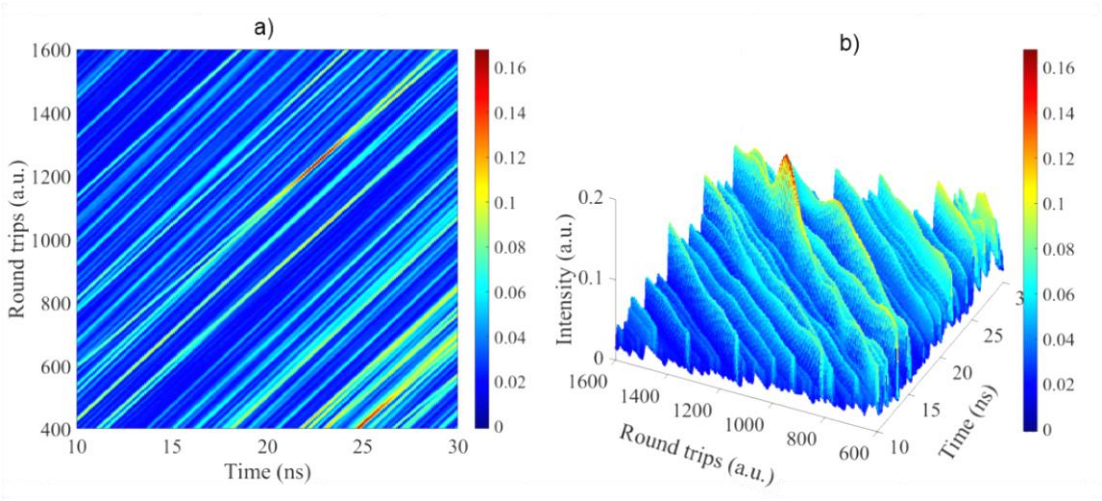

Fig. 2.22: FORW pattern emerged as results of interaction of 3 pulses and then separated into 2 pulses (a) 2D spatiotemporal evolution, (b) 3D front view of the pattern.

2.8: Conclusion

In conclusion, we have experimentally demonstrated a new type of low threshold vector resonance multimode instability which inherits features of multimode and modulation instabilities in a unidirectional long cavity fibre laser system. This instability has driven the laser system to tune from a chaotic regime to the single pulse similar to the mode-locked laser regime. The RF spectra show two types of satellites in addition to the fundamental laser frequency line: the first one of which is close to the round trip frequency and is related to the power modulation instability; and the second one is related to polarization rotation in the laser cavity. Another instability mechanism that is related to chiral symmetry breaking has been demonstrated using the same fibre laser. Using this mechanism, the output can be tuned from chaotic to single pulse regimes. Based on both of the instabilities, we have presented the first experimental classification of optical RWs temporal utilizing the autocorrelation function. Thus, in comparison with the AF characteristic time, FORW events have a lifetime duration shorter than the AF decay time and emerge due to the result of pulse-pulse interactions and nonlinear pulses dynamics. While SORW events have a lifetime duration significantly longer than the decay time of the AF and are the result of polarization hopping between different attractors due to incoherent coupling from the

polarization instability. This could occur in both active and passive fibre through polarization hole burning by means of polarization attractors. Therefore, our results can be explained in terms of hopping between different attractors in a multi-state oscillation system.

Meanwhile, the dynamics of the interaction between pulses leads to the conclusion that all of the observed FORWs have been placed in an active fibre due to nonlinearity induced by the inverse population as well as the intrinsic nonlinearity in the passive part of the cavity. Most of the mechanisms of the pulse-pulse interaction were found to be mutually exclusive. This means that all the observed RW patterns namely, the lonely, twins, three sisters and cross are probably different cases of the same process. The particular pattern observed depends on the speed between the pulses. The PDF of the output amplitude is highly dependent on the cavity birefringence, and satisfies the criteria for RW identification for both the FORW and SORW events.

Finally, we can summarise the observed optical RW patterns in our unidirectional long laser cavity in the flow and Pie-charts which are illustrated in charts 2.1 and 2.2 respectively. Also, we summarise the lifetime, likelihood and the formation mechanisms of the optical RW patterns in table 2.1.

Chart 2.1: Flow-chart of all RW events observed in our experiment unidirectional long laser cavity.

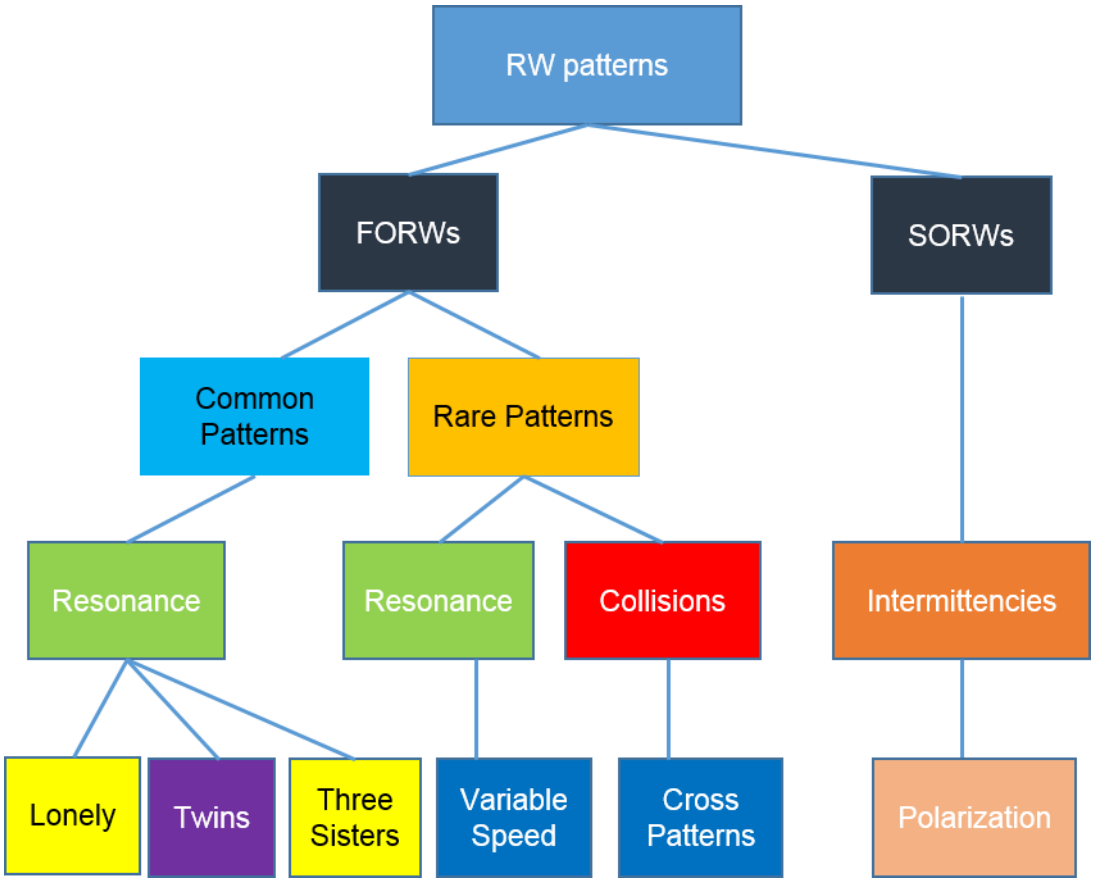

Chart 2.2: Pie-chart of all RW events observed in our experiment unidirectional long laser cavity.

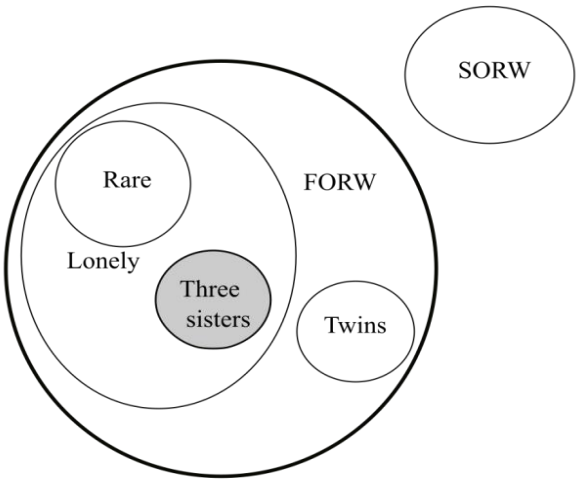

Table 2.1: The observed RW patterns lifetime its likelihood and mechanism.

Pattern	Lifetime (round trips)	Likelihood	Mechanism
Lonely	Hundreds	~0.6	Pulse-pulse interaction
Twins	Thousands	~0.3	Pulse-pulse interaction
Three sisters	Hundreds	~0.1	Pulse-pulse interaction
Accelerated	Hundreds	<0.01	Pulse-pulse interaction
Cross	$<10^{-4}$	<0.01	Pulse-pulse collision
PSORW	Hundreds of thousands	0.195	Polarization trapping

Chapter 3

Optical Rogue Waves Based on Soliton Rain and Soliton Fission

3.1: Introduction

The mode-locked fibre laser as a source of ultra-stable pulse trains has been of fundamental technological importance in the revolution of a wide range of natural and applied research areas [27, 88-90]. These include material processing, optical communications, natural science, optical frequency metrology, sensing and medicine [27, 88, 91-94]. Moreover, these ultrashort pulse lasers have attracted significant interest in the field of nonlinear dynamics studies [27, 89]. This is because of the complex interplay of linear and nonlinear effects, as well as gain and loss mechanisms, which can give rise to a rich diversity of nonlinear dynamical forms that can be systematically explored by controlling individual laser parameters such as pump power, polarization, and cavity dispersion. Adjusting parameters such as these can enable high flexibility in the generation and the ways to control the nonlinear dynamic states. These states include the high harmonic mode-locked regime soliton rain and soliton fission which are the most intriguing phenomena in mode-locked lasers. This chapter presents for the first time, soliton rain and soliton fission as a mechanism for originating optical RWs at low pump power. High harmonic mode-locked (HML) states are also presented in the beginning of this chapter.

Typically, most of the fibre lasers operate at a repetition rate of tens of MHz due to the relatively long laser cavity. However, applications such as telecommunication, spectroscopy and metrology require higher repetition rates. The HML is a practical path to increase the repetition rate by a factor of 100 through the selective excitation of the harmonic of the fundamental frequency. The HML is based on the multi-pulsing which emerges because of

the interplay between the laser cavities' bandwidth constraints and the energy quantization associated with the resulting mode-locked pulses [95]. The increase in the mode-locked spectral bandwidth with growing pump power is limited by the gain bandwidth of the cavity. To overcome this constraint, a single pulse is split into many pulses with the energy shared between the pulses and bandwidth remaining within the gain bandwidth window. This splitting is accompanied with the electrostriction effect in the form of excitation of radial R_{0m} and torsional-radial TR_{2m} acoustic modes. Interaction of such acoustic modes with the multi-pulse regime can result in a 1.2 GHz repetition rate for passive HML based on nonlinear polarization rotation (NPR) [96, 97]. The HML with 2.2 GHz repetition rate has also been realized using a tilted fibre Bragg grating in NPR [98]. A 10 GHz harmonic repetition rate has been achieved using a nonlinear amplifying mirror (NALM) [99]. However, both NPR and NALM techniques are intrinsically environmentally unstable as both techniques use an artificial saturable absorber (SA). Furthermore, the development of novel materials as SAs have been evolved from semiconductor towards nanomaterials for a stable high laser repetition rates [100-102]. Therefore, researchers have spent considerable efforts investigating HML using SAs, such as semiconductor saturable absorbers (SESAM) [103], carbon nanotubes (CNT) [104-106], graphene [107] and other nano-materials [108-110]. Although SESAMs provide a stable 2.6 GHz HML, it also possesses some inherent drawbacks, for instance, having a narrow bandwidth and requiring a complex multi-layer fabrication. Therefore, nanomaterials such as CNT and graphene have been found to be good candidates for fabricating excellent SAs. Single-layer graphene has an intrinsic ultra-broadband SA, but it often has a low modulation depth. The CNT [111, 112] possesses some advantages such as wavelength-independent SA characteristics, a low saturable absorbing threshold, and a large modulation depth due to their high optical nonlinearity, high damage threshold, low insertion losses, wide spectral range and fast recovery time SA. Furthermore, SAs using single-wall CNT (SWCNT) are insensitive to environmental instability. Therefore, much attention has been paid to CNT SA-fibre lasers in recent years. Recently, various techniques and configurations have been investigated for SWCNT mode-locking in EDFL. Also, SWCNT SAs have been embedded in various kinds of polymer matrix for different mode-locking studies including high power [113], tuneable wavelength and pulse duration [114] and switchable wavelength [115, 116]. Using this technique, a 23rd (328MHz) harmonic of the fundamental cavity frequency was experimentally observed [116]. Also, a stable 10^{th} harmonic of 245 MHz repetition rate was achieved [106]. Nevertheless, a challenging task still exists in the context of understanding the role of the polarization independent radial R_{0m} and polarization-dependent torsional-radial TR_{2m} acoustic modes in the stabilization of HML. Therefore, high HML near to 1GHz is discussed at the beginning of this chapter as we have observed for the first time in a SWCNT passive mode-locked fibre laser.

Another intriguing nonlinear dynamic phenomenon in mode-locked lasers is the soliton rain. Soliton rain is a process whereby existence a complex self-organized intermediate regime with of the order of tens of small soliton pulses aggregated in a condensed soliton phase constitutes with CW in the form of spontaneously noisy background as a necessary condition for their appearance [9]. When the fluctuations in the CW exceed a certain level, these small solitons are formed, as a droplet would be formed from a vapour cloud. It then drifts towards a soliton cluster with a high probability to interact with other pulses or overlapping through their tails. This complex dynamic has been addressed as the main source for optical RW formation. Therefore, the investigation of this natural nonlinear dynamic is of interest for both fundamental and applied studies. The soliton rain phenomenon was first identified experimentally in laser physics using dissipative soliton generation by NPR [10]. Then it was observed in some other laser experiments such as in ultra-long fibre lasers [11] and NALM or figure of eight [12, 13]. But with all these lasers, a high pump power (>430 mW) was required before soliton rain regimes were observed. In addition, both NPR and the NALM, are environmentally unstable. Therefore, due to the drawback of the high pump power as well as the multiple interaction processes involved with such lasers, the modeling of soliton rain dynamics represents a challenging task. This modelling remains to be undertaken even with the previous research, where comprehensive experiments have demonstrated a clear way towards building a model which can reproduce soliton rain. Therefore, it is important to develop a more stable mode-locked laser that is able to observe soliton rain with low pump power.

The objective of this chapter is to provide an experimental platform for a nonlinear localized dynamic framework for observing soliton rain, soliton fission and soliton interaction based on a testbed SWCNT-SA passive mode-locked laser at low threshold pump power.

This chapter is organized as follows: In section 3.2, the experimental setup of the testbed passive mode-locked fibre laser and its characterization are described. High harmonic mode-locked operation at up to 902MHz driven by R_{0m} and T_{0m} acoustic resonances are found and are explained in section 3.3. In section 3.4, the soliton rain regimes are demonstrated in the range of low pump powers. The appearance, flow and the numbers of small pulses can be controlled by intra-cavity birefringence and the laser pump power and this is presented in this section. High harmonic soliton rain is presented in section 3.5. Soliton fission and the effect of temporal spacing and frequency separation at different laser parameters on the optical RW emergence are studied in section 3.6. The soliton rain interactions that lead to the emergence of optical RWs are demonstrated in section 3.7. Finally, the ranges of soliton parameters for achieving nonlinear localized dynamics are concluded in section 3.8.

3.2: Experiential Setup and Characterization

The schematic of the testbed SWCNT-SA passive mode-locked fibre laser is illustrated in Fig. 3.1(a). The laser cavity contained a 0.75 m long erbium-doped fibre (EDF) which is used as an active medium and has an absorption of 80 dB/m and a second order dispersion (β_2) of +59 ps^2/km at 1550 nm. The rest of the cavity is a 10.55 m SMF with β_2 of −22 ps^2/ km; the overall cavity length is 11.3 m. Therefore, the net cavity dispersion supplied soliton pulses. A fibre-pigtailed 980 nm laser diode was used to pump the EDF through a 980/1550 WDM. Polarization insensitive isolator with 51dB attenuation was used to ensure unidirectional operation of the ring cavity. The intra-cavity birefringence was controlled by PC1, while PC2 was to control the SOP of a pump laser diode. These PC1 and PC2 as well as the pump power gave a high flexibility in the generation and controlling the nonlinear dynamics of this laser. A 70:30 output coupler (OC) was used to output 30% of the cavity light. The SWCNT-SA which was used in this experiment is a high purity, high metallic content (CG200). A concentration of 0.2 mg/mL of CG200 was placed in deionized water with 2% of Sodium dodecylbenzenesulfonate surfactant. The solution was placed in an ultrasonic bath for about one hour at 130 W and 20 kHz. Large bundles and impurities were removed using ultracentrifugation. The resulting solution was mixed with Polyvinyl Alcohol (PVA) powder and placed in a Petri dish to form a SWCNT-PVA film. Then a 1mm x 1mm piece was placed as a sandwich between the two fibre connectors. The laser output from the 30% coupler was detected using an InGaAs UDP-15-IR-2_FC detector with a bandwidth of 17 GHz and recorded using a 2.5 GHz sampling oscilloscope (Tektronix DPO7254). The oscilloscope has the built-in option of a variable electronic filter for the incoming signal. An optical spectrum analyzer (Yokogawa AQ6317B) with a maximum resolution of 0.02 nm and radio frequency spectrum analyzer (Rohde and Schwarz) with a 3 Hz resolution were used to observe the optical spectrum and the RF line respectively.

For identifying the optical RW emergence mechanism, a 50-GHz fast photodetector (Finisar XPDV2320R) with a bandwidth of 33 GHz was used and its output was recorded with an 80 GSa/s sampling rate oscilloscope (Agilent DSOX93204A). The oscilloscope traces were recorded for 26 ms with an effective resolution of 12.5 ps per point with an amplitude resolution of 8 bits. To analyse the results using the spatiotemporal dynamics, the 26 ms oscilloscope traces were split into segments. The length of each segment is equal to the one round trip. Then these segments were processed as a matrix which providing the intensity evolution through 10000 round trip.

Due to the use of a SWCNT SA, self-started mode-locking can be easily achieved as soon as the lasing threshold (18 mW) was reached. The fundamental pulse repetition rate was 56.6 ns (17.67 MHz) (oscilloscope traces Fig 3.1 (b)). The optical spectrum of the mode-locking pulses (Fig. 3.1 (c)) has the shape typical for the soliton operation regime with clear

distinct Kelly sidebands in the spectrum. The main components of the spectrum were in wavelength near 1563.6nm, with a 3dB spectral bandwidth of 2.85 nm. The pulse duration is shown in Fig. 3.1 (d) is about 990 fs and the pulse profile has been fitted to a hyperbolic secant pulse profile. Correspondingly, the time-bandwidth product is 0.3481, indicating that the output pulse width is almost transformed limited. Fig. 3.1 (e) shows the RF spectrum which confirmed that the mode-locked laser regime has a high signal to nose ratio (>70dB).

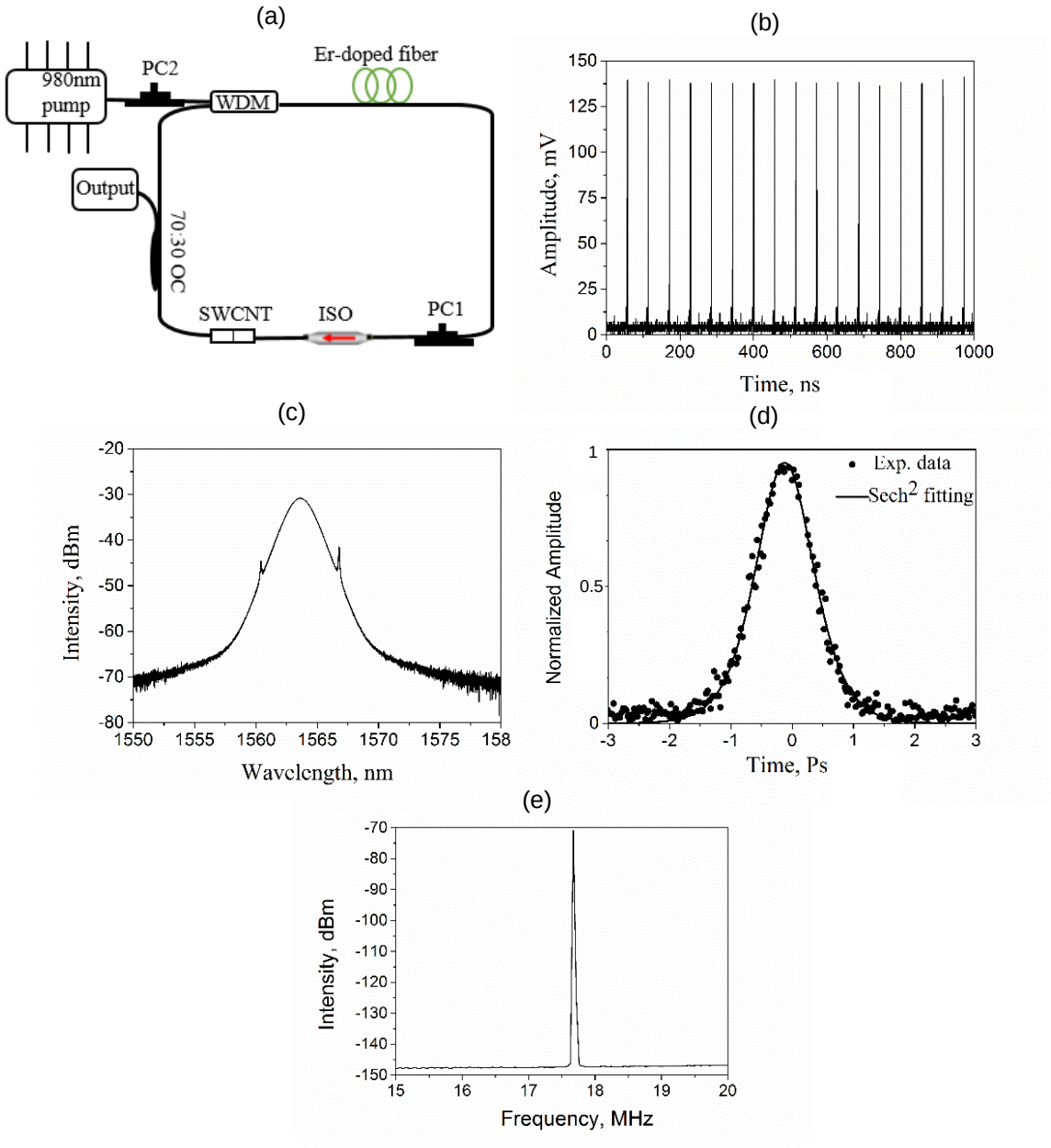

Fig.3.1: (a) The Experimental setup. WDM: wavelength Division multiplexing; PC: polarization controller; ISO: optical isolator; CNT: carbon nanotube SA; and OC: output coupler; (b) Mode-locked oscilloscope traces at 23mW; (c) Optical spectrum (d) corresponding pulse duration and (e) the RF spectrum.

3.3: High-Frequency Harmonic Mode-Locking Driven by Acoustic Resonances

In this section, the polarization role of the acoustic modes (R_{0m}, TR_{2m}) on the stabilization of HML has been addressed to generate a high HML (~GHz) based on SWCNT-SA for the first time. It was found that the characteristic of the HML in the proposed fibre lasers is that the pulse repetition rate increases with increase pump power and adjusting the polarization controller PC1. For example, with the proper adjustment of both PC1 and PC2, the first and second HML were obtained at pump powers of 27 mW and 29 mW respectively. Then multiple pulses from 3rd up to 51st are generated within the laser round trip as shown in Fig. 3.2 (b-e) with further increasing of the pump power and adjustment of PC1. For a pump power of 32 mW, the observed multi-pulsing which was transformed to HML with increased the pump power as follows: 14th harmonic (247. 38 MHz) at 63 mW, 42nd harmonic (742.14 MHz) at 138 mW and 51st harmonic (902 MHz) at 180 mW (Figs. 3.2 (c-e)) respectively.
The RF spectra for the sequence of ML and different HML regimes at different pump powers are shown in Fig. 3.3. The RF spectrum at a fundamental frequency f_1 =17.67 MHz at 23 mW (Fig. 3-3 (a), peak 1) has a peak-to-pedestal ratio of ~80 dB. Additional peaks (peaks 2) with spectral power in 30 dB smaller emerge at 63 mW at different frequencies. These peaks moved towards their centre of mass located at a distance of $f_1/2$ from the main peak with increased pump power and related to the birefringence depended satellites (adjustment by the PC1). The small peaks (peaks 3) are moving towards each other with increased pump power and adjustment of PC1.

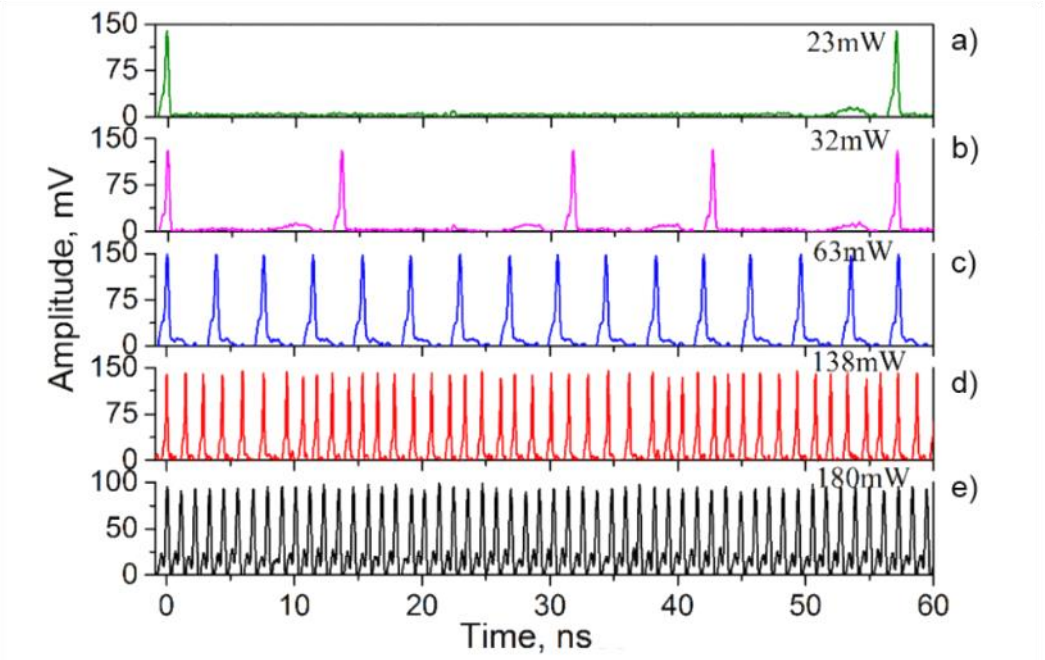

Fig. 3.2: (a) Oscilloscope trace of the output pulses at a different pump power; (a) 23 mW; (b) 32 mW; (c) 63 mW; (d) 138 mW; (e) 180 mW.

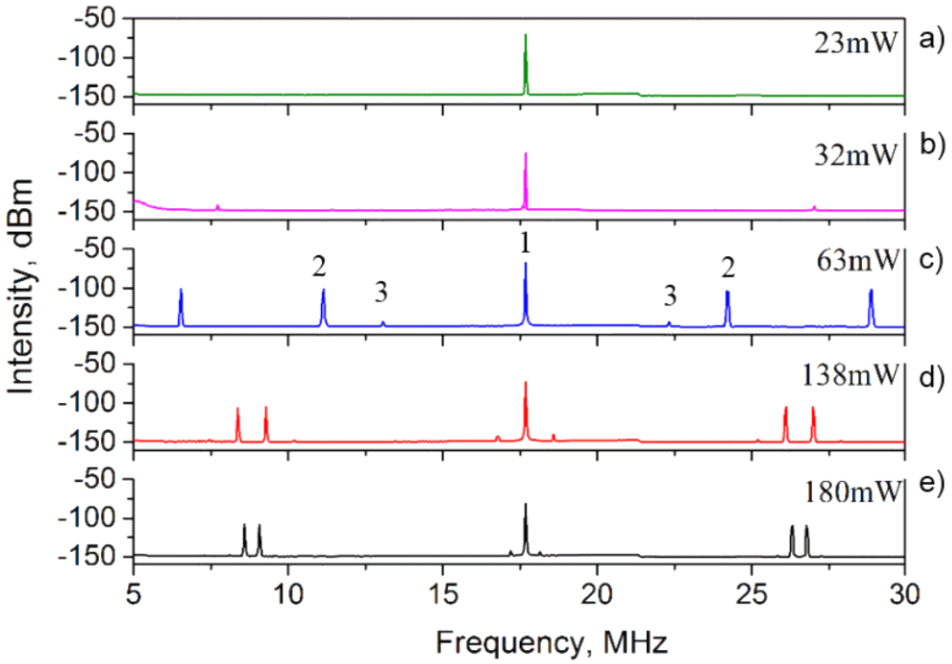

Fig. 3.3: RF spectrum of the output pulses at the different pump powers: (a) 23 mW; (b) 32 mW; (c) 63 mW; (d) 138 mW; (e) 180 mW.

The emergence of the birefringence-dependent satellites in Fig.3.3 means excitation of linearly polarized states along with the HML and excitation of acoustic mode TR_{2m}. Where there is an absence of polarization satellites as in Fig. 3.3 (b), the HML pulses distribute randomly inside the laser cavity (Fig. 3.2 (b)) due to the absence of the acoustic-optic effect. The adjustment of the two neighbouring polarization modulation satellites (Fig. 3.3 (c-e) leads to a resonance interaction via the induced acoustic-optic effect in the optical fibre which results in a stabilized order distribution of soliton multi-pulses (HML) in the laser cavity as shown in Fig. 3.2 (c-e). It was found that it is very hard to match the two neighbouring polarization satellites as it reaches a limit space and the repulsive far from each other. Also, the matching of the polarization satellites with the fundamental frequency or even near to it leads back the laser to emit normal mode-locking regimes. However, the RF peak-to-pedestal ratio of the 51st harmonic is about 68dB as shown in Fig. 3.4. The linewidth of this harmonic laser line is 50 KHz. The optical spectra of the HML regimes are illustrated in Fig.3.5; the optical spectrum (OS) was centred at about 1564 nm at low pump power (Fig. 3.5 (a-c)) and then shifted towards 1562 at higher pump power (Fig. 3.5 (d, e)). Also, the spectrum at a pump power of 63 mW (Fig. 3.5 (c)) exhibits a strong CW feature which may have appeared as the result of the polarization and pump power satellites explained in Fig. 3.3 (c). The CW component has increased as two CW lines appeared at increasing the pump power to 138 mW Fig. 3-5 (d). These two CW components became closer (Fig. 3.5 (e)) to each other exactly as the two neighboured polarization satellites in Fig. 3.3 (e). In addition, Fig. 3-5 (e) shows many sidebands in the optical spectrum.

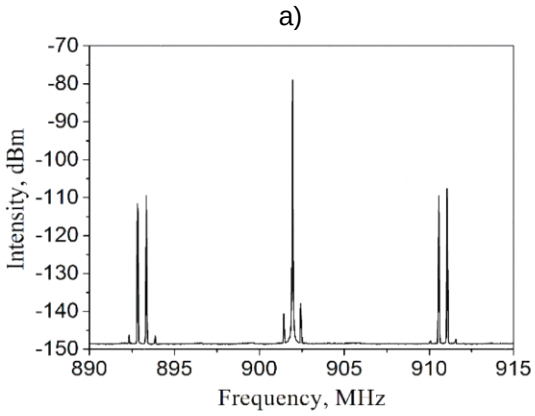

Fig. 3-4. The RF spectrum of the 51st HML pulses.

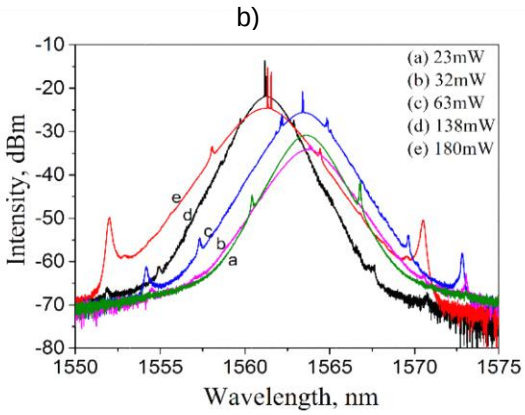

Fig. 3-5. Optical spectra of the HML at the different pump powers: (a) 23 mW; (b) 32 mW; (c) 63 mW; (d) 138 mW; (e) 180 mW.

Figure 3.6 (a) shows the obtained output pulse repetition rate and the harmonic order that was measured as a function of the pump power. The pulse repetition rate changes almost linearly from 17.67 MHz to 902 MHz together with the harmonic order. The pumping efficiency which is defined as the obtained HML frequency divided by the optical pump power was estimated to be ~5.44 MHz mW^{-1}. Figure 3-6 (b) shows the average output power and pulse energy that were measured. The maximum average power was 37.2 mW at a maximum pump power of 180 mW. The pulse energies of the output pulses were in the range from 38 to 97 pJ.

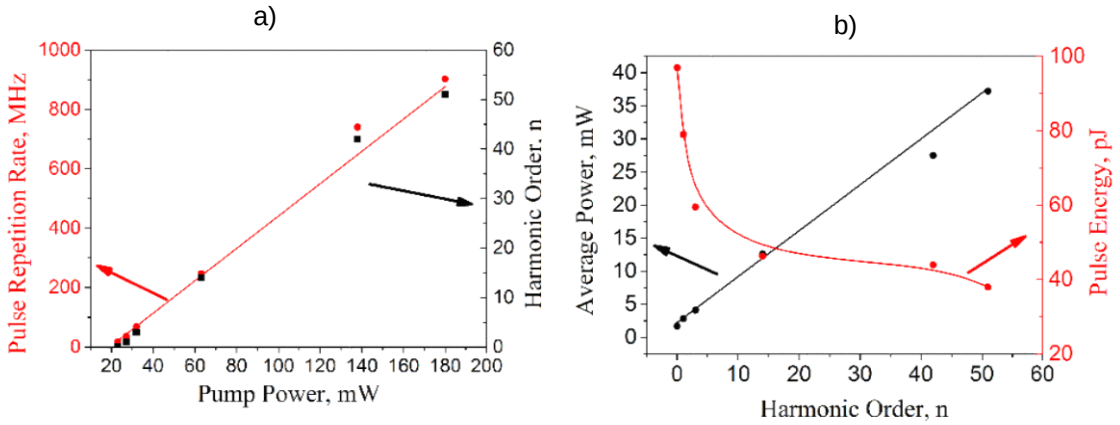

Fig. 3.6: (a) Pulse repetition rate and harmonic order of the output pulses as a function of the pump power; (b) average output power and harmonic pulse energy as a function of harmonic order (n).

The polarization properties of the HML have been studied using the same polarimeter that was used in chapter 2. It was employed to measure the normalized Stokes parameters S_1, S_2, S_3 and DOP. The intra-cavity polarization controller was tuned to achieve a high HML through excited high TR_{2m} modes. The polarization dynamics for the HML regimes are shown in Fig.3.7.

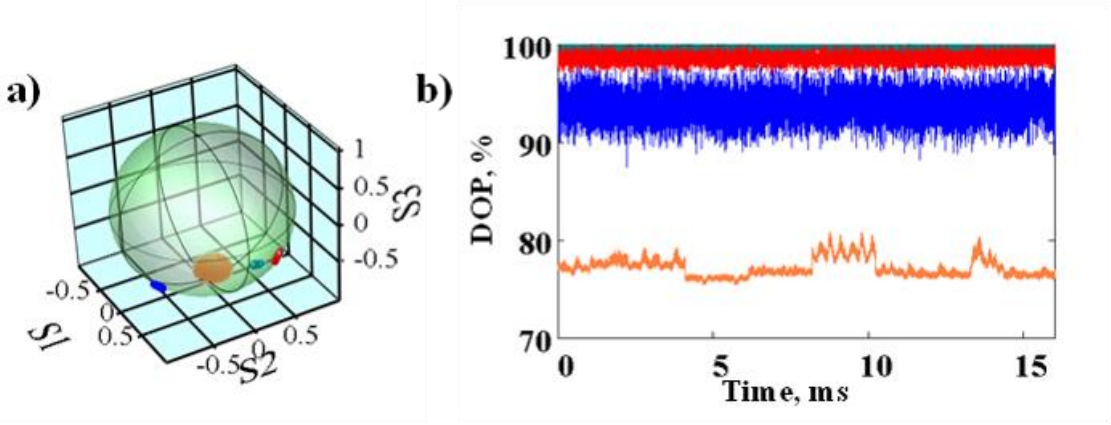

Fig. 3.7: The SOPs (a) and DOPs (b) for different pump powers: 23 mW (blue), 32 mW (green), 138 mW (brown), 180 mW (red).

The Stokes parameters on the Poincaré sphere shown in Fig. 3.7 (a), is related to the polarization attractor at the Poincaré sphere in the form of a fixed point for all the generated HML regimes. This fixed point indicates a stable operation for all the HML pulse trains with the axis defined by the S_1, S_2, and S_3. It was found that at 32 mW, the SOP is horizontal linearly polarized (both S_2 and S_3 are nearly equal to zero) and at 63 mW is linearly polarized at 45 (as both S_1 *and* S_3 are nearly equal to zero). But, with the clear appearance of the polarization modulation satellite (excited TR_{2m} modes) at 138 mW, the SOP has switched to left circular polarized (both S_1 *and* S_2 are nearly equal to zero). While at 180 mW, where the high HML generated (902 MHz), the SOP starts the change to the elliptically polarized. Fig. 3.7 (b) shows the DOP for the HML pulse train which indicates that these regimes are quite stable as it has a high DOP (more than 90% for 23, 32, 63 and 180 mW) while 78% for 138mW. The S_1, S_2, S_3 and DOP remained practically unchanged for all of the high order harmonic regimes, but the location of the point on the Poincaré sphere is changed.

3.4: Low Threshold Solitons Rains

In this section, using the same laser experiments described in section 3.2, we describe for the first time the observation of low-threshold power soliton rain in a mode-locked fibre laser based on SWCNT-SA. The proposed fibre laser can easily achieve a mode-locking regime due to the use of SWCNT-SA and the soliton optical spectrum accompanied with CW features were shown in Fig.3.5 in section 3.3. The gradual transition from the CW regime to the ML regime has been done by increasing the pump power to about 20 mW. The pulses are shaped into soliton operation regime with distinct Kelly sidebands in the spectrum as shown in Fig. 3.8 (a) (red). At the same pump power and given initial orientation of the PC1, it was found that the laser operates in a weak or partially mode-locked regime with the pre-existing CW components as shown in the optical spectrum illustrated in Fig. 3.8 (a) (black). This is because the cavity's anisotropy is changed by rotating the PC1. These CW

components accompanied with the mode-locked regime consist of a fluctuating noisy background that forms soliton rain around the cavity. The main components of the spectrum were in wavelength range around 1568 nm, with a 3 dB bandwidth of 4 nm.

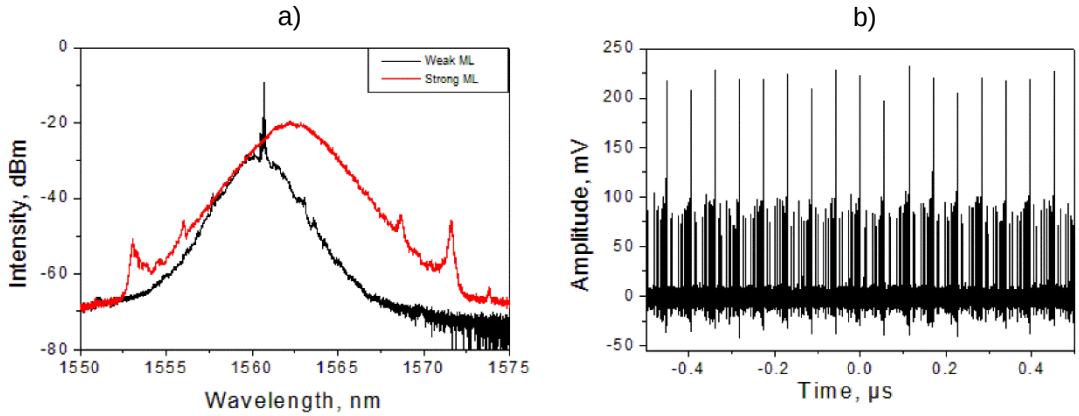

Fig. 3.8: a) the optical spectrum of the normal mode-locked regime (red); partial mode-locked regime (black); b) Oscilloscope trace of the soliton rain regime.

It was also noticed that, when the CW noisy background was minimized towards zero by further rotation of PC1 towards the mode-locked regime, the soliton rain disappeared. At a particular PC1 setting and hence cavity birefringence, an interesting dynamic intermediate pattern, soliton rain, is observed where the CW components and soliton pulses coexist in the cavity as shown in the oscilloscope traces in Fig. 3.8 (b). This CW component producing noisy and inhomogeneous background fluctuations in the laser cavity which lead to the formation of small pulses like the way droplets form in a vapour cloud [10]. When these are amplified they drift toward the main pulses (condensed phase) with a nearly constant relative velocity as can be seen in the Fig. 3.8 (b).

Indeed, soliton rain is formed in the laser cavity due to the interaction between three elements: the CW noisy background, the drift of the small soliton pulses and the condensed phase. The noisy background could be produced by cavity CW modes, amplified spontaneous emission (ASE) and dispersive waves produced by solitons. Soliton drifting is due to the propagation of the small pulses formed in the laser cavity with a low constant speed of the order of 10 m/s due to non-uniform background levels and this leads to collisions with the condensed soliton phase. While the condensed phase is a bunch of several tens of solitons which aggregate close to the main pulse.

Fig. 3.8 (a) shows a combination of mode locking and background components in the optical spectrum with the presence of a quasi-CW spike in addition to the resonant radiation waves symmetrically located with respect to the centre of the spectrum This mixing of field components is also apparent in the temporal domain (Fig. 3.8 (b)), which reveals an inhomogeneous background. Importantly, the fraction of the weakly coherent background could be gradually varied by tuning the cavity parameters, such as the intra-cavity

birefringence and pump power. It was found that the observed soliton rain can be controlled by both the intra-cavity birefringence (PC1) and the pump power.

3.4.1: Controllable Soliton Rain by Intra-Cavity Birefringence

By increasing the pump power to about 23 mW with an appropriate PC1 setting, the cavity birefringence could be altered, and an interesting dynamic pattern could be obtained. An evolution of soliton rain dynamics can be observed in the oscilloscope traces of the Fig. 3.9. This is because by rotating PC1, the cavity's anisotropy has changed. The CW component in the optical spectrum (Fig 3.8 (a)) accompanied with the laser pulses indicates that the laser is operating in a partial mode-locking regime. It was found that the flow and the number of the solitons emitted can be controlled by tuning PC1. For example, when only a few small pulses (1-4) are observed, these drift towards the main pulses as shown in Fig. 3.9 (a-c) respectively at a different PC1 setting. The amount of soliton rain emitted increased noticeably when a so-called condensed phase appeared close to the main pulses as shown in Fig. 3.9 (d) and became very heavy with fast drifting in the cavity in Fig. 3.9 (e, f) at another setting of PC1. These soliton pulse trains are composed of two parts; a soliton condensed phase part and a flow part; the solitons are constantly moving from the soliton condensed part. Therefore, when small pulses were triggered by the oscilloscope, it was found that these small pulses would drift towards the main and collide with it and rise again from the noisy ground after the collision. It was also found that when tuning PC1 to a position where the CW component disappeared as shown in Fig. 3.8 (a) (red), the rain stops almost immediately. In addition to controlling the appearance and disappearance of soliton rain, it is possible to tune the soliton drifting direction and speed by adjusting PC1. Moreover, a bunch of pulses or like a burst of soliton rain (Fig. 3.9 (g)) has also been found at this pump power, but at a different position of PC1. In this situation, the distribution of these burst pulses inside the bunch is constantly moving from one round trip to the next. In the beginning, the travelling bunch of pulses becomes chaotic due to the CW fluctuation. But, with appropriate tuning of the PC1, freezing of these fluctuations could be achieved, thus possibly controlling the formation of soliton rain.

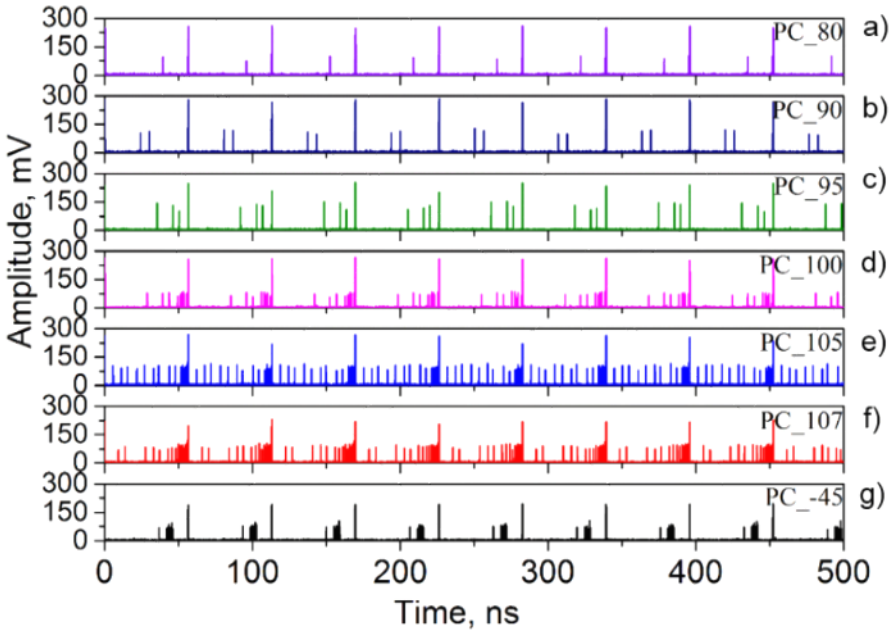

Fig. 3.9: Oscilloscope traces of the soliton rain at different intra-cavity polarization controller positions; a) PC1=80^0; b) PC1=90^0; c) PC1=95^0; d) PC1=100^0; e) PC1=105^0; f) PC1=107^0; g) PC1=-45^0.

The RF and optical spectra measurements of the emergence of soliton rain by tuning PC1 dependent are labelled from 1 to 7 in Fig. 3.10 (a, b). These results show that there is no big difference between regimes as the RF spectrum is nearly the same as the RF spectrum of the HML in Fig. 3.3 where the slow and fast two orthogonal polarization satellites appear at the same places at roughly *f*/2 except for the last case at PC_-45^0. Here both RF and optical spectra show the satellites became closer to the fundamental laser line with small noisy features on the optical spectrum.

Therefore, when the soliton rain starts above a certain level of CW background fluctuations, it is possible to control its appearance. Indeed, the detailed features of soliton rain are the size of the condensed phase, the number of drifting solitons and their drifting velocity and most of these features can be adjusted by changing the PC1 setting.

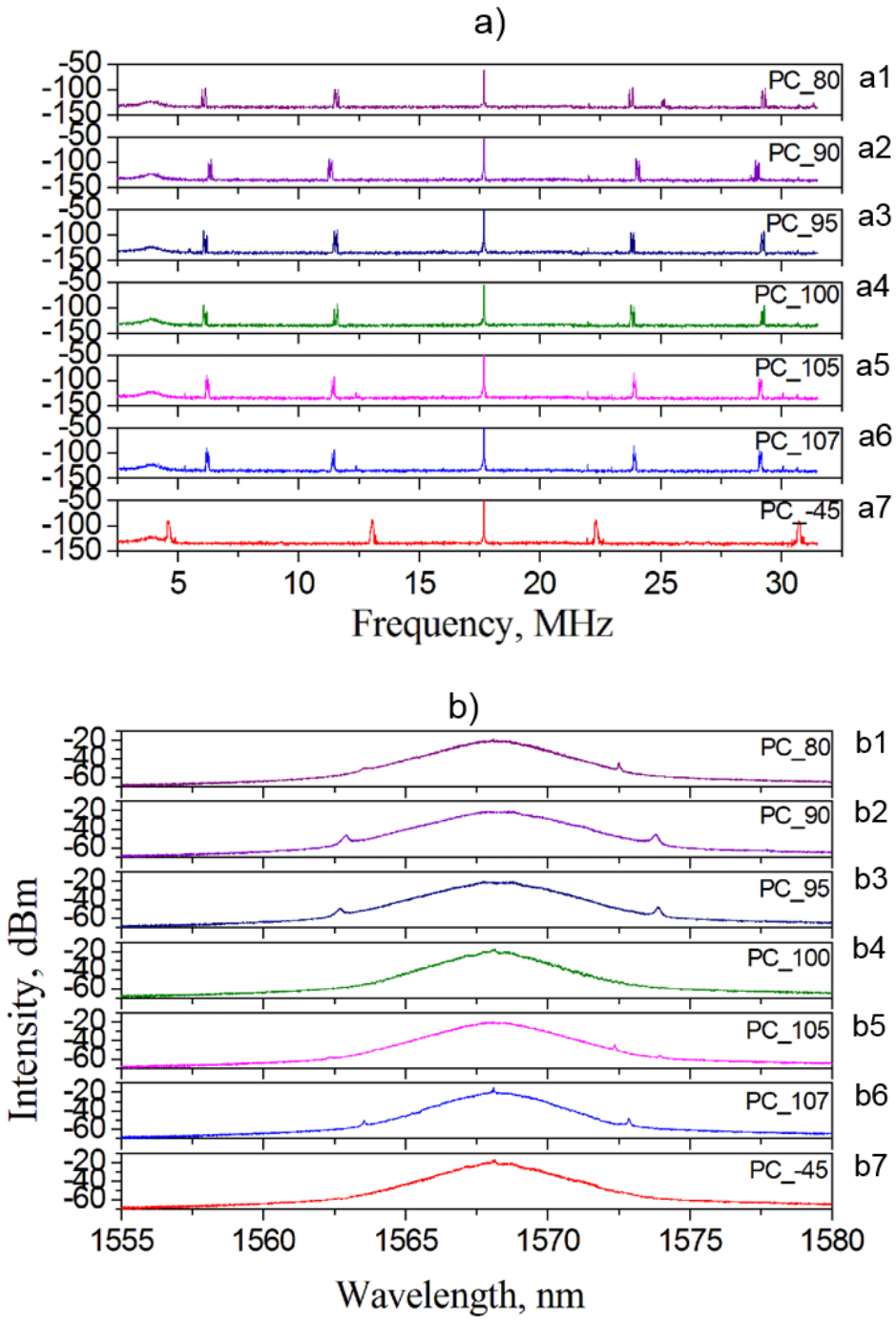

Fig. 3.10: (a) RF spectrum of the output pulses and (b) optical spectrum at the PC1 positions: (1) PC1=80^0; (2) PC1=90^0; (3) PC1=95^0; (4) PC1=100^0; (5) PC1=105^0; (6) PC1=107^0 and (7) PC1=-45^0.

3.4.2: Controllable Soliton Rain by Pump Power.

In this experiment, fundamental mode-locking was firstly obtained through tuning the pump power to 23 mW and appropriately adjusting the PC1. Then by adjusting the PC1 to a soliton rain regime and fixing it in this position, it was found that the number of solitons formed in the cavity continuously increased by increasing the pump power as illustrated in Fig. 3.11. Indeed, the increase of the pumping power increases the level of the CW fluctuations in the

background. When the pumping power is sufficient to trigger small flowing pulses, the soliton rain starts initially with a few of drifting solitons at a time per cavity round trip and 1, 3, 4, and 5 have also observed as shown in Fig. 3-11 (a-d) respectively. Increasing the pumping power further to 40 mW (Fig. 3.11 (e)), the number of drifting solitons increases, and the pulse train appears as a group of pulse bursts. At 42 mW of the pump power, soliton rain becomes heavy (Fig. 3.11 (g)) which tends to aggregate into a sub-nanosecond pulse bunch. At the same time, a significant fraction of the energy of the cavity remains in the quasi-CW background. When the pump power was increased to 94 mW (Fig. 3.11 (h)), it was found that the probability that two solitons are created closer together becomes significant. Thus, interactions between neighbouring drifting solitons can occur which could be a trigger for the emergence of optical RWs. The sequence of RF and optical spectra measurements on increasing the pump power are illustrated in Fig. 3.12 (a, b) over 7 steps labelled 1-7. These spectra show that there is a clear difference between these regimes compared to the RF spectra of different PC positions in Fig. 3.10. Here the slow and fast two orthogonal polarization satellites are not fixed in position and the spectrum is accompanied with some noisy features while the optical spectra exhibit from the high Kelly side-band which refers to the effect of the nonlinearity in the laser cavity. The adjustment of the two neighbouring Kelly side-bands leads to the frequency resonance interaction in the optical fibre which results in disorder distribution of the soliton multi-pulsing.

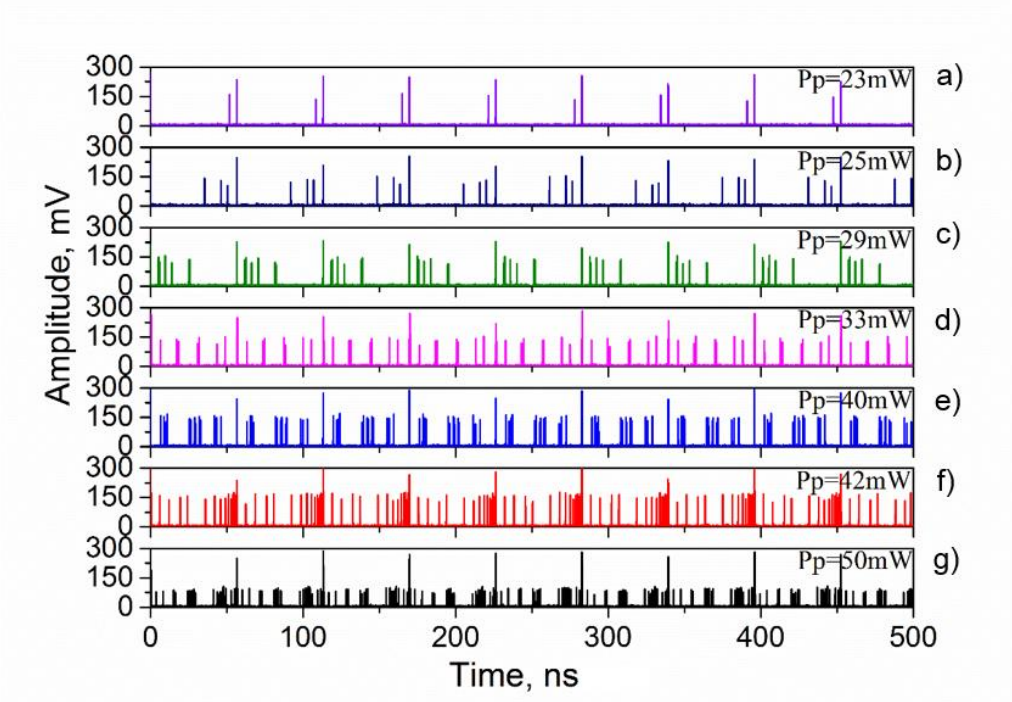

Fig. 3.11: Oscilloscope traces of the soliton rain at different pump power; a) 23mW; b) 25 mW; c) 29 mW; d) 33 mW; e) 40 mW; f) 42 mW; g) 50 mW.

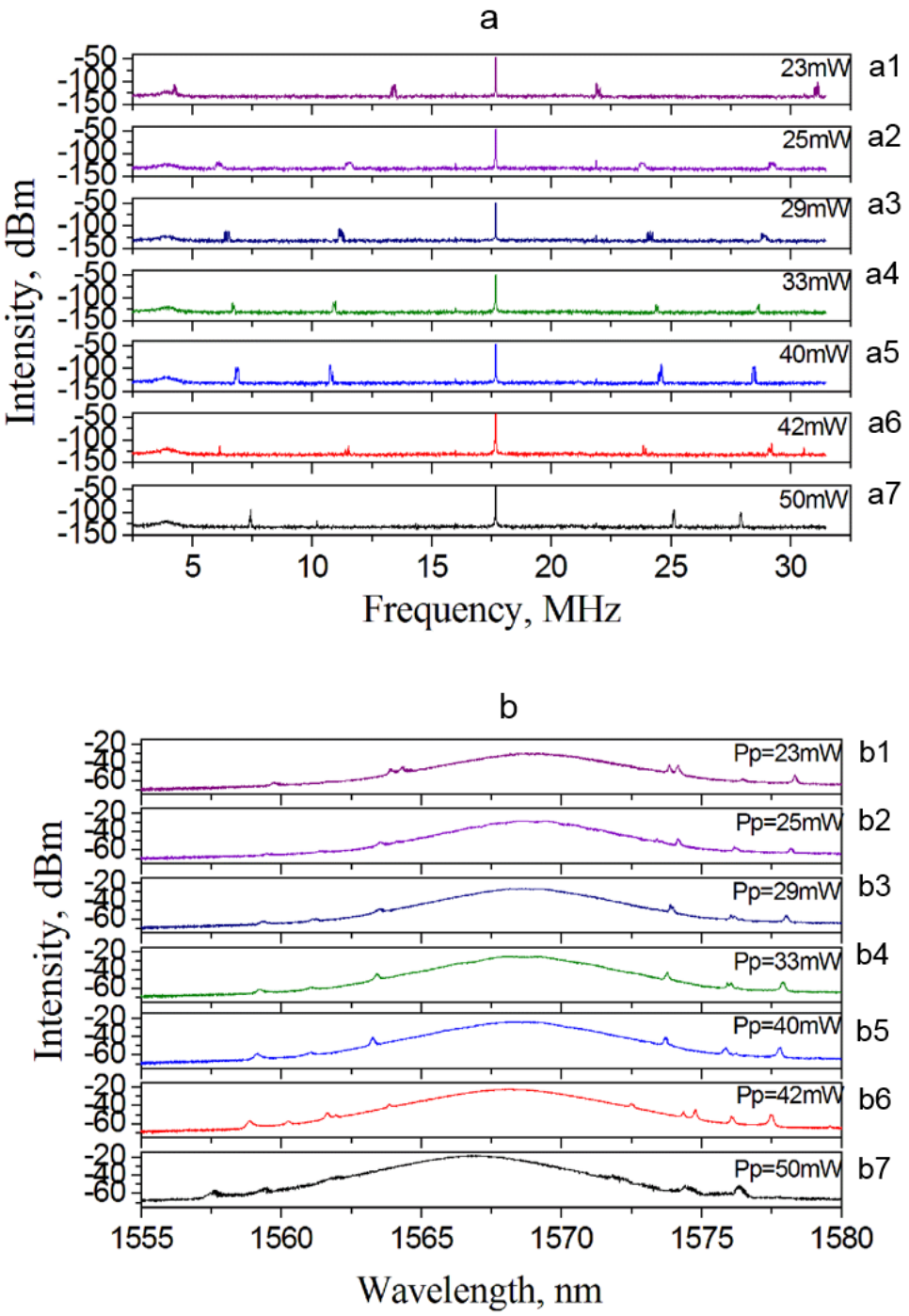

Fig. 3.12: (a) RF spectrum of the output pulses and (b) optical spectrum at the different pump powers: (1) 23 mW; (2) 25 mW; (3) 29 mW; (4) 33 mW; (5) 30 mW; (6) 42 mW and (7) 50 mW.

3.5: Soliton Rain Harmonics

In addition to controlling the numbers of the soliton rain and its appearance, harmonics of the soliton rain have also observed at relatively low pump power (160 mW-200 mW). The fundamental, first, and second harmonic soliton rain have been observed as illustrated in Fig. 3.13 (a-c) and these correspond to different positions of PC1 with the same pump power (for harmonics 160 mW). Tuning the PC1 in the laser cavity will control the effective non-

linear transfer function and generate an increase or decrease in the level of background and radiation (CW) that accompanies the soliton pulses. Therefore, the existence of soliton rain harmonics is due to the instability of the condensed phase when its size exceeds a certain level which is typically more than 30 solitons. The condensed phase then breaks into parts, and each new condensed part becomes related to its own background part that produces drifting solitons [10]. Increasing the pump power to about 200 mW leads to the appearance of a high harmonic soliton rain as illustrated in Fig. 3.13 (d). The pulse-pulse interaction becomes important as the probability that two or more neighbouring drifting solitons become sufficiently close together when the pump power is increased beyond 100 mW.

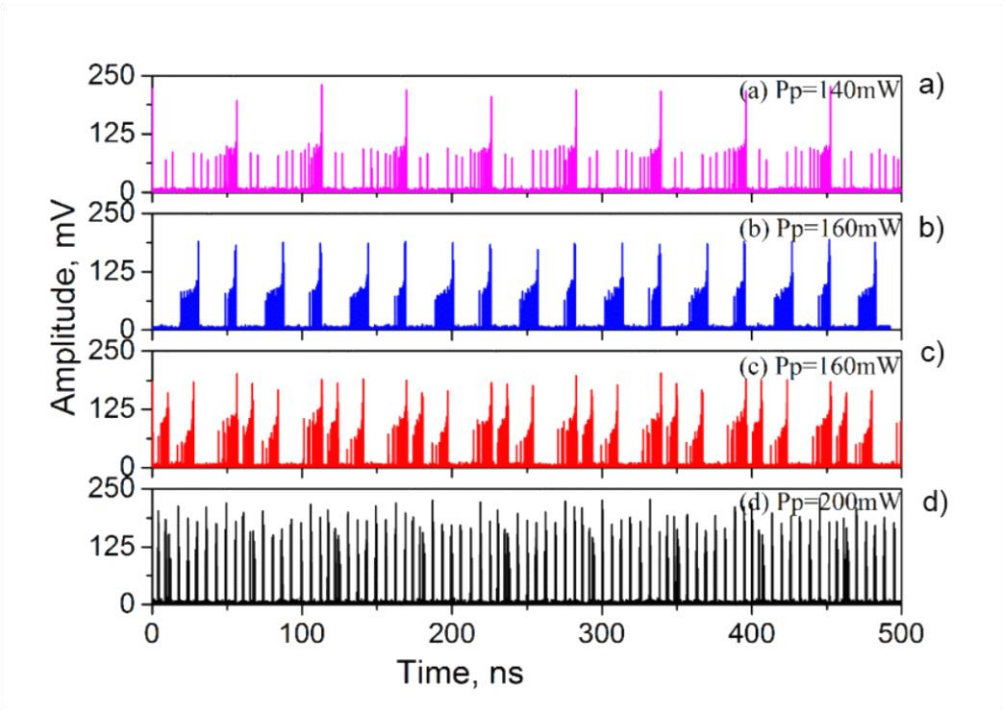

Fig. 3.13: Harmonic soliton rain at three different pump powers, a) 140 mA; b) 160 mW; c) 160 mW at another PC1 position and d) 200 mW.

The optical spectrum of the first and second harmonic are placed within the fundamental pulse and centred at a wavelength of about 1567 nm as in Fig. 3.14 (a, b). Two sets of spectral sidebands appear on the spectra. The one was the Kelly sidebands which confirmed that the mode-locked pulses were solitons. Apart from the Kelly sidebands, there was another set of sidebands. This set of sidebands exhibits peak-dip alteration in the polarization resolved spectra and its appearance was a result of the phase matching (coherent energy exchange) between the two orthogonal polarization components of the vector solitons. While it seems that the phase matching (incoherent energy exchange) has been destroyed and the pulses propagate chaotically at a pump power of 200 mW (Fig. 3.14 (c)) as the Kelly sidebands have disappeared as well as the central peak shifted to 1562 nm.

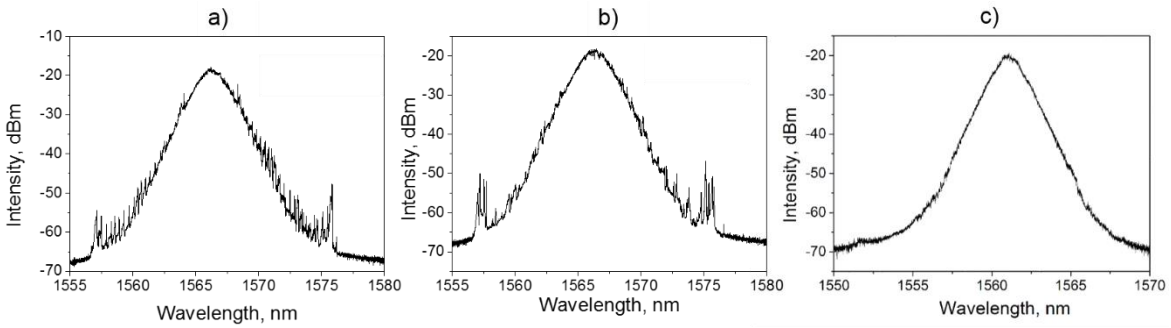

Fig. 3.14: Optical spectrum analyzer of a) first harmonic at 160 mW; b) second harmonic at 160 mW and c) high harmonic at 200 mW of the soliton rain regimes.

3.6: Soliton Fission

As can see from previous sections, the output soliton dynamics in laser systems are complicated and depend considerably on the laser parameters. Therefore, the evolution of laser can be switched from one stable state such as the mode-locked regime to another regime such as HML, low threshold soliton rain, harmonic soliton rain or soliton rain with interactions by controlling either the intra-cavity birefringence or the pump power. However, under certain circumstances, solitons can mergence into a single pulse during soliton collision which is a principal feature of soliton fusion. Because of soliton fusion, a high-intensity robust light structure arises and propagates over significant distances without recovering to the initial solitons. Soliton fusion has also been considered as one of the optical RW generation mechanisms.

In this section, the experimental observation of temporal signatures of soliton fission has been demonstrated using the same fibre laser experiment. Specifically, clear soliton pulse fission signatures were observed in measurements of shot-to-shot intensity that is operating in a transition regime between soliton rain and chaotic emission. The soliton pulse fission appears at a pump power of 116 mW when the laser operates in this transition zone, between soliton rain emission and chaotically. We have observed clear time-domain signatures of pulse explosion events with sharp temporal shifts. Interestingly, it was observed that the temporal envelope (Fig. 3.15 (a)) shows that soliton fission is similar to the onset of many pulsing. It can identify clearly many soliton fission events, each displaying qualitatively similar characteristics. Indeed, the several pulses can be seen to develop at the trailing edge of the fundamental laser pulse. It can be shown that the soliton pulses fissions manifest themselves as abrupt temporal shifts in the output pulse train. Also, during the fission, the soliton laser pulse and optical spectrum underwent dramatic changes and did not return to the steady state afterward. The output spectrum which is shown in Fig. 3.15 (b) shows that the spectra of all the pulses are placed within the fundamental peaks which is centred at about 1563 nm. As the laser operates in soliton regime, the laser spectrum shows week Kelly sidebands from week phase matching between the solitons.

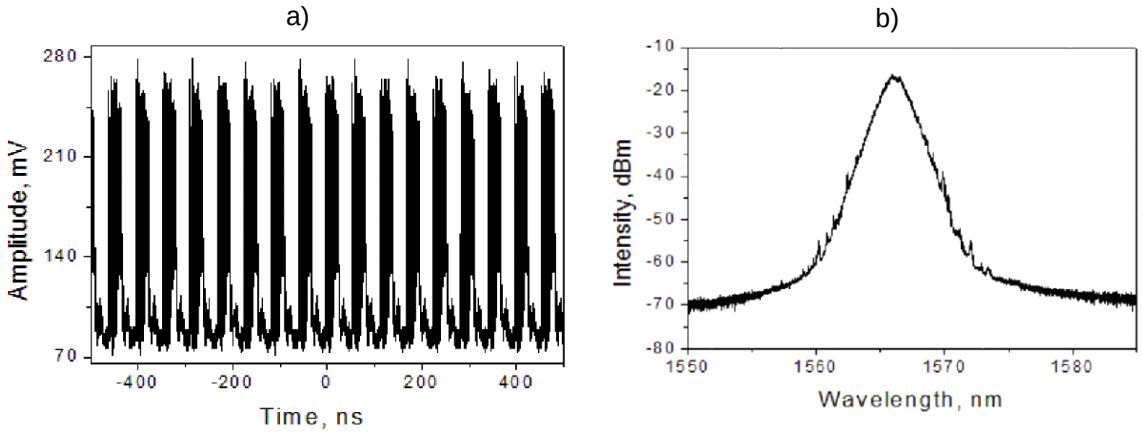

Fig.3.15: a) Oscilloscope trace and b) optical spectrum of soliton fission.

The laser pulse output has also been investigated when the laser was operating in the soliton fission regime by recording 26 ms of oscilloscope traces with 12.5 ps resolution. By dividing the recorded real-time signal into segments whose duration equals the average cavity round trip time, clear sharp pulse temporal shifts were observed by plotting 10000 round trips of the real-time signal in Fig. 3.16 (a). It was found that the main pulses splitting into many pulses that occupied the whole laser cavity due to the soliton fission in the main pulse. The spatiotemporal intensity measurements also show, the interaction processes between solitons inside the main pulse can be clearly captured and it is found that nonlinear soliton fission accounts for optical RW generation in this SWCNT-SA passive mode-locking fibre laser. As seen in Fig. 3.16 (b), there are many interactions between solitons inside the main pulses. For instance, it was found that two soliton-fission that are placed near 35 ns ejected many solitons that are static in the laser cavity. It is also found that around 34.5 ns, two solitary pulses interact with each other rather than quasi-elastic collision when the temporal and frequency separation between two solitons is small. It can be seen that optical RWs which are generated from soliton collisions can propagate for over 1000 consecutive round trips indicating a lifetime of over 56 μs. In the repulsion case, two solitary pulses have been found to propagate independently after the interaction. Because conditions for the soliton interaction are extremely delicate, the interaction itself is a very rare event as confirmed by PDF histogram statistic. The PDF (Fig. 3.16 (c)) confirms the generation of optical RW events as results of soliton fission. Indeed, instead of using high pump power in NPR or double-cladding fibre lasers, and long cavity fibre laser, our SWCNT-SA passive mode-locked fibre laser can produce a multiple-soliton state as a result of soliton fission with solitons spreading across the whole cavity under low pump power. Also, it was found that the soliton fission regimes are affected by the pulse polarization evolution in the cavity. However, the peculiar feature of the RWs which emerge from soliton interaction is the very slow changing of the amplitude over a long period after the two solitons have merged (over 2000RT before optical RW emerged at 34.5 ns in Fig. 3.16 (b)). Also, as characteristics of

the soliton fission process, soliton interactions joint two solitons into a single giant solitary pulse that propagates while maintaining its shape and intensity of about double the original soliton value (red colour).

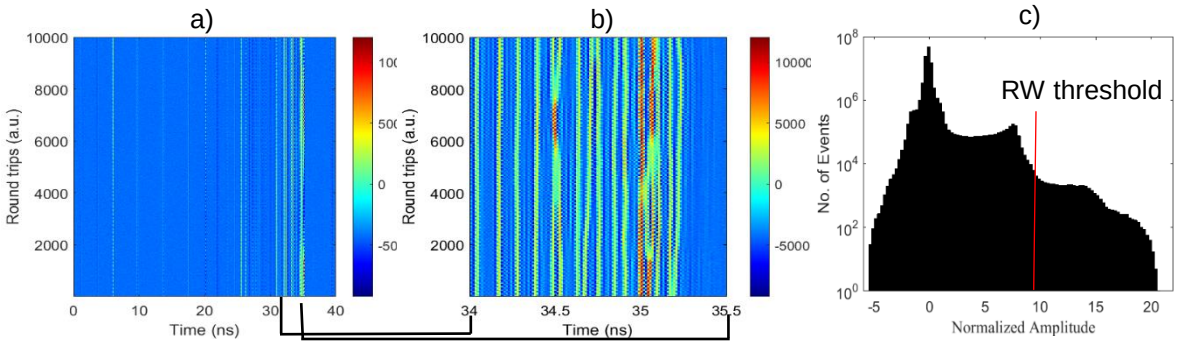

Fig. 3.16: a, b are the spatiotemporal intensity evolution; and c the PDF of the soliton fission at pump powers 116 mW.

Soliton fusion also occurred due to soliton interactions between co-propagating solitons with small temporal spacing, small frequency separation, and the appropriate phase difference. However, as in most SR regimes, soliton fission can be controlled by adjusting the pump power and the intra-cavity polarization. The modulation instability formed by PC1 can trigger the laser pulse to explode into many pulses when the pump power is in the range for which fissions occur. Therefore, soliton fusion refers to the process where many adjacent soliton pulses are merged into a single pulse.

Also, depending on the pump power and intra-cavity birefringence, multi-soliton pulses strongly influence the interactions between them and then the solitons are not static and randomly distributed resulting a chaotic soliton bunch in the laser cavity (Fig.3.17 (a)). Consequently, soliton fusion could also be accelerated because of multiple interactions between solitons and dispersive waves (Fig. 3.17(b)). These two regimes that are observed at the same pump power (116mW), but at different PC1 setting have also induced optical RWs events (as confirmed by PDF in Fig 3.17 (c, d) from the multiple collisions and interactions inside the main laser soliton pulse. There is no big difference in the optical spectra of these two regimes compared with the regime in Fig. 3.15. The results show that the fusion process is quite sensitive to the initial conditions of the pump power and the intra-cavity birefringence of these parameters and because of the interactions, soliton pulses are merged together, where the resultant soliton pulse amplitude is significantly greater than the initial amplitude of other solitons. Therefore, the fusion of optical solitons can be regarded as a new scenario to generate optical RWs.

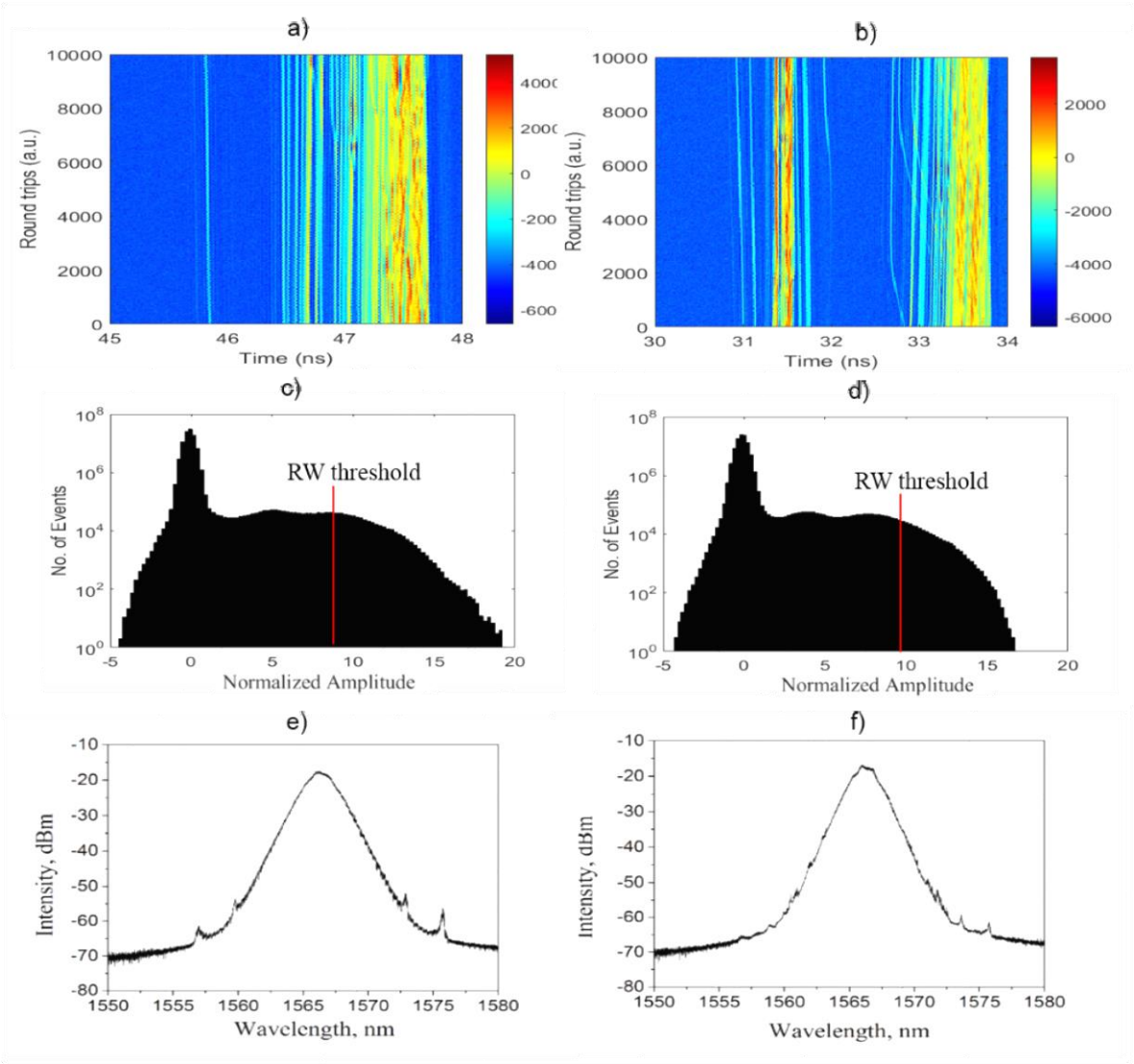

Fig. 3.17: a) and b) are the spatiotemporal intensity evolution; c and d the PDF histogram; e and f optical spectrum of the soliton fission at pump powers 116 mW and different cavity birefringence.

3.7: Soliton Rain Interactions

It was found that, when the pump power exceeds a certain value, for instance at values of 140 mW and 160 mW, and PC1 is set far from the harmonic soliton rain position, the distribution of bound soliton rain inside the cavity became very heavy and chaotic as shown in Fig.3.18 (a, b) for 140 mW and 160 mW respectively. This makes the laser pulses travel at different group velocities and hence they have a very high probability to interact with each other and initiate optical RW events. Moreover, energy dissipation of solitons is visible during the interaction processes. Some amount of the soliton's energy is transferred to dispersive waves. It has been confirmed that the RW events emerge from the soliton rain interactions by analysing the collected data using the spatiotemporal evolution as illustrated in Fig. 3.18 (c, d) for 140 mW, 160 mW respectively. Therefore, due to the interactions among solitons, soliton rain and CW, these multiple-solitons formed various dynamic patterns. Also, at higher pump power (160 mW Fig. 3.18 (d)), the pulses travel chaotically

with different group velocities that lead to crossed pulses with optical RW emergence for about100s of the round trip without energy exchanges. The PDF for all of these regimes yield a long tail shape which is far from the normal Gaussian distribution as shown in Fig. 3.18 (e, f). The output pulse intensities have been normalized to the amplitude normalization with RW threshold of 8 (red lines). It was also found that the optical spectrum exhibits noisy feature with the disappearance of Kelly sideband features when the RW emerged as shown in Fig. 3.19. It seems that the soliton pulses break up due to the CW features into many pulses that propagate chaotically due to having different group velocities in the laser cavity. Therefore, these nonlinear localized dynamics named soliton rain are formed due to the balanced in the nonlinear system through an energy exchange with the environment in presence of nonlinearity, dispersion, gain and loss which can be controlled by both the pump power and PC1. So, their existence and stability depend on the energy balance which can manifest conditions for self-organization.

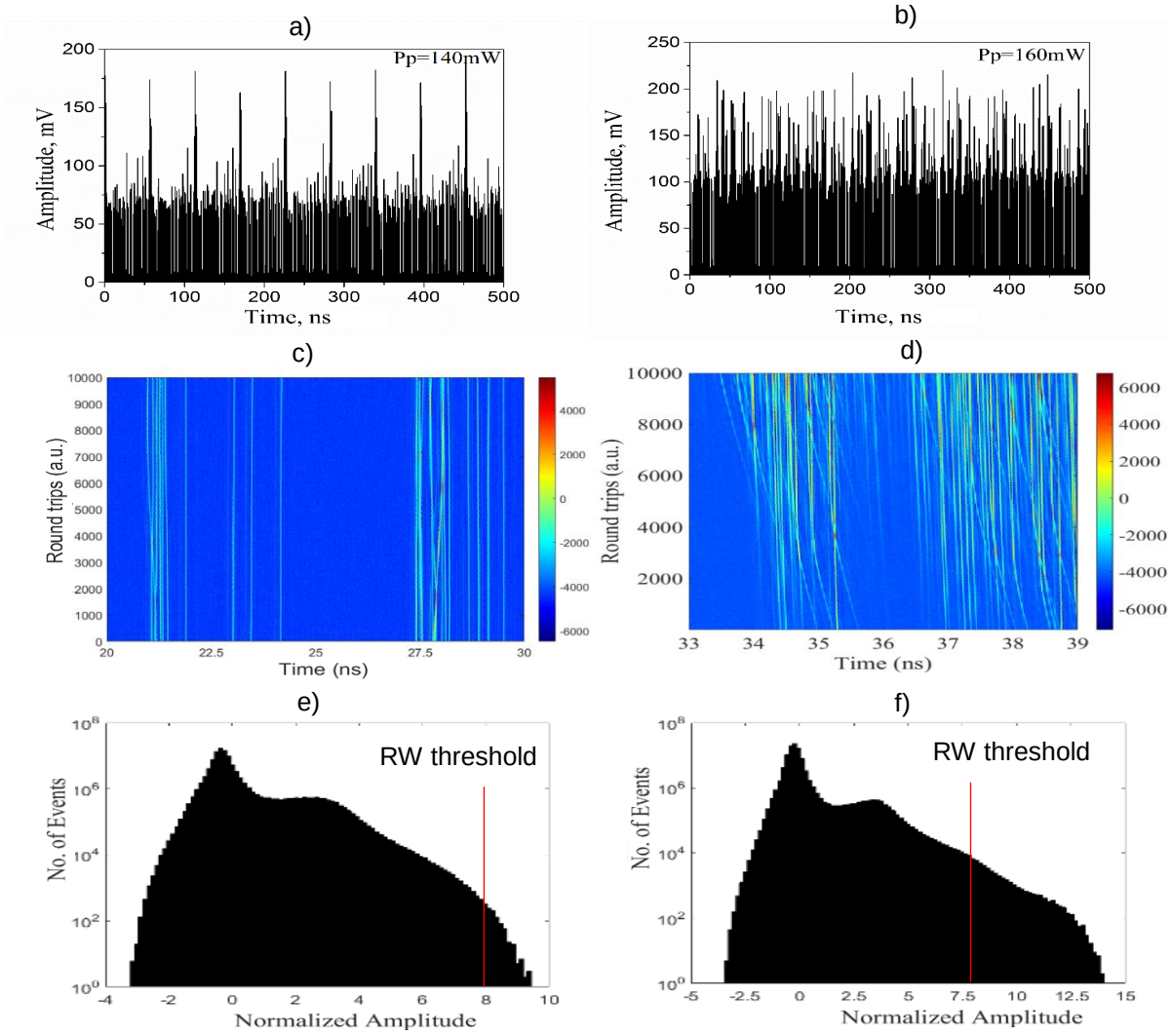

Fig. 3.18: a, b oscilloscope traces; c and d are the spatiotemporal evolution; e and f is the PDF of the chaotic soliton rain at two different pump powers (140 mW and 160 mW) respectively.

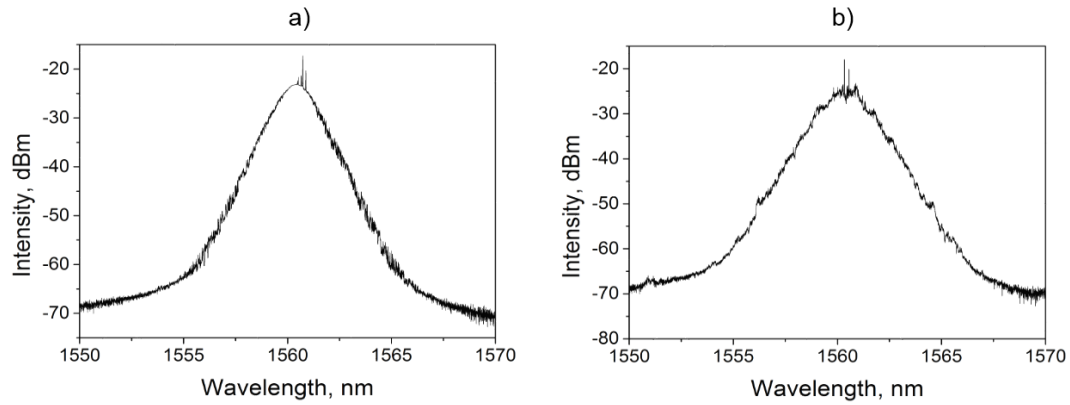

Fig. 3.19: Optical spectrum measurements of a) 140 mW and b) 200 mW.

3.8: Conclusions

In conclusion, high HML in a SWCNT-SA erbium-doped fibre laser using acoustic-optic effect has been demonstrated. Under different pump powers and appropriate adjustments of the polarization in the laser cavity, controllable HML from the first up to the 51st order have been obtained. The 51st order HML, corresponding to a repetition rate of 902 MHz, was obtained with an output power of 37 mW. The stability of HML is tested by the super mode suppression level which is as large as 68 dB and this means that the laser emits high-quality pulses with low energy fluctuations. The high HML fibre lasers are important in revealing the high-speed laser modulator, which is vital for fibre optic communications, all-optical clock recovery, frequency metrology and sensing applications.

In addition, using the same testbed fibre laser and by adjusting of the pump power and the intra-cavity birefringence, the control, appearance and disappearance of soliton rain flow at a low range of pump power have been demonstrated. Harmonic soliton rain, soliton fission and soliton interactions that lead to emergence of optical RW have also been obtained in this experiment at different level of pump power and intra-cavity birefringence. We have recorded the round trip-to-round trip pulses emitted by the laser, identifying clear soliton fission and soliton interaction signatures for optical RW formation as confirmed using both the spatiotemporal intensity evolution technique and the PDF.

The collected results from this testbed laser system could clear the way towards modelling the appearance of soliton rain as well as high nonlinear localized dynamics such as optical RW emergence. Also, it is an attractive area of research in the field of fibre lasers where much work has been done over the last few years which focused on the design of high-energy mode-locked fibre laser cavities. In addition, this nonlinear localized dynamic provides an excellent framework for studying and understanding complex pulse dynamics and could stimulate researchers to design new innovative cavity designs. It was found that passive mode-locked lasers are an ideal platform for testing the concept of dissipative solitons such as soliton rain, soliton explosions, dissipative soliton molecules and soliton pulsations.

Chapter 4

Vector Optical Bright-Dark Rogue Waves

4.1. Introduction

Nonlinear optical systems are amongst the most important tools in modern optics. These nonlinear optical systems provide the unique potential to artificially generate and study optical events in a highly controlled environment analogous to a range of events observed in nature from soliton propagation to extreme RW events. Many nonlinear systems exhibit an instability that leads to the modulation of the steady state through breaking the CW or quasi CW radiation into a train of short or ultrashort pulses. This phenomenon was thought to be the result of the interplay between the nonlinear and dispersive effects and is referred to as the modulation instability (MI). It was studied during the late 1960s and early 1970s in such diverse fields as fluid dynamics [117, 118], nonlinear optics [119-121] and plasma physics [122-124]. The CW mode is inherently unstable in the presence of anomalous dispersion ($\beta_2<0$) and this instability leads to a spontaneous temporal modulation of the CW beam and transforms it into a pulse train. MI can also occur in the normal-dispersion region ($\beta_2>0$) of optical fibres but only under certain conditions. These conditions turn out to be the presence of cross-phase modulation. This can occur when two optical beams propagate simultaneously at different wavelengths or with orthogonal polarizations. But, MI near to the zero dispersion region ($\beta 2\sim 0$) has not yet been studied. Hence, this chapter focus on studying of MI at zero dispersion system.

However, during the last two decades, the focus of researchers from many fields ranging from oceanography to the laser physics, has been on revealing the mechanisms of origin

of RWs with anomalous amplitudes. The mode-locked laser, as a test-bed system, provides a unique opportunity to collect more data on RWs in the form of periodic or random localized pulses as well as to clarify the mechanisms of RW emergence using a similar analysis shown in chapter 2 and chapter 3. Previously, in addition to MI, several mechanisms have been found that optical RWs events can be generated in the mode-locked laser at the time scale of round trip (RT). These mechanisms include soliton-soliton interactions through the overlapping of the soliton tails and soliton-dispersive wave interactions. All of the previous experimental observations utilizing this mechanism have reported the existence of either bright or dark RWs. The co-existence of the bright-dark RWs (BDRWs) has been recently predicted theoretically [55, 70, 72, 125] using coupled NLSE systems, but has never been observed experimentally in optics.

This chapter discusses the experimental results of the BDRW observation in a stretched (β_2~0) cavity mode-locked fibre laser. Clarifying the mechanisms of BDRW emergence are also discussed in this chapter. For the first time, we have demonstrated experimentally that in addition to the soliton-soliton interaction that is presented in the second chapter of this thesis and the soliton rain that is presented in the third chapter, a new type of vector RWs can emerge. The emergence of these RWs was driven by either MI or desynchronization (incoherent coupling) of the orthogonal linear states of polarization and leads to output power oscillations in the form of anomalous spikes-dips (bright-dark RWs). These results can pave the way to the unlocking the universal nature of the RWs origin and so it can be of interest to a broad scientific community. This chapter is organized as follows. In section 4.2 and section 4.3, the experimental set-up of a passive stretched-pulse mode-locked fibre ring laser and its characterization are presented respectively. BDRW such as Akhmediev, Peregrine and bi-periodic breathers that are driven by MI are demonstrated in section 4.4. The polarization evolutions of such breathers are demonstrated in section 4.5. In section 4.6 and section 4.7, BDRW driven by incoherent coupling of the orthogonal linear SOP due to the PI are validated. Finally, conclusions on these results and the emergence mechanisms are presented in section 4.8.

4.2: Stretched Passive Mode-Locked Fibre Laser Bright-Dark Experimental Setup

The fibre laser set-up used to observe optical BDRW is a passive stretched-pulse mode-locked fibre ring laser based on CNT-SA as illustrated in Fig. 4.1. The laser has a pump threshold of 14mW.

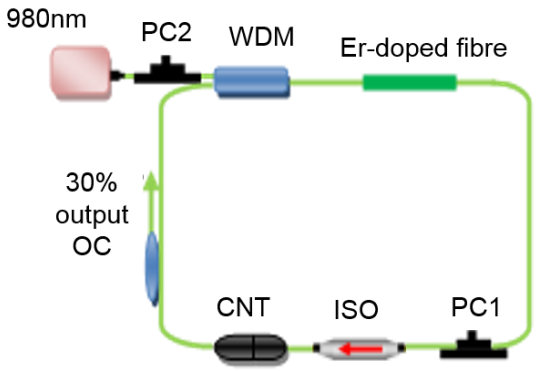

Fig. 4.1: The experimental setup of the stretched mode-locked fibre laser. WDM: wavelength Division multiplexing; PC: polarization controller; ISO: optical isolator; CNT: carbon nanotube SA; and OC: output coupler.

The laser cavity contained a 1.1m long EDF which is used as an active medium and has absorption of 80 dBm at 1530 nm with a second order dispersion (β_2) of +59 ps^2/km at 1550 nm and a 7.6 m SMF with a β_2 of −22 ps^2/ km. The net cavity dispersion was -0.04 ps^2/km. A 975nm laser diode was used to pump the EDF through a 980/1550 WDM. Unlike a mode-locking scheme based on nonlinear polarization rotation, we have used just one polarization controller inside the laser cavity (PC1) to control the laser cavity birefringence. Another polarization controller (PC2) was used to control the SOP of a pump laser diode. A polarization insensitive isolator (ISO) with 51dB attenuation was used to ensure unidirectional operation of the ring cavity. A standard 70:30 fused output coupler (OC) has been installed to redirect 30% of the laser light out of the cavity. Passive mode locking was realized by using a carbon nanotube (CNT). The CNT polymer composite film placed between two standard fibre connectors supplemented by the index matching for minimization of insertion losses. The output laser radiation from the 30% coupler is detected using a 50 GHz fast photodetector (Finisar XPDV2320R) with a bandwidth of 33 GHz and recorded by an 80 GSa/s sampling rate oscilloscope (Agilent DSOX93204A). The length of the recorded oscilloscope traces was 26 ms with an effective resolution of 12.5 ps per point and 8 bits of resolution. To analyse the results using the spatiotemporal dynamics, the 26 ms oscilloscope traces were split into segments with the length of each segment equal to one round trip. Then these segments were processed as a matrix which provides the intensity evolution through 10000 round trips. The output laser regimes have also been characterized using an RF spectrum analyzer (Rohde and Schwarz; 10 Hz-13.6 GHz) and an optical spectrum analyzer (Yokogawa AQ6317B). The resolution used in the RF and optical spectrum measurements are 3 Hz and 0.02 nm respectively.

The polarization dynamics properties have been studied using the same commercial polarimeter (Thorlabs IPM5300) that was used in chapters 2 and 3. The polarimeter is employed to measure the normalized Stokes parameters S_1, S_2, S_3, phase difference and DOP. We combined 16 slices of the temporal waveforms obtained by polarimeter to

calculate S_1, S_2, S_3, phase difference and DOP. All of these parameters are the function of the two linearly cross-polarized SOPs I_x and I_y output powers as in equation 2.1.

4.3: Laser Experiment characterization:

Firstly, the laser system was characterized by measuring the output laser power dependence on the laser pump power. It was found that the laser has a threshold of 14 mW (76 mA) as shown in Fig. 4.2; the maximum output power is 3 mW at a pump power of 40 mW. The laser was pumped with three different pump power groups during the experiments. The first group value (79-86 mA; 16.3 mW-20 mW) is only slightly above than the lasing threshold (76 mA; 14.12 mW). The second pump power group in the mode-locked laser regimes (88 mA-98 mA; 21.8 mW-28 mW). While the third pump power group values were at a harmonic mode-locked laser regime (beyond 98 mA; 28 mW). All of these three pump power groups are much lower than the pump power of 600 mW which was used to study optical RW observation in the laser mode-locked by NPR.

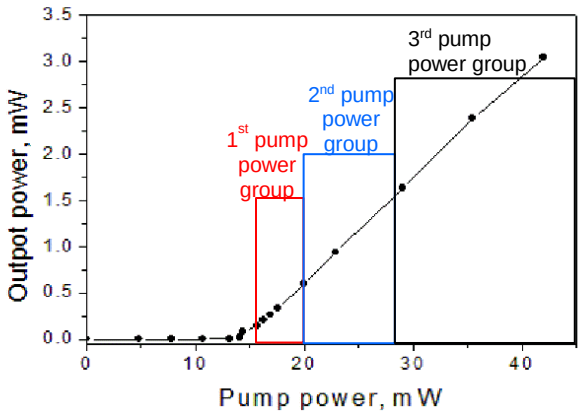

Fig. 4.2: The laser output power dependence on the pump power.

However, different laser regimes such as CW, mode-locked and multi-pulsing are triggered in this laser by adjusting the laser parameters which are the laser pump power, the polarization controller in the laser cavity (PC1), and the polarization controller that is placed outside the laser cavity (PC2).

Due to the CNT-SA, the laser immediately started emitting mode-locked pulses as shown in Fig. 4.3 (a) at about 19 mW (85 mA). The oscilloscope trace shows a stable single pulse per cavity round trip with the repetition rate of 33.2 ns of round trip time corresponding to the 30.135 MHz frequency central line that matched with the cavity length. PDF of this regime in Fig.4.3 (b) yield to a Gaussian shape which can confirm there are no fluctuations due to either polarization or MI. The corresponding optical spectrum profile at the laser output (Fig. 4.3 (c)), centred at 1565 nm and had a spectral bandwidth at full-width at half-maximum (FWHM) of 8 nm. The absence of distinct Kelly sidebands in the spectrum

indicates signature of the dispersion management (stretched) soliton operation regime. The autocorrelation results in Fig. 4.3 (d) shows the pulse duration is about 1.2 ps fitted to the hyperbolic secant pulse profile providing 1.05 time-bandwidth product that confirmed the stretched pulse mode-locked laser regime. Fig. 4.3 (e) shows the RF spectrum which confirmed that the mode-locked laser regime has a high signal to nose ratio (>65dB).

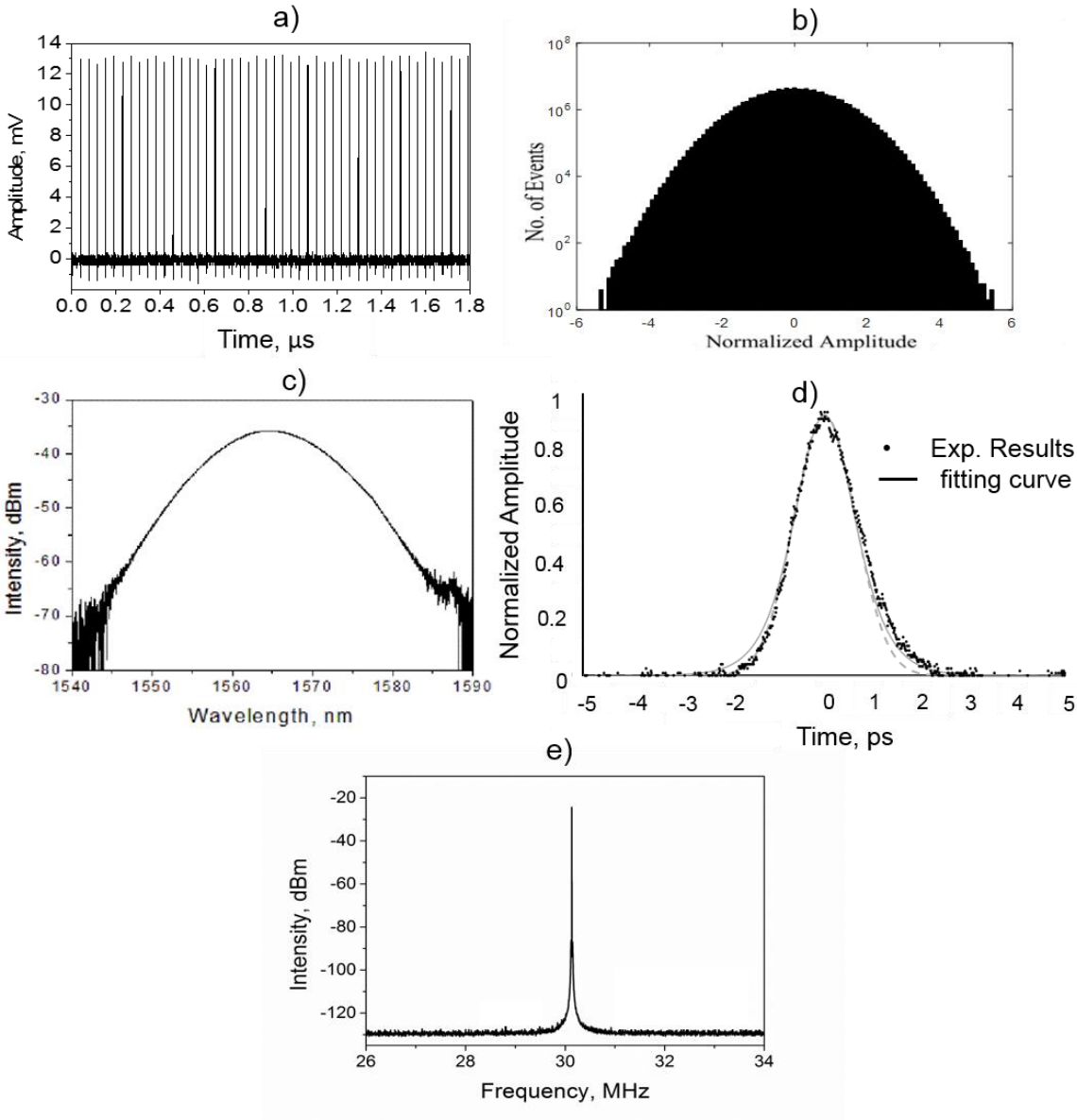

Fig. 4.3: The mode-locked regime laser regimes; (a) oscilloscope traces; (b) PDF histogram; (c) the optical spectrum (d) the autocorrelation measurement and (e) the RF spectrum of the mode-locked laser regime at a pump power of 19 mW (85 mA).

When operating in the normal mode-locked regime, the polarization attractor on the Poincaré sphere is shown in Fig. 4.4. Similar results were obtained over all of the normal mode-locked regime where the polarization state is in the form of a fixed point in the Poincaré sphere (Fig. 4.4 (a)) that indicates a stable output power (Fig. 4.4 (b)). The PDF histogram is shown in Fig. 4.4 (c) where we have calculated for the output power (I_x+I_y) and

this shows a normal Gaussian distribution as expected as the pump power is far below the optical RW threshold. The DOP that is close to 95% and has no big phase difference between two orthogonal polarization modes (Fig. 4.4 (d)) also confirms that the output laser regime is in stable operation.

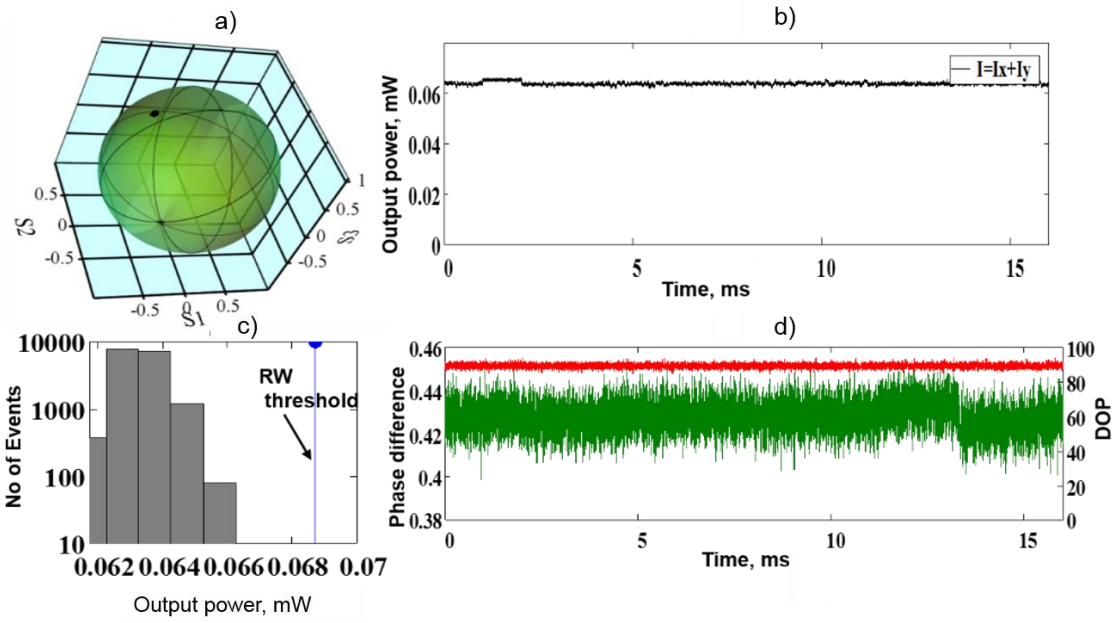

Fig. 4.4: (a) Stokes parameters at the Poincare´ sphere, (b) total optical power of orthogonally polarized modes I=Ix+Iy, (c) PDF histogram and (d) phase difference (green) and DOP (red) of the mode-locked laser regime at a pump power of 19 mW (85mA).

4.4: Optical Rogue Waves Driven by Modulation Instabilities.

When certain parameters of the laser cavity are set, the output laser steady-state regime became unstable against small fluctuations (MI) due to either polarization or pump power and leads to the development of a periodic modulation. MI could be either spontaneous or stimulated MI. This section focuses on optical RW generation as a result of spontaneous. The laser in Fig.4.1 was adjusted to operate in CW regime in the first group of the pump power which is only slightly above the laser threshold. This CW beam was found to be inherently unstable; the laser output can undergo spontaneous temporal modulation and transfer into a periodic pulse train. This periodic modulation dynamics are typically described in the spatiotemporal domain. Based on spatiotemporal evolution dynamics, different kinds of breathers were observed within the first pump power group (79-86 mA, 16.3-20mW).

4.4.1: Akhmediev Breather Optical Rogue Waves.

A breather soliton is a nonlinear wave in which energy is localized in space but oscillates in time or vice versa. It forms an important part of many different classes of nonlinear wave systems, manifesting themselves as a localized temporal structure that exhibits oscillatory

behaviour. To date, the dynamics of breather solitons in stretched-pulse (β~0) mode-locked fibre ring laser remains largely unexplored, and its experimental characterization is challenging. Here we demonstrate the first experimental excitation of AB near to β~0 cavity fibre laser. However, it was found that at a 16.3 mW, the instability causes a periodic perturbation on the CW background which grows exponentially along the propagation distance (RT) forming an Akhmediev breather (AB). Fig. 4.5 shows the temporal evolution of the AB at 16.3 mW (79 mA) of pump power. We can show from Fig. 4.5 (a) that the AB consists of a temporarily single pulse train that undergoes a single growth-decay cycle localized along the RT and appears eventually in periodic pulses through the RT. This growth describes the initial exponential growth of the weak perturbation in the framework of the MI. Therefore, the breakup of CW emission due to the MI condition was used to obtain the pulses train condition. The estimated breather period for this pump power is 3.7 ns. The periodic nature of this breather implies that the pulse should restore its original shape. Also, the PDF statistics in Fig. 4.5 (b) shows that the AB formed has an asymmetric shape and large statistical deviations from a normal Gaussian distribution with a long tail exceeding 8 σ from the mean value on both sides of the PDF; normalized amplitude >8σ is the bright RW threshold criteria, whereas normalized amplitude <-8σ is the dark RW threshold criteria). This can confirm that the laser is operating in a regime accompanied by the emission of bright and dark RWs. It was found that the bright RW probability is 3.2×10^{-3}, whereas the dark RW probability is 2.2×10^{-4}. The spectral evolution towards breather formation in both the RF and optical domains is plotted in Fig. 4.5 (c, d) respectively. It can be seen that the RF has a clearly MI in form of low RF noise that appeared close to the central frequency of the RF confirmed of the MI that leads to the formation of the AB and the abrupt output pulses. Also, the optical spectrum exhibit a heavy primary comb lines due to the MI.

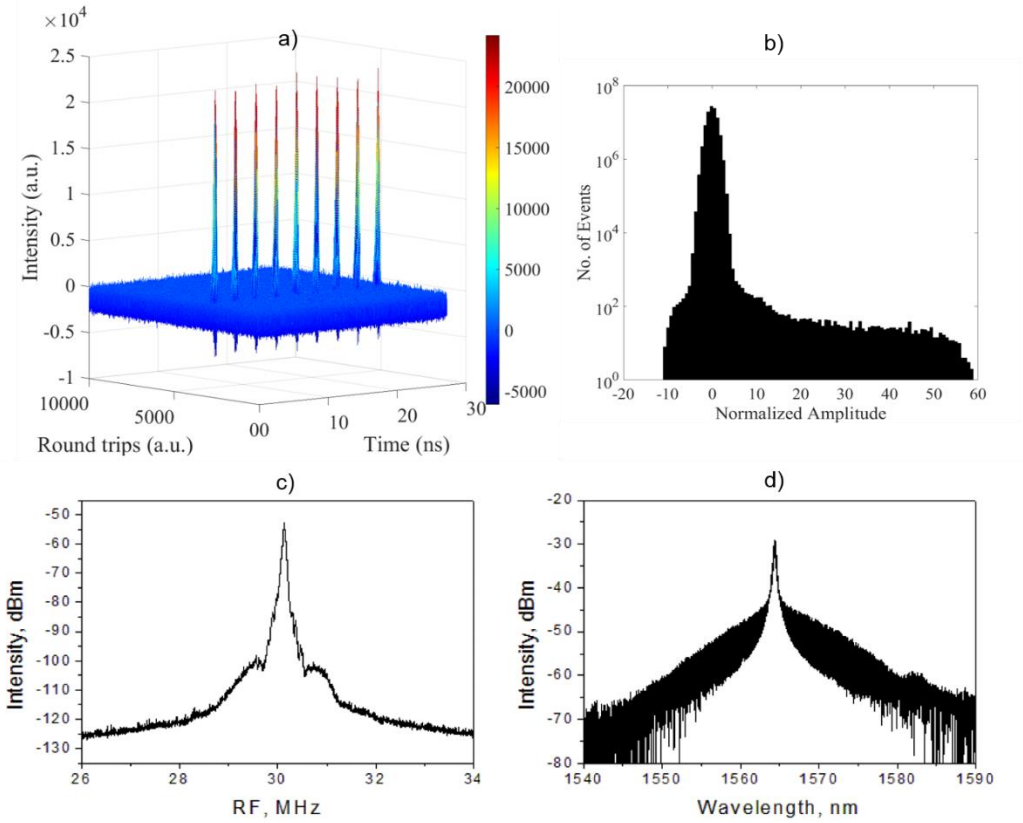

Fig. 4.5 a) AB temporal evolution; b) PDF histogram of the laser regime; c) the RF spectrum and d) the optical spectrum.

The RF beat note peaks (detuning) that are excited by MI are 163 KHz, 260 KHz, 346 KHz and 483 KHz are shown in Fig. 4.6 (a). The 163 KHz has a small intensity modulation depth (<2 dBm) that has less effect on the AB formation compared to the 260 KHz that has an about 5 dBm intensity which affected the AB periodicity formation. This RF beat peak (260 KHz) confirmed the breather periodicity (3.84 ns) in Fig. 4.5 (a) as AB repeated each 1000RT (breather frequency 260 KHz x1000RT=260 MHz); breather periodicity=1/260 MHz=3.84 ns). We attribute these sharp RF beat notes to the occurrence of AB breather pulses, while the other broad RF placed at about 30.83 MHz (detuning 700 KHz) indicated an unstable high order MI. As the AB is periodic in RT, the breather has grown exponentially during 200RT and decayed with 300RT with repetition of each 1000RT (Fig. 4.6 (b)). The optical spectrum (Fig. 4.5 (d)) is covered with primary comb lines with about 8 dBm intensity (Fig. 4.6 (c)) and this confirms the MI status without any sign of PI. Therefore, the evolution of the RF detuning and MI in the optical spectra is crucial for AB breather formation. The same breather exactly has been obtained at 17 and 18 mW. Apparently, this regime is linked to the evolution of a weakly MI signal with the AB.

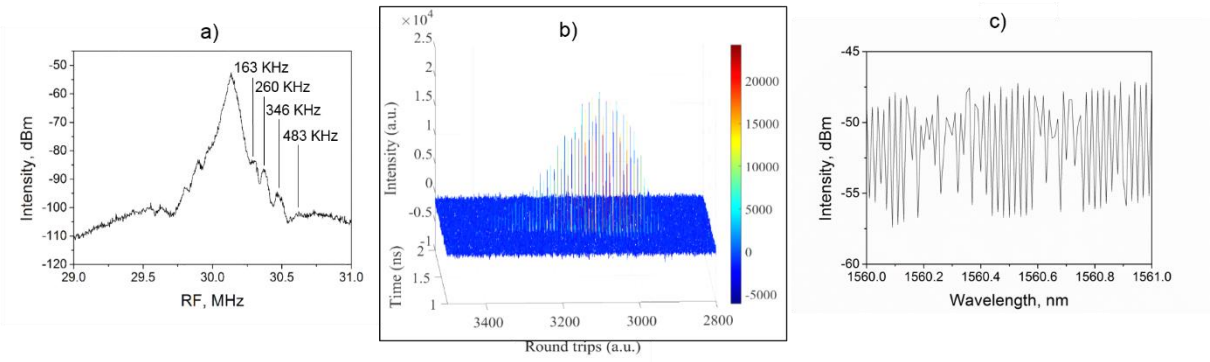

Fig: 4.6 a) RF spectrum over 2MHz; b) 3D breather intensity evolution over 1 ns and 600RT; c) the MI on the optical spectrum.

4.4.2: Peregrine Optical Rogue Waves

Increasing the MI perturbation by increasing the laser pump power to 18 mW (82mA), it was observed a single pulse with localization in time as well as in RT position as shown in Fig. 4.7 (a). This localized pulse is similar to Peregrine soliton (PS) that was experimentally observed earlier this decade [26] as it is not reportable in both time and RT. The intensity evolution is repeated noisy each 6.8 ns (Fig. 4.8 (a)) after formation of the PS within the first RT. The PDF statistics in Fig. 4.7 (b) is quite different from PDF of the AB case; it has asymmetric shape and large statistical deviations from normal Gaussian distribution with a long tail exceeding 8 σ from the mean value on right sides only, which means that the laser is operating in a regime accompanied by the emission of optical bright RWs only. The optical bright RW probability was found to be 3.67 $x10^{-4}$ which is significantly less than the AB RW. Actually, this regime links to the evolution of a weakly modulated CW signal with the MI inside the laser cavity as shown in both the RF and optical spectra in Figs. 4.7 (c, d).

Both the RF and optical spectra have a clear MI but it seems less than the previous case especially on the optical spectrum. The small RF beat note peaks are also excited by MI as in the AB in section 4.4.1. But, because of the increased perturbation, these peaks are shifted closer to the central frequency and placed at 140 KHz, 216 KHz, 313 KHz, and 460 KHz respectively. Compared to the AB RF spectrum, the intensity of the peaks have increased by about 8 dBm and become narrower with a very small modulation depth. The peregrine breather grows exponentially over a period of 330RT and decays over about 600RT as illustrated in Fig. 4.8 (b). As in the previous status, the optical spectrum have also coved with non-uniform primary comb lines (Fig. 4.8 (c)) which confirm the MI perturbation.

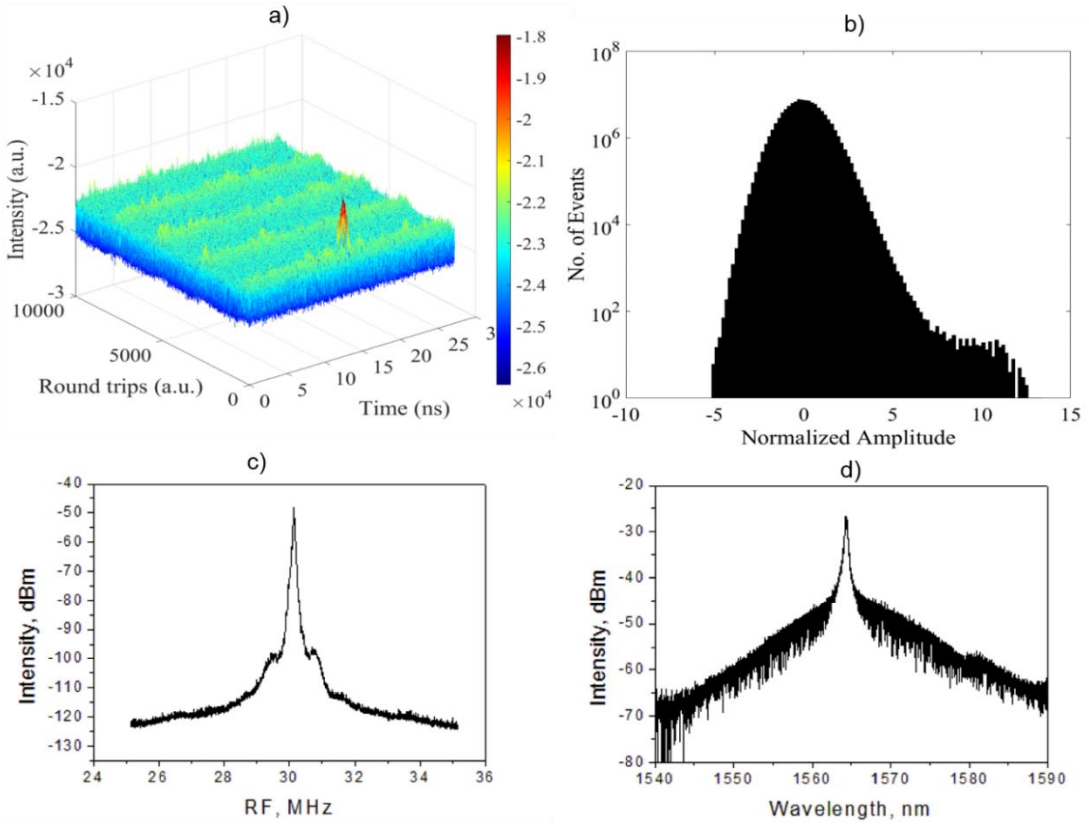

Fig. 4.7: (a) Peregrine soliton 3D temporal evolution; b) PDF histogram of the PS laser regime; c) the RF spectrum and d) the optical spectrum.

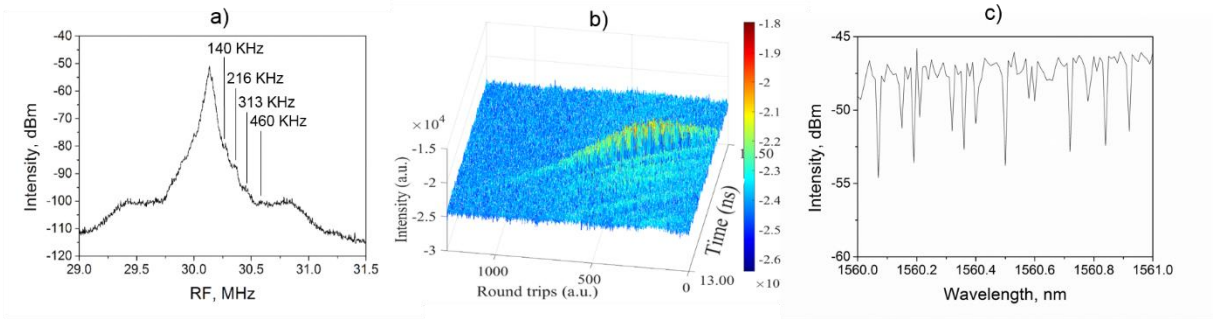

Fig. 4.8: a) RF spectrum over 2.5MHz; b) 3D PS breather intensity evolution over 1.5 ns and 1200RT; c) the MI over 1 nm of the optical spectrum.

4.4.3: Bi-Periodic (Twin) Breather Optical Rogue Waves.

Further increasing the pump power to 20 mW (86 mA, increasing the MI perturbation), the laser starts to emit twin pulses, which are also named bi-periodic pulses where the pulses can be periodically repeated in both RT (AB) and time Kuznetsov-Ma (KM), which form bi-periodic breathers as shown in Fig. 4.9 (a). Therefore, the dynamic of this regime is that the output is periodic along both RT (spatial) and temporal (time) axis. Fig. 4.9 (a) shows the pulse evolution in the average soliton regime over 6000RT. When increasing the modulated CW field due to increasing the pump power, the laser pulses inside the laser cavity became unstable due to the MI which leads to the growth of multiple periodic pulses as shown in Fig. 4.9 (a). It was found that this periodicity is a feature depending on both pump power

and PC1. Controlling both means controlling the modulation length and the periodicity of the MI. The estimated breather periodicity is 3.7 ns (as in the AB in section 4.4.1). Also, this periodic nature implies that the pulses should restore to their original shape when the period is a multiple of the RT period. Compared to AB in Fig. 4.5, the dark pulse intensity has decreased and only just surpasses the definition threshold for dark RWs (-8σ) with a probability of $4x10^{-6}$ ((Fig. 4.9 (b)), while a very clear long tail shape in the right side of the PDF confirms optical bright RW events with a high probability of $2.68x10^{-2}$. Increasing the pump power to 20 mW increases the modulation depth of the frequency and also the spectrum exhibits an additional wide sideband of the main peak which is related to slow and fast PI (Fig. 4.9 (c)). Therefore, the RF spectrum in Fig. 4.9 (c) exhibits two kinds of MI. The first MI is placed close to the central frequency and is related to the pump power MI as in all of the previous cases. Whereas the other two sideband spectra near to 22 MHz and 37 MHz are related to the PI. The intensity of the MI (~20 -50 dBm) is significantly higher than the intensity of the PI (15 dBm) which makes both of them contribute to the formation of this kind of breather. The optical spectrum in Fig. 4.9 (d) is the same as in the BA where the spectrum is clearly covered with primary comb lines related to the modulated instability. The pulses exhibit periodicity in both transverse time and longitudinal RT (Bi-periodic) and have been described by a Jacobi elliptic function. Indeed, when one of the periods tends to infinity, we obtain either AB or KM. But when both of them tend to infinity, we obtain the peregrine in the output pulse.

The RF beat note peaks seem to be in resonance with the central frequency and are equally spaced (28 KHz) as shown in Fig. 4.10 (a) which could be counted as the occurrence of the Bi-breather formation. From Fig. 4.10 (b), it was found that the first pulse from the beginning of the RT has grown over 170RT and decayed over 500RT, while the second pulse has grown and decayed with about 430RT and 420RT respectively. The distance between these two pulses is 1000RT. On the other side, the growth time of both pulses are about 30 ps and the decay time is about double this (60 ps). These pulses are repeated each 100RT confirming the frequency detuning of the polarization instability (PI) (2.8 MHz) and the breather periodicity (3.57 ns) ((breather frequency 2.8 MHz x100RT=280 MHz); breather periodicity=1/280 MHz=3.57 ns). The MI in the optical spectrum (Fig. 4.10 (c)) is slightly different from the MI of the optical Peregrine RWs case, it is just as more modulated as in AB optical spectrum in section 4.4.1.

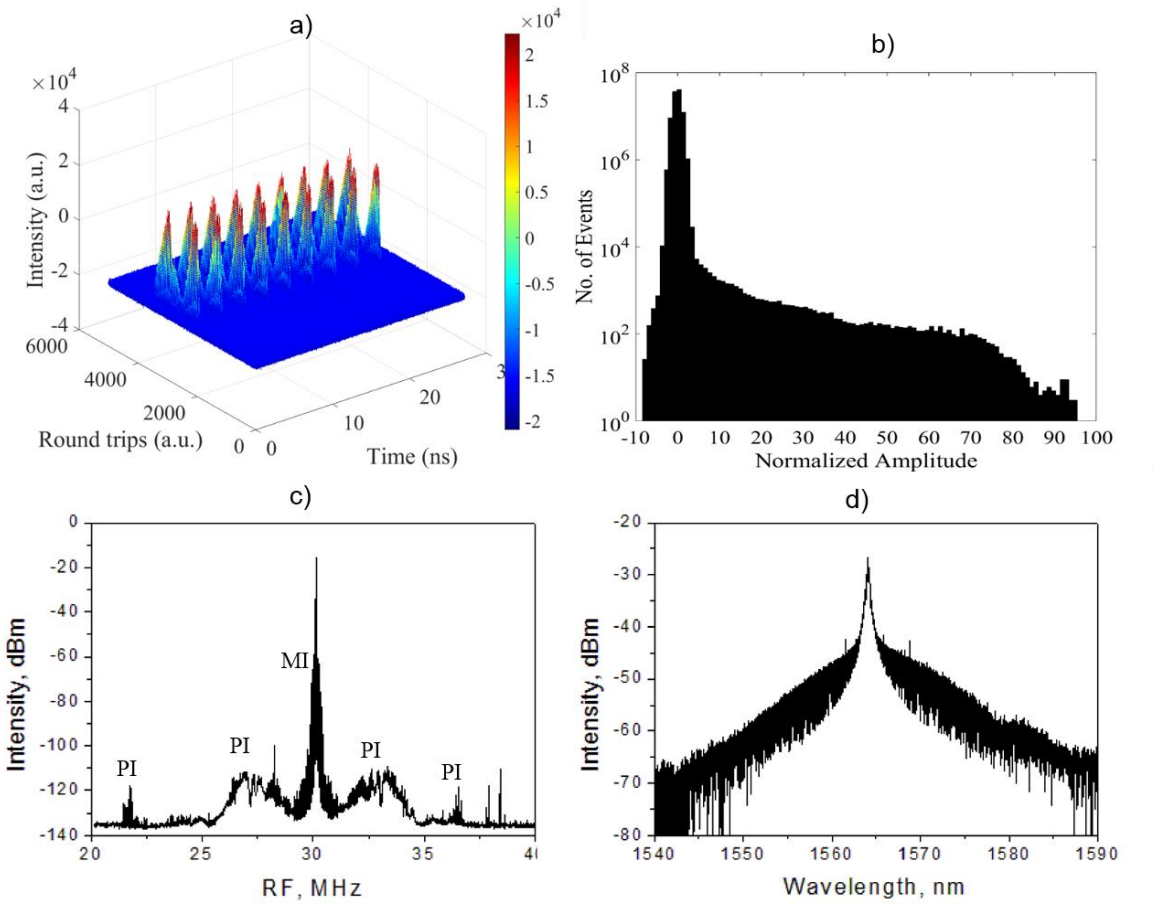

Fig. 4.9: (a) Bi-periodic temporal evolution at a pump power of 20mW; b) PDF of the laser regime; c) the RF spectrum and d) the optical spectrum.

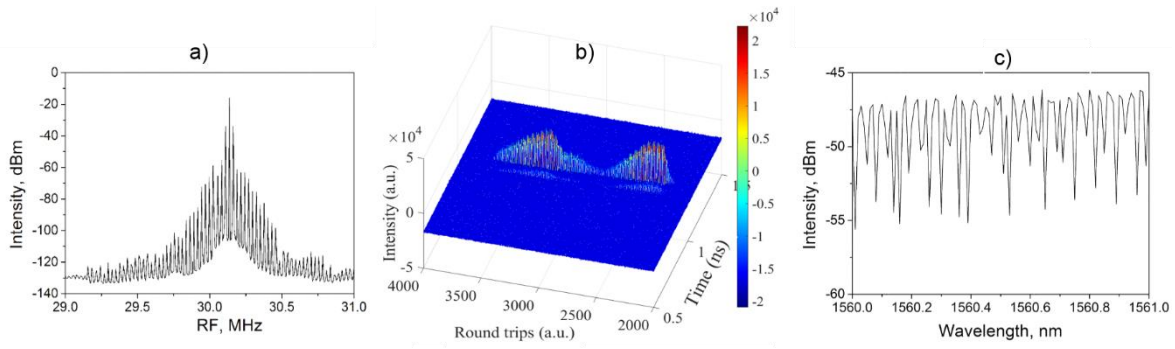

Fig. 4.10: a) RF spectrum over 2MHz; b) 3D breather intensity evolution over 1.5 ns and 2000RT; c) the MI over 1 nm of the optical spectrum.

It was observed that the RF spectrum in Fig. 4.9 (c) exhibited PI. Therefore, the output from the laser cavity can easily switch to chaotic bi-periodic (Fig. 4.11(a)) through tuning the PC1at the same pump power (20 mW). Therefore, the breathers formed at this pump power are not periodic in nature and the pulse can't revert to its original shape. The growth of the perturbation from both MI and PI produces large waves and increases the population of optical RWs. This contribution of both MI and PI can be described by a random combination

of the laser parameters such as the pump power and the SOP and leads to the formation of a non-uniform higher order of breather.

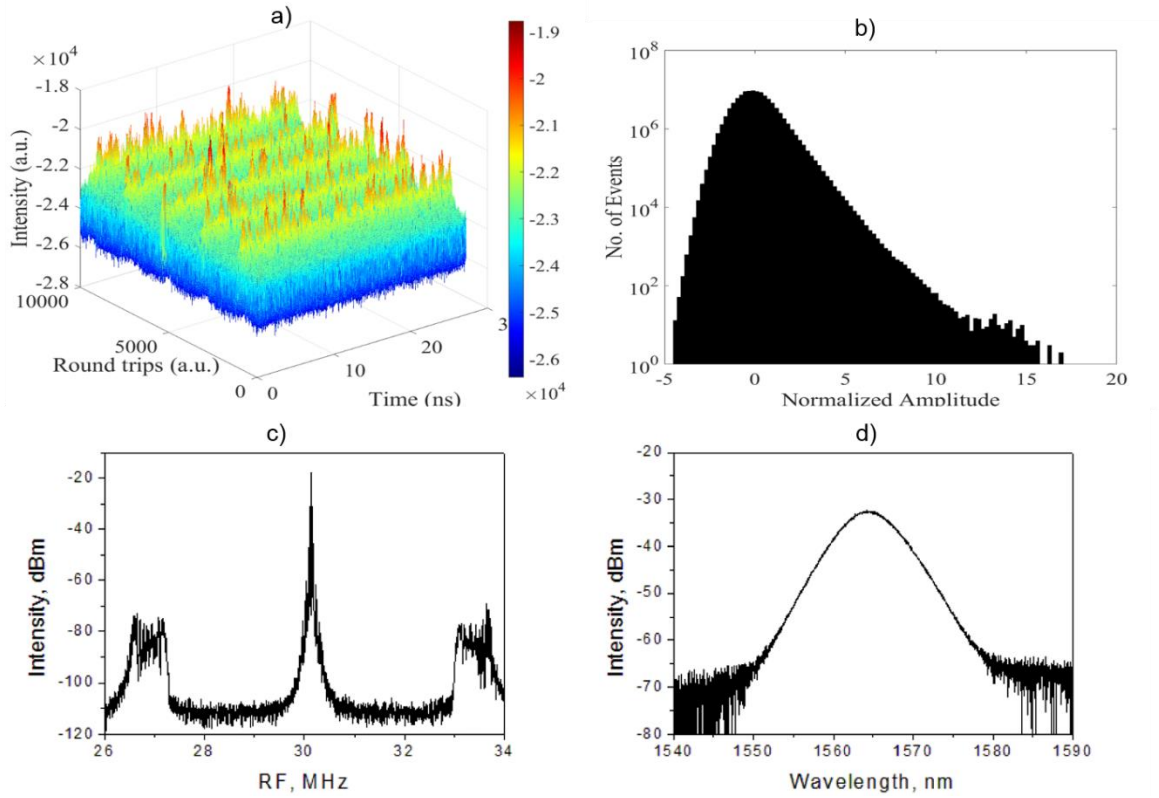

Fig. 4.11 (a) Chaotic Bi-periodic temporal evolution; b) PDF of the laser regime; c) the RF spectrum and d) the optical spectrum.

The PDF in Fig. 4.11(b) confirms the generation of bright optical RWs for this pump power with a probability of about 2.2×10^{-3} while optical dark RW has not surpassed the DRW threshold. Also, controlling these sidebands requires controlling the SOP inside the laser cavity and this can also increase the probability of optical RW appearing. In addition to the equally spaced RF beat detuning (28 KHz) shown in the RF spectrum in Fig. 4.11(c) exhibited 4 MHz PI satellites with an intensity of around 35 dBm because of the longitudinal modes beating inside the laser cavity. At this pump power, the PI led to a significant enhancement of the weak instabilities when both PC1 and PC2 were turned. The PI is quite wide (1 MHz) and modulated with noisy MI components which made the output breathers non-periodic. These pulses suffer from a high fluctuation and surpass the optical bright RW criteria. Also, we found here the controlling of PC1 had an impact on the optical RW probability, and for this situation, the PDF probability was about 9.46×10^{-3}. The optical spectrum illustarted in Fig. 4.11(d) shows a stretched pulse spectrum centred at 1565 nm with very small fluctuation within the peaks confirming that increasing the MI leads to the fundamental soliton regime, but this appears chaotically (Fig. 4.11(a)) due to the unstable polarization instability dynamics.

All of the previous breathers and RW events show that the PI either did not contribute to the pulse formation (as in AB and PS cases) or is too small, unstable and non-uniform (as in both of the Bi-periodic results). Actually, the nature of the MI depends strongly on the whether the pump power is below or above the PI power threshold. It was found that the threshold power is required to excite the stable PI in our stretched fibre laser is 21.6 mW.

4.5: Breathers Polarization Dynamics.

To get an insight into the PI and the mechanism of BDRW emergence at slow time scales of 1 μs – 20 ms (660K round trips), we have studied the evolution of the polarization dynamics. A set of 16 slices of the temporal waveforms have been saved and combined with the help of the polarimeter. This was used to measure the DOP and normalized Stokes parameters S_1, S_2, and S_3 which are related to the output powers of two linearly cross-polarised SOPs as given in equation 2.1. It was found that the polarization evolution in Fig. 4.12 (a, b) for both AB and PS show that the SOP is moving chaotically in the Poincaré sphere. This approach shows that the motion of the Stocks parameters on the Poincaré sphere becomes chaotic in the sense that polarization for both AB and PS does not return to its original state after each successive period. The spikes in the total output power (represented by I_x+I_y) which appear as semi-periodically modulated along the slow time scale correspond to spikes in both the phase difference and DOP (Fig. 4.12 (g, h)) that confirm the random transition between the two orthogonal polarized light as can be seen in the Poincare sphere. The phase difference and DOP switch between low and high power periodically due to periodic perturbation yielding a long tail PDF histogram that surpasses the RW threshold (Fig. 4.12 (i)) for AB due to random phase difference and nearly to the RW threshold (Fig. 4.12 (k)) for PS due to oscillating phase difference (between 0 and π). Therefore, the modulation periodicity of PS is less (higher modulation frequency) due to increasing the perturbation through increasing the pump power which makes the chaotic movement of the Stokes parameters less random. The polarization evolution of the Bi-periodic breather Fig. 4.12 (c) is quite different from the polarization evolution of both AB and PS. The SOP is in the form of an arc moving periodically between the two orthogonal polarizations can be seen in the Poincaré sphere. This is due to the effect of PI that leads to switching the polarization of light inside the laser cavity between the low and high power states of the two orthogonal polarizations. The combination of both MI and PI lead to a regularly modulated output power (Fig, 4.12 (f)), regular oscillations in the phase difference between 0 and π as well as fast DOP switching (10%-90%) between the two orthogonal polarizations indicating the effects of the PI on the output polarization dynamics. The PDF histogram of the Bi-periodic breather is quite far from the RW threshold in slow time scale due to the regular phase difference between 0 and π.

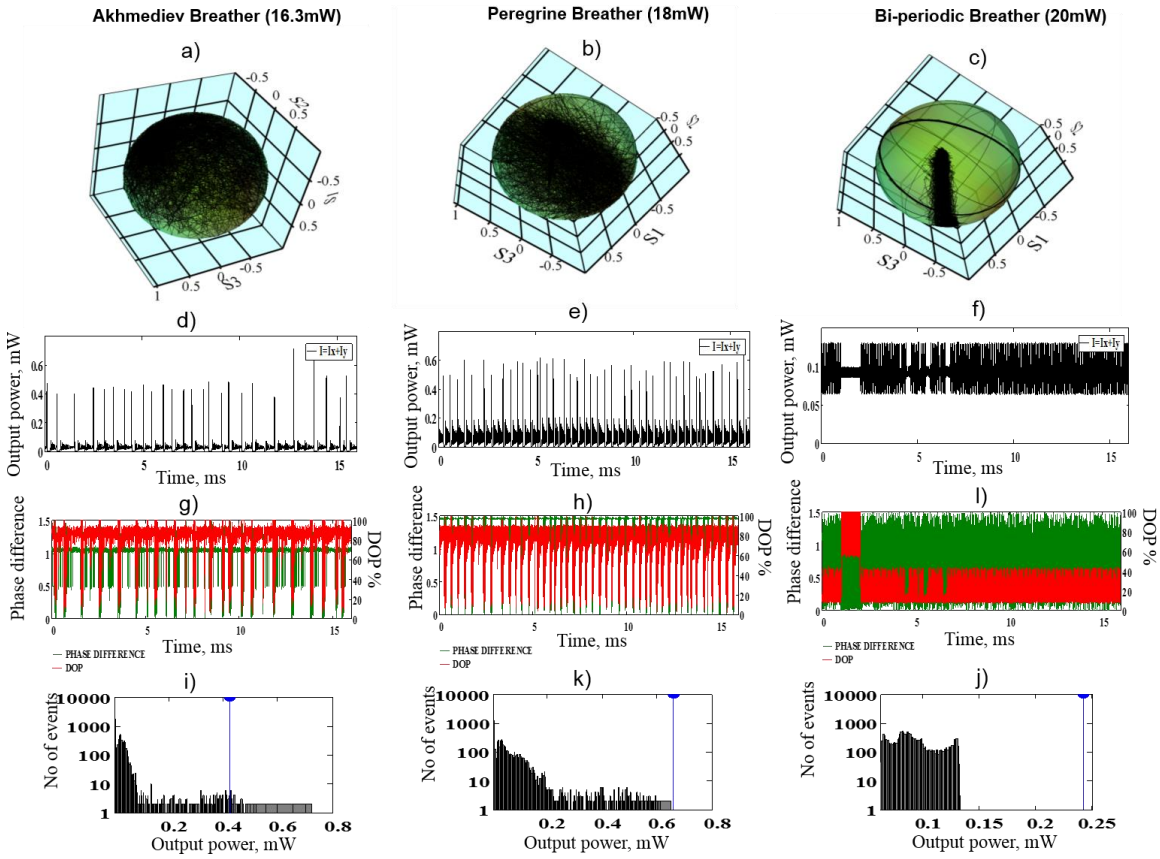

Fig. 4.12: (a, b, c) Stokes parameters at the Poincare´ sphere, (d, e, f) total optical power of $I=I_x+I_y$, (g, h, I) phase difference and degree of polarization and (I, k, j) PDF histogram of the observed breather in this experiment.

4.6: Polarization Instability Bright-Dark Rogue Wave Events

The polarization instability in the previous section elucidates that the intra-cavity polarization can generate large changes in the output pulse formation when the input power or the polarization controllers PC1 and PC2 are changed slightly. The presence of this polarization instability also shows that slow and fast axis can not be entirely equal in position and amplitude. The effect of this as a source of PI can be understood as follows. When the input beam is polarized close to the slow axis (*x*-axis at $n_x > n_y$), nonlinear birefringence adds to intrinsic linear birefringence, making the fibre more birefringent. In contrast, when the input beam is polarized close to the fast axis, nonlinear effects decrease total birefringence by an amount that depends on the input power. As a result, the fibre becomes less birefringent. But the fibre again becomes birefringent with a further increase of the input power. Moreover, the shape of the output pulses is found to change dramatically when the pump power exceeds a certain value that we have called the critical power for exciting polarization instability. In our fibre laser, this critical power is found to be 21.8 mW (88 mA). Therefore, large changes in the output of the laser can occur when the input power is close to or higher than the polarization instability threshold as it will be a balance of the linear and nonlinear birefringence.

However, in addition to the laser regimes that are observed within the first pump power group, a different set of laser regimes can be triggered within the second pump power group by adjusting polarization in the laser cavity (by adjusting PC1 in Fig. 4.1). Therefore, tuning the laser cavity birefringence induces modulation in form of PI inside the laser cavity that is then further amplified by the EDF gain fibre section in the cavity. Subsequently, a rich set of pulse dynamic regimes, including bright optical RW, can also be observed.

The BDRW events which result from PI were observed at the second pump power group which are in the range of (88-98 mA; 21.8-28 mW); increasing the power to slightly above the first pump power group excites the MI (79-86 mA). To confirm the emergence of BDRWs, time series of oscilloscope traces were recorded, as was described in section 4.2, when the laser is an operating at an 88 mA, 20 mW pump power. This was used to measure the shot-to-shot intensity variations.

Furthermore, to gain an understanding the mechanisms that govern the emergence of BDRWs, we performed real-time measurements of the spatiotemporal intensity and polarization dynamics evolution. The 3D spatiotemporal intensity dynamics measurements, which are shown in Fig. 4.13 (a) reveal only one soliton pulse propagating inside the laser cavity and clearly there is no sign of pulse-pulse interaction during the saved data shown in Fig. 4.14 (a) (oscilloscope trace for 1.2ms). Thus we can rule out both breather formation and pulse to pulse interaction as a mechanism for the formation of BDRWs at this pump power. The most notable characteristic of the RW events is a highly skewed PDF of the output power. In Fig. 4.13 (b), the observed PDF statistical analysis shows the strongly asymmetric shape and large statistical deviations from the Gaussian distribution with a long tail exceeding 8 σ from the mean value on both sides of the PDF. From Fig 4.13 (b), it was confirmed that the laser is operating in a regime accompanied by the emission of bright RWs (with a probability of 6.8×10^{-2}) and dark RWs (with a probability of 8.4×10^{-4}). Also, further analysis of these 3D patterns shows that the RW emerged as a result of PI that leads to the interaction of the two orthogonal polarizations and this can be clearly seen on both of the RF and optical spectra (Fig. 4.13 (c, d)). The specific SOP induces the initial intensity perturbations exactly like the input MI which break the stability of the two orthogonal vector polarization in the laser cavity. Therefore, the PI indeed affects the fundamental soliton and makes it unstable and this leads to the emergence of the BDRW.

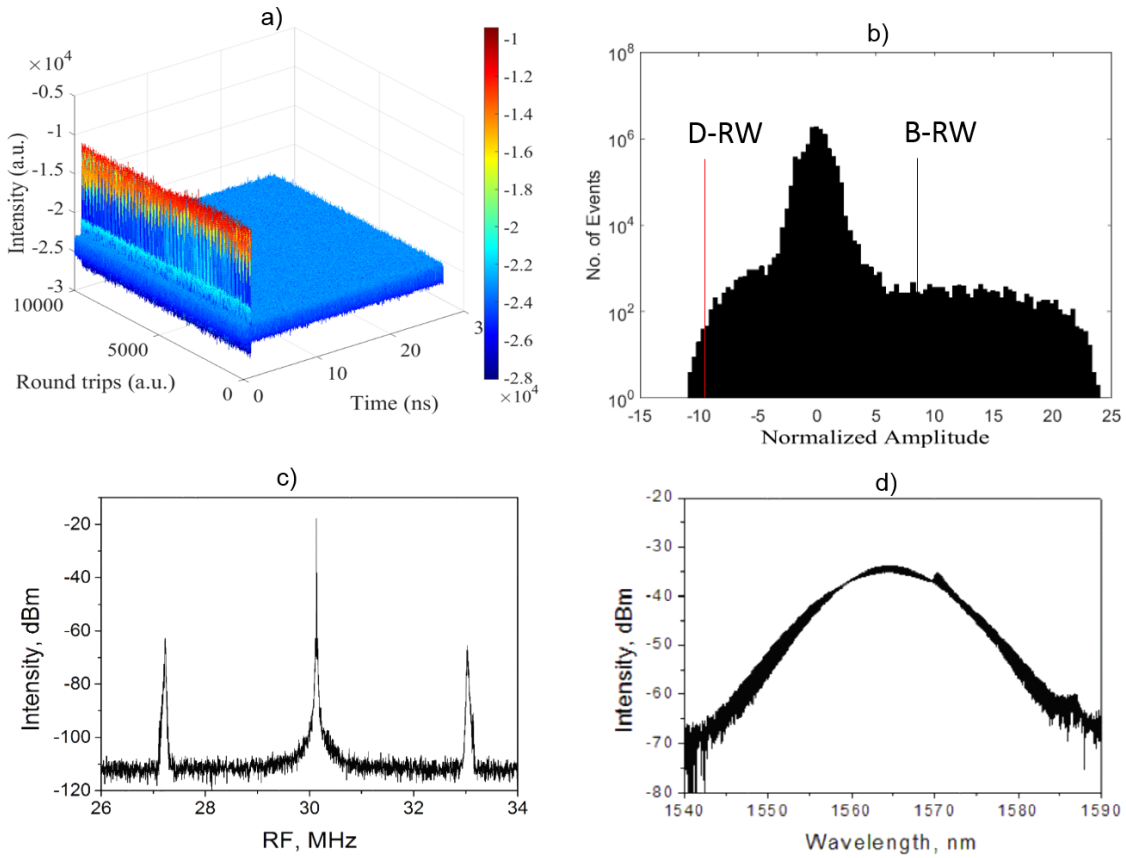

Fig. 4.13: Optical BDRW pattern at a pump power of 21.8 mW; (a) 3D spatiotemporal intensity dynamics of the BDRW for one round trip over 10000 round trips; (b) PDF histogram (vertical lines are the RW threshold); (c) RF spectrum; and (d) the optical spectrum.

The RF spectrum of this regime shown in Fig. 4.13 (c) exhibits a very clear PI modulation (satellites) that are related to the slow and fast orthogonal polarizations and are placed at a detuning of 3 MHz and low-noise RF spectrum with 20 KHz detuning peaks (Fig. 4.14 (c)). The polarization satellites here are dominated as PI because of the intensity of these satellites (45 dBm) is higher than the intensity of the MI (3 dBm) and these satellites can be tuned by just tuning the PC1 in the laser cavity. The optical spectrum for the bright-dark regime is illustrated in Figure 4.13 (d); it was centred at about 1565 nm and had a width of 8 nm. The modulation on the spectrum is a result of polarization modulation instabilities. This modulation instability leads to clear fluctuations in the peaks of the output soliton pulses. The optical spectrum corresponds to the PI regime in which multiple independent mini-combs grow with a modulation space of 0.04 nm and a modulation depth varying between below 1 dBm to 4 dBm.

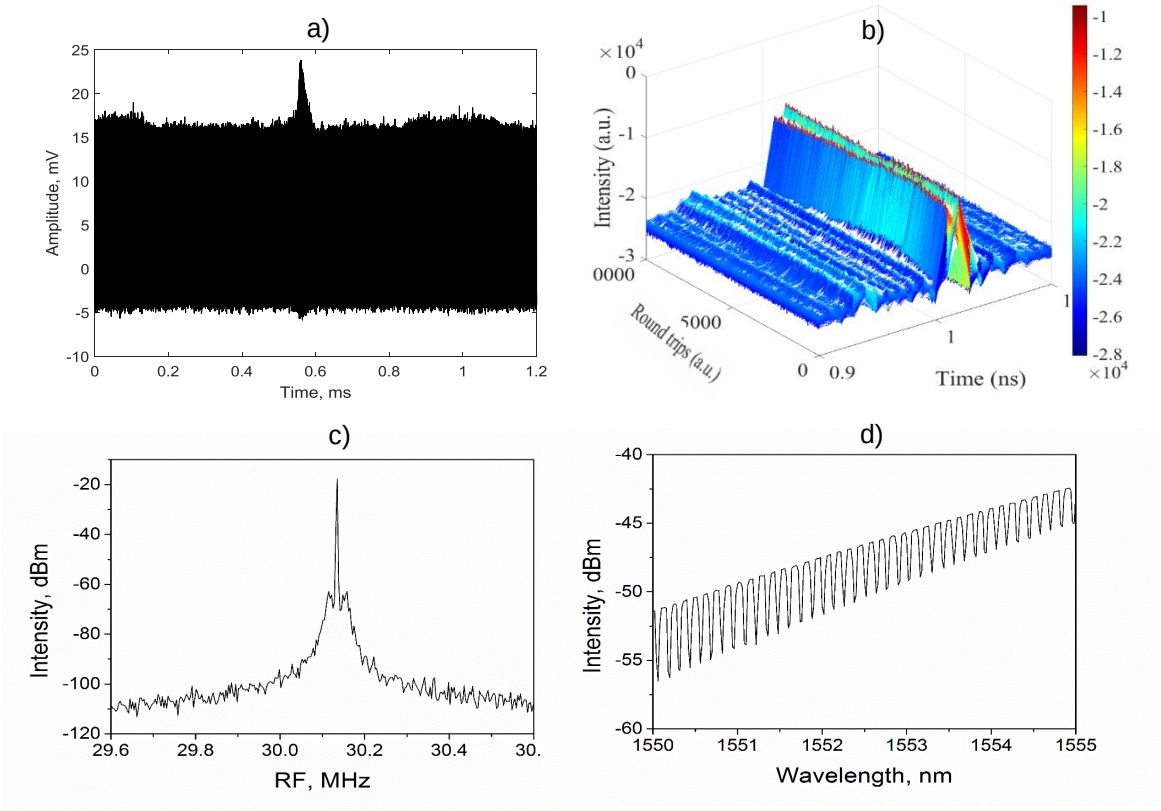

Fig. 4.14: (a) oscilloscope traces (33 GHz bandwidth) of 1.2 ms (b); getting inside the 3D spatiotemporal intensity dynamics 0.2 ns over 10000 RT (c) RF spectrum over 1 MHz showing the MI peaks (d) the mini-comb PI feature over 5nm of the optical spectrum.

As in section 4.4.3 on the bi-periodic breather, we found that the intra-cavity SOP can also switch the laser regime while maintaining the same pump power. For instance, at a pump power of 24.3 mW (92 mA), changing the SOP could switch the output laser regime from stable mode-locked (similar to the regime in section 4.2) to the other laser regimes, such as unstable fundamental and harmonic mode-locked regime. We observed that the output laser regime is switched dramatically from long-term mode-locked (after 0.9 ms of the 1.2 ms oscilloscope trace in Fig. 4.15 (a)) to chaotic pulse emission that clearly indicates optical RW emergence. Apparently, it is difficult to clarify this regime as a high Bi-periodic breather (AB and Ma) as the breather is formed from the breakup of the CW light into a train of pulses. But in our case, it seems the mode-locked regime is breaking up into chaotic pulses. In addition, increasing MI to a high value leads to a stabilization of the output soliton pulses [33]. Fig. 4.15 (a) shows the oscilloscope traces for 1.2 ms laser regime, while Fig. 4.15 (b) shows PDF statistics accompanied with this regime which clearly shows that the pattern has both optical bright and dark RW. Optical bright RW probability is quite high in this case (about 8.36×10^{-2}) while the optical dark RW probability is about 1×10^{-4}. The RF spectrum in Fig. 4.15 (c) shows clearly narrow and stable slow and fast polarization instabilities located about 3.5 MHz far from the central frequency with about 50 dBm modulation intensity depth. Also, the spectrum shows small non-uniform satellites placed in between the polarization

satellite and the central frequency which could indicate high order PI with the absence of evidence for MI. Based on these facts, the BDRW events have emerged at this pump power as the result of first and high order PI.

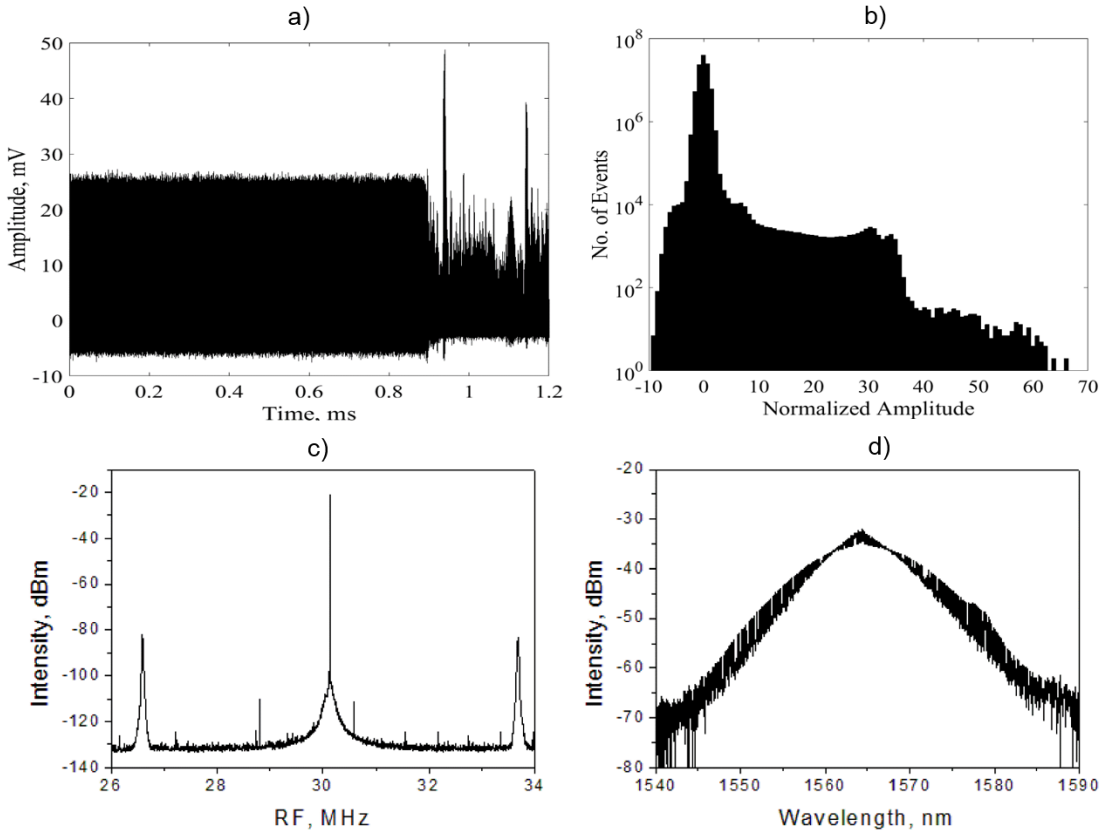

Fig. 4.15: Optical BDRW pattern at a pump power of 24.3 mW; (a) oscilloscope traces of 1.2 ms; (b) PDF histogram (vertical lines are the RW threshold); (c) RF spectrum and (d) the optical spectrum of this patterns.

Therefore, PI leads to the breakup of the mode-locked regimes to random intensity pulses which are responsible for both the bright and dark RW event formation. The optical spectrum in Fig. 4.15 (d) presents the modulation on the spectrum as a result of the polarization modulation instabilities. The spectrum parameters are quite similar to the previous case (21.8mW) as the output pulse was centred at 1565 nm and had a width of 8 nm. Also, the PI induced modulation space is 0.12 nm and modulation depth varying between below 1 dBm to 7.5 dBm in the optical spectrum (Fig. 4.16 (d)); the non-periodic mini-comb in this optical spectrum is due to the high order PI.

The 3D shape of this soliton laser regime in Fig. 4.16 (a) shows the pulse evolution over 1000RT which is a small part of the oscilloscope traces (0.34 ms). The output of this regime is a periodic temporal and spatial pulses train in the form of harmonic soliton pulses with a 3.7 ns soliton separation. The time interval between two neighbouring solitons or pulses is important to determine how close two solitons can come without affecting each other. Therefore, the front view of this figure confirmed that there is no sign of the soliton

interaction. But getting inside both RT (200RT) and time (4 ns) as in Fig. 4.16 (b) shows that the same soliton pulse in each round trip is unstable and has fluctuation in the output intensity. It seems that the periodic evolution is resulting from the interplay between both pump power and the intra-cavity SOP, but the long stable soliton pulses indeed are destroyed because of the relatively long-loss of the induced perturbation due to the high order PI.

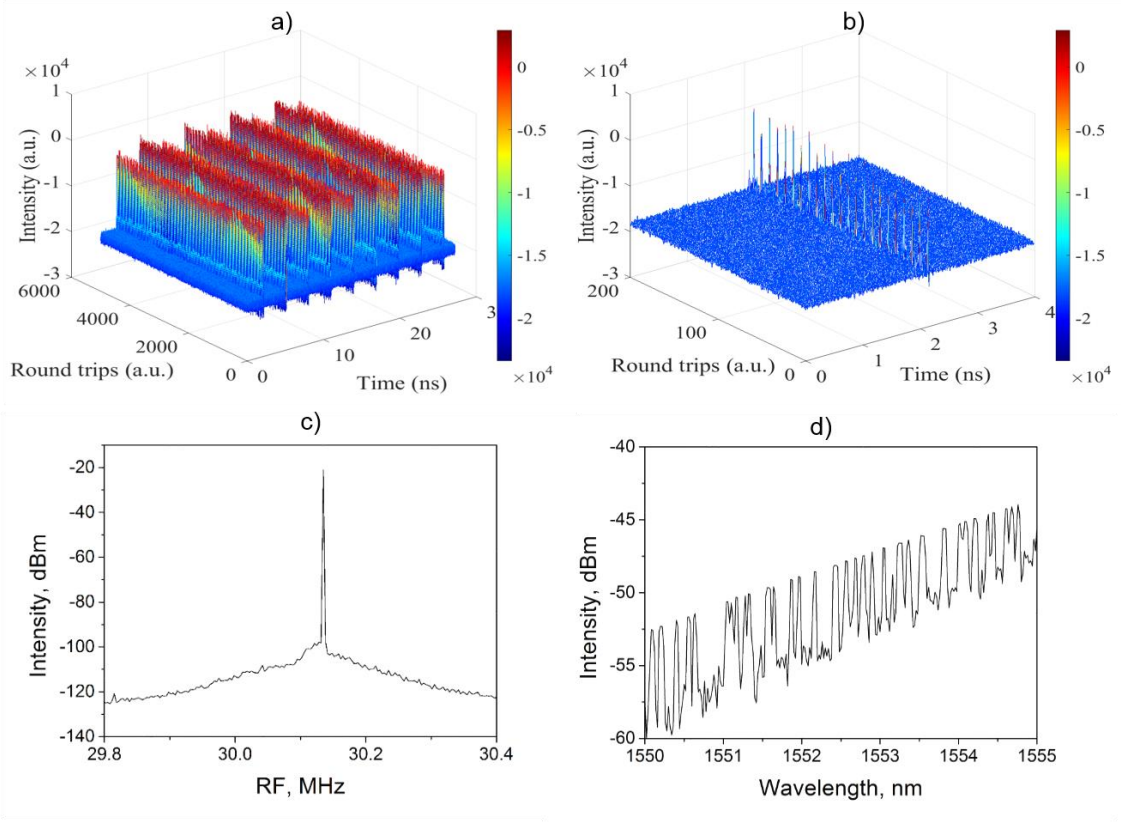

Fig. 4.16: (a) 3D spatiotemporal intensity dynamics of the BDRW for one round trip over 10000 round trips (0.34 ms) (b) getting inside the soliton pulse evolution over 200 RT and 4 ns showing the unstable output intensity evolution; (c) getting inside the RF showing the absence of the MI; and (d) random periodic of the mini-comb PI feature over 5 nm of the optical spectrum.

At the same pump power, 24.3 mW (92 mA), but after rotating the PC1 to another position, we observed a laser regime which is the exact opposite to the previous regime where the SOP can switch the output laser from a chaotic regime to a stable mode-locked regime. The output laser pulses which are shown in the oscilloscope trace in Fig. 4.17 (a) are switched from chaotic propagation in the laser cavity to a stable mode-locked laser regime. Therefore, the output regime is very sensitive to the SOP inside the laser cavity. Hence, the SOP plays an important role in the determining the output laser regime. The PDF statistics are shown in Fig. 4.17 (b) also confirm the BDRW accompanying this regime. The optical bright RW probability is quite high in this case (about $7x10^{-2}$) while the optical dark RW probability is about 10^{-6}. The RF spectrum in Fig. 4.17 (c) clearly shows two slow satellites and two fast satellites PI on each side of the central frequency and located at offsets of

about 7 MHz and 5 MHz and with non-uniform modulation intensity depth between 30 dBm and 5 dBm respectively. This gives an indication of presence of the high order PI, but with non-uniform intensities in both sides of the central frequency. Therefore, this confirmed the BDRW events have emerged in this pump power as the result of the high order PI. There is no clear difference in the optical spectrum of this laser regime compared to the previous regime.

The 3D shape of this soliton laser regime elucidate the pulse evolution over 0.34 ms is shown in Fig. 4.18 (a). The output in this regime starts chaotically for about 10000RT and then switches to stable mode-locked soliton pulses for the rest of the oscilloscope trace (1.2 ms).The time interval between two neighbouring harmonic soliton pulses is decreased to about 3.1 ns. The front view of the output evolution during 600RT and 10 ns (Fig. 4.18 (b)) confirmed that there is no any sign of soliton interaction.

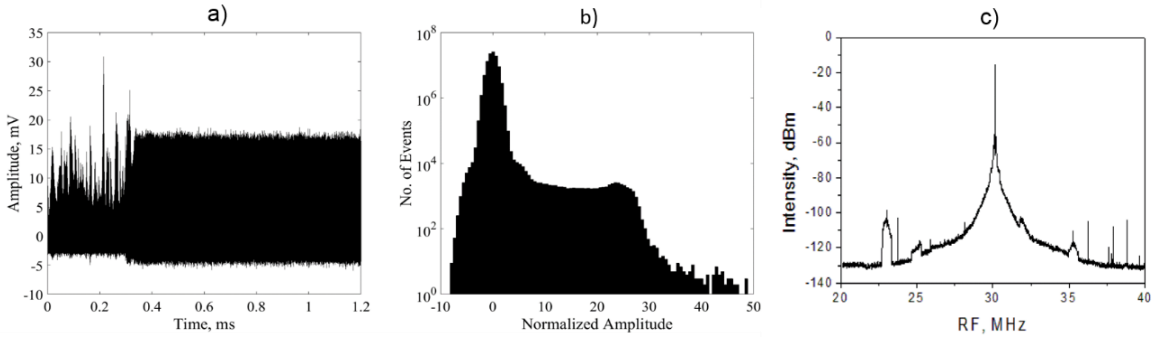

Fig. 4.17: Optical BDRW pattern at a pump power of 24.3 mW; (a) oscilloscope traces of 1.2 ms; (b) PDF histogram (vertical lines are the RW threshold) and (c) RF spectrum.

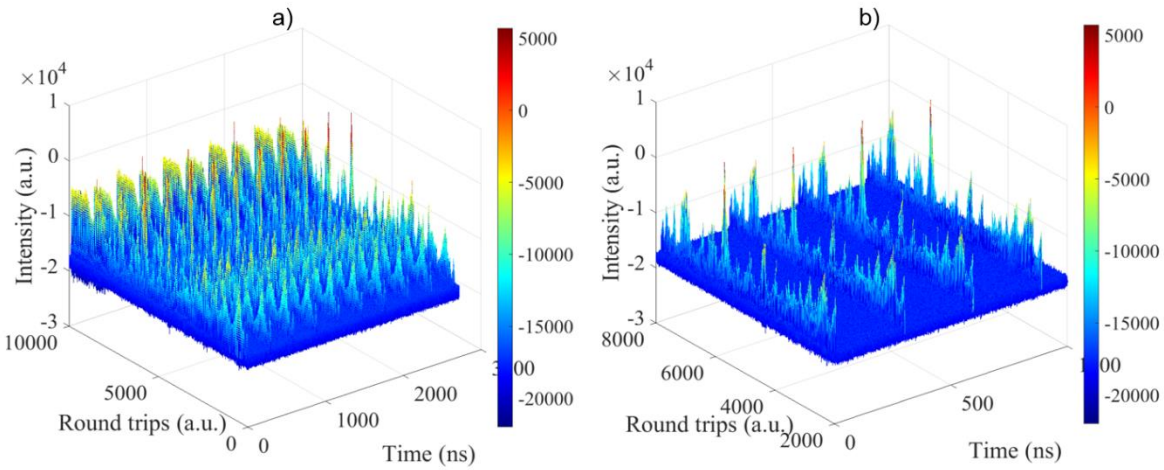

Fig. 4.18: (a) Spatiotemporal intensity dynamics of the BDRW for one round trip over 10000 RT and (b) soliton pulse evolution over 200 RT and 4ns of 24.3mW pump power.

Further investigation of the PI effect on the stabilization and the output mode-locked laser regimes have been made by increasing the pump power to 26.1 mW (95 mA). Interestingly, in this regime we find periodical switching between mode-locking patterns and BDRW patterns (Fig. 4.19 (a)). The oscilloscope trace and 3D shape in Fig. 4.19 (a) and Fig. 4.20

(a) respectively show that the laser operates in a single (fundamental) soliton pulse within the cavity round trip. The dip after each ML regimes and before each RW regime indicates that the system first accumulates energy during the dip to then emit high amplitude bright and dark RWs. This means that polarization instability drives the switch of the output laser regime from in-phase (coherent coupling) of the mode-locked regime to the out of phase (incoherent coupling) of the BDRW regime due to the fast switching between the two orthogonal polarizations. The 3D spatiotemporal pulse evolution (Fig. 4.20 (a)) over 1000 RT which is a small part of the oscilloscope traces (0.34 ms) shows semi-periodic (~0.16 ms) fast switching from the mode-locked regime to high amplitude pulses that grow exponentially and surpass the optical bright RWs criteria accompanied with dark pulses that also surpass the dark RW criteria (RW thresholds are defined as 8σ and -8σ respectively as shown in the PDF histogram in Fig. 4-19 (b). It also confirmed there is no sign of pulse-pulse interaction when BDRWs are generated. Getting inside the 3D (Fig. 4.20 (b)) shows that the RW emerged as a result of the PI that leads to interaction of the two orthogonal polarization inside the laser cavity.

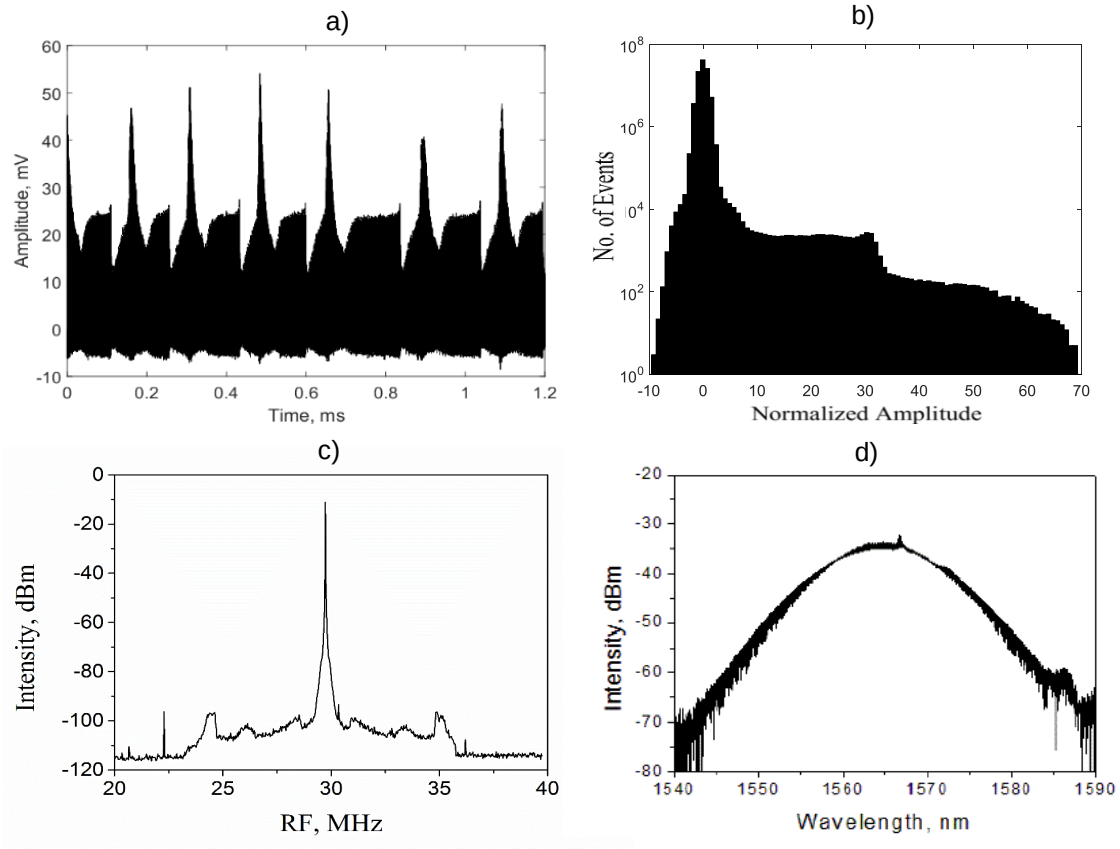

Fig. 4.19: Bright-Dark optical RW pattern at the pump power of 27 mW (95 mA); (a) Oscilloscope trace for 1.2 ms; (b) PDF histogram; (c) RF spectrum and (d) the optical spectrum.

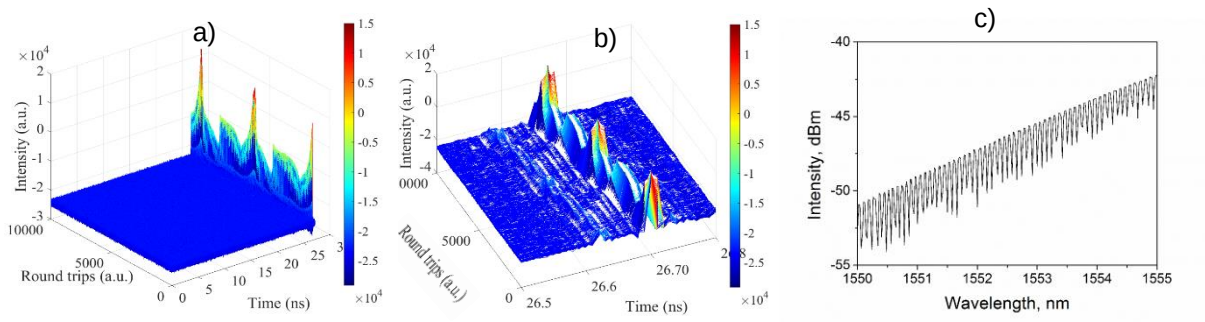

Fig. 4.20: (a) 3D front view of the pulse evolution for one RT over 10000 RT; (b) getting inside the 3D spatiotemporal (c) getting inside the optical spectrum showing the periodic mini-comb PI feature over 5nm.

The PDF histogram of this pattern also confirms BDRW and reveals a larger deviation from 8σ for the optical bright RWs while the dark RWs are smaller than in the previous pattern (20mW, 88mA). Optical bright RW probability is quite high in this case (about 7.67×10^{-2}) while the dark RW probability is about 2.1×10^{-5}. The RF and optical spectra (Fig. 4.19 (c, d)) illustrate that PI is the main source for emergence of BDRW. As the RF spectrum evolves the high orders of PI are placed uniformly at 0.5 MHz, 3 MHz and 5 MHz on each side of the peak and all have nearly the same modulation depth. Also, the RF spectrum shows no MI accompanied the PI at this regime. The optical spectrum in Fig. 4.20 (c) shows the modulation space is 0.08 nm and modulation depth variation between below 1 dBm to 2.5 dBm as a results of the PI that led to emerging the BDRW.

Further increasing the pump power to 28 mW (96 mA) (Fig. 4.21), we observed that the PI is the main source for the emergence of the BDRW, with previous patterns to those seen at a pump power of 26.1 mW (95 mA). From the oscilloscope measurements in Fig. 4.21 (a) and the 3D view in Fig. 4.22 (a), the system has also accumulated energy and this is released by gradually increasing the amplitude of the mode-locked regimes over a long period of exponential growth (0.6 ms) and then emit a high amplitude patterns that surpass the RW criteria of the PDF histogram. The PDF histogram, RF spectrum and optical spectrum are illustrated in Figs. 4.21(b-d) respectively, and follow similar patterns to the previous optical BDRW patterns at 21.8 mW (88 mA) and 26.1 mW (95 mA) pump powers. The PDF shows that the bright RW probability is very high (about 0.101), while dark RW probability is about 1.25×10^{-4}. The RF spectrum confirms the high order PI as we have many small peaks on both sides of the spectrum. While the optical spectrum also exhibits the mini comb features as a result of the PI with non-uniform periodic modulation space and modulation depth variation between below 1 dBm to 4 dBm as illustrated in Fig. 4.22 (c).

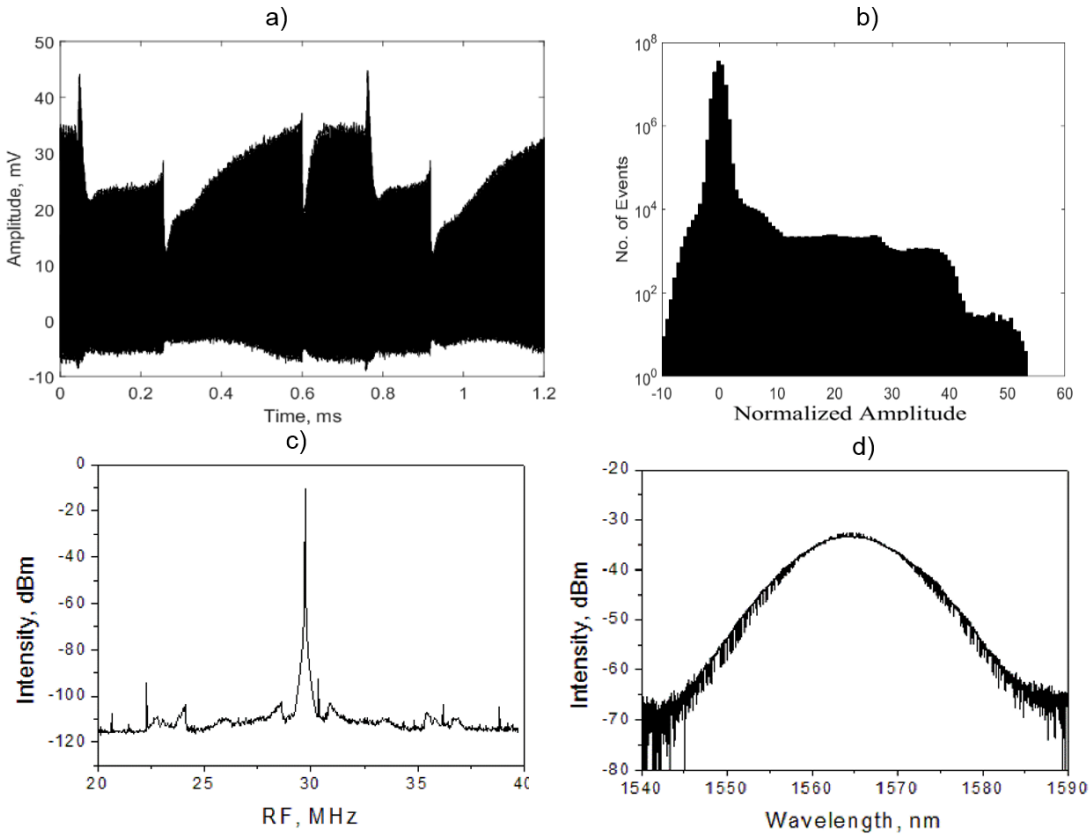

Fig. 4.21: Optical BDRW pattern at the pump power of 28mW; (a) Oscilloscope trace for 1.2 ms; (b) PDF histogram; (c) RF spectrum and (d) the optical spectrum.

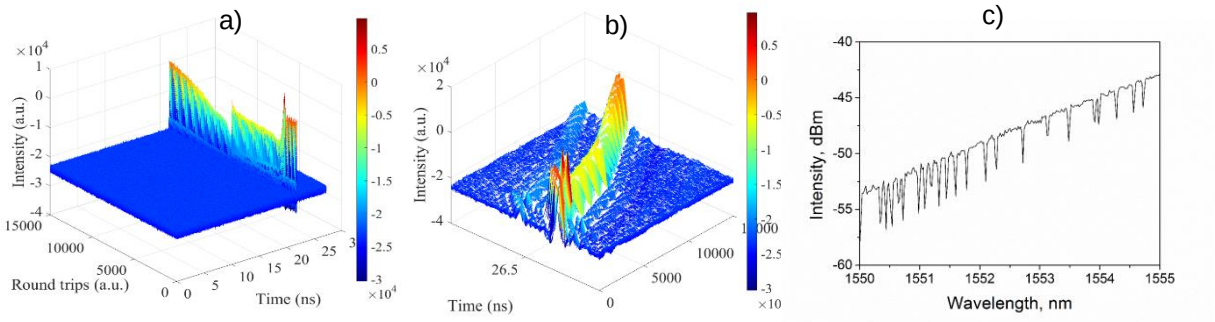

Fig. 4.22: (a) 3D side view of the spatiotemporal intensity dynamics for one RT over 10000 RT; (b) getting inside the 3D spatiotemporal and (c) getting inside the optical spectrum showing the mini-comb PI feature over 5 nm.

During this range of the pump power, increasing the pump power to about (29 mW, 100 mA), only optical bright RW have also observed which also emerged as results of high order PI; while the dark RW events have decreased to nearly the threshold limit or below. The oscilloscope trace, 3D spatiotemporal intensity evolution PDF histogram, RF spectrum and optical spectrum of this optical bright RWs pattern are illustrated in Fig. 4-23 (a-d) respectively. The oscilloscope trace (Fig. 4.23 (a)) shows very clear bright RWs which also is confirmed by the L-shaped PDF (Fig. 4.23 (b)) which have very clear bright RWs with high probability (7.46×10^{-2}, while dark RWs get zero probability which as it below the limit of the -8σ indicating that there was no dark RW accompanied by the bright RW events. The

3D spatiotemporal intensity dynamics (Fig. 4.23 (c)) also confirmed there was no sign of pulse-pulse interactions as there is only one single pulse inside the laser cavity and this pattern as a result of spontaneous synchronization of two orthogonal polarization components due to the polarization instabilities. The RF spectrum (Fig.4.23 (d)) confirmed the high PI. The optical spectrum analyzer is not greatly different from the previous scenarios but just accompanied with fewer modulation features.

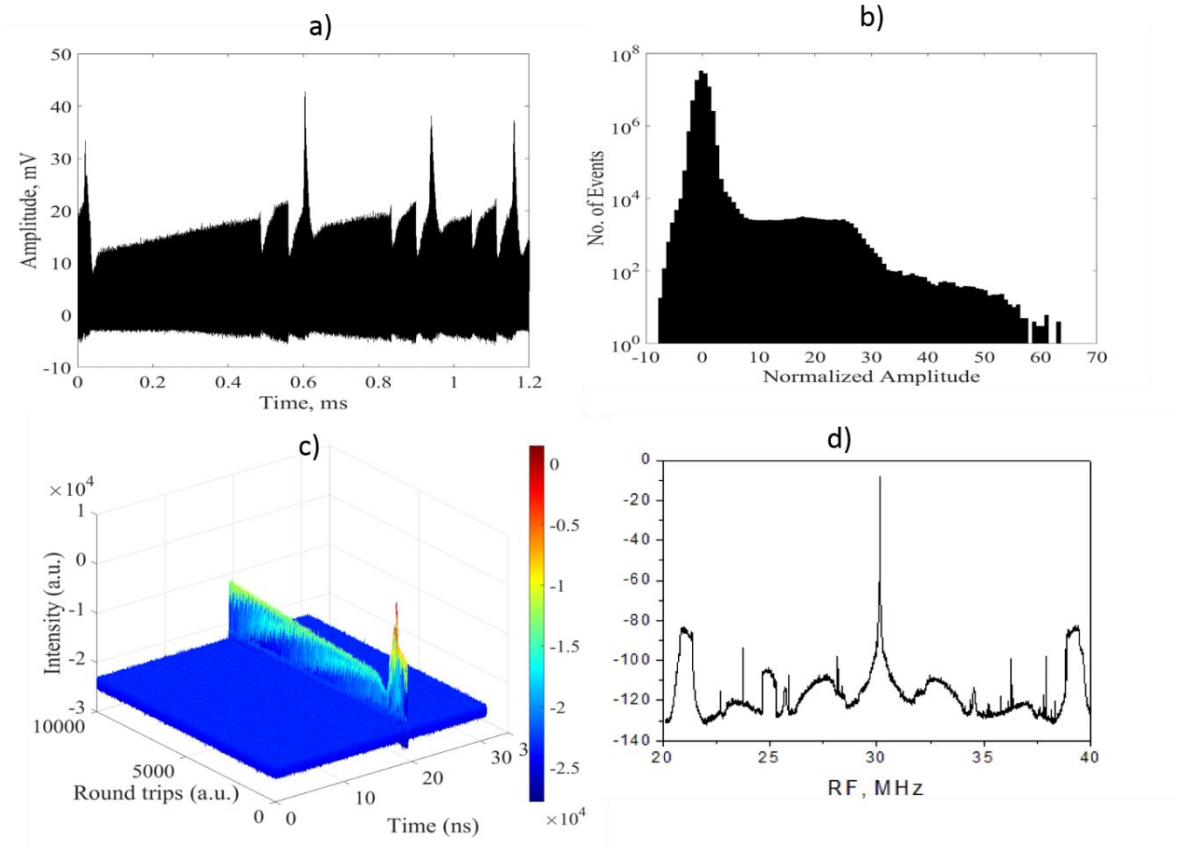

Fig. 4.23: Bright optical RW pattern at the pump power of 32 mW, 100 mA; (a) oscilloscope traces over 1.2 ms; (b) PDF histogram; (b) the RF spectrum and (d) the optical spectrum.

Further increasing the pump power to the third range of the pump power group, which is beyond 103 mA (31 mW), the laser system started to work in multiple pulses, pulse bound states and also harmonic mode-locked regime. In these regimes, the polarization instability frequency is less than 2MHz from the central frequency. These regimes of emission have been intensively investigated in fibre lasers with anomalous and normal net cavity dispersion. However, switching between the different regimes needs adjustment of the PC1 settings and pump power.

It is worth noting that all observed optical BDRW events have lifetimes in the 10s of µs (as shown in the oscilloscope traces (Fig. 4.14 (a), 4.15 (a), 4.18 (a), 4.19 (a), 4.21 (a), 4.23 (a)) (30-60 µs)). In other words, their lifetime is 10^3 times longer than the laser cavity round trip time (~34 ns). Thus, we can categorize these events as belonging to the family of slowly evolving RWs.

4.7: Polarization dynamic of the Optical Bright-Dark Rogue Waves.

Using the slow time scale, the observed RW patterns that emerged due to the PI have been characterized using the same polarimeter to detect the Stokes parameters S_1, S_2, S_3, the phase difference and the DOP. The intensities of the two linearly-polarized I_x and I_y were measured from equation 2.1. The S_1, S_2, S_3 at Poincaré sphere for the observed optical BDRWs at different pump power (88 mA-98 mA; 21.6-28 mW) are shown in Fig. 4.24. It was found that the evolution of the measured state of polarizations (Fig. 4.24 (a-c)) for all of the patterns are switched between the orthogonal polarizations in the form of arc attractor. But in Fig. 4.24 (c), the polarization attractor is in the form of a double semicircle. This double semicircle is sensitive to fluctuation of the fibre birefringence in form of PI. The anomalous spikes in the output power (I_x+I_y) at the slow time scale Figs. 4.24 (d-f) correspond to the spikes in DOP and phase difference jump in π, i.e. transitions between orthogonally polarised SOPs as shown in Fig. 4.24 (g, l). It coincides with jumps in DOP and phase difference jumps in π, i.e. transitions between orthogonally polarised SOPs. The evolution of the DOP and the phase difference show a switching between 20% and 95% in the DOP confirming the fast polarization switching between the two orthogonal polarization modes; low signal power and high signal power. Also, the low phase difference in Figs. 4.24 (g-l) elucidates the partial coupling between the two orthogonal polarization components as in the mode-locked regimes, while the high phase difference indicates for incoherent (random) coupling between the polarization components that lead to the emergence of the optical BDRW events. This leads to an asymmetrical PDF histogram for the orthogonal SOPs total power $I=I_x+I_y$ showing the presence of the optical dark and bright RWs (Fig. 4.24 (k-j)) as the spikes in the output total power coincides with jumps in DOP and phase difference. Unlike this, only bright RW are present in Fig. 4-24 (i). Therefore, the interaction between the two orthogonal SOPs is due to the anti-phase dynamics of the output power represented by I_x and I_y, DOP and phase difference that led to the BDRW.

The same scenario was repeated for the polarization dynamics evolution of the optical bright RW that was observed at 30 mW.

The BDRW results that emerged due to the PI have been confirmed theoretically by Sergey [126]. Theoretical analysis demonstrates that orthogonally polarised SOPs can be considered as quasi-equilibrium points where a typical trajectory traverses the neighbourhood of one of the orthogonal SOPs with further switching to the other SOP. The dwell time for the trajectory in the vicinity of each orthogonal of the SOP is defined by the cavity anisotropy, i.e. by the pump wave's ellipticity which is adjustable using the pump polarisation controller. The escape from the neighbourhood of each SOPs is driven by the cavity birefringence tuneable with the help of the in-cavity polarisation controller and leads to the output power distribution satisfying the BDRWs criteria.

Therefore, as in the theoretical model [126], the orthogonally polarised SOPs can be considered as coupled oscillators where the frequency difference depends on the birefringent strength and the coupling strength and is a function of the ellipticity and the power of the pump wave. Thus, adjustment of the pump wave and in-cavity polarisation controllers (PC1 and PC2 in Fig.3-1), the pump power results in tuning the frequency difference and the coupling strength. This provides the complex dynamics tunability from the phase difference oscillations to chaotic phase jumps resulting in BDRWs emergence.

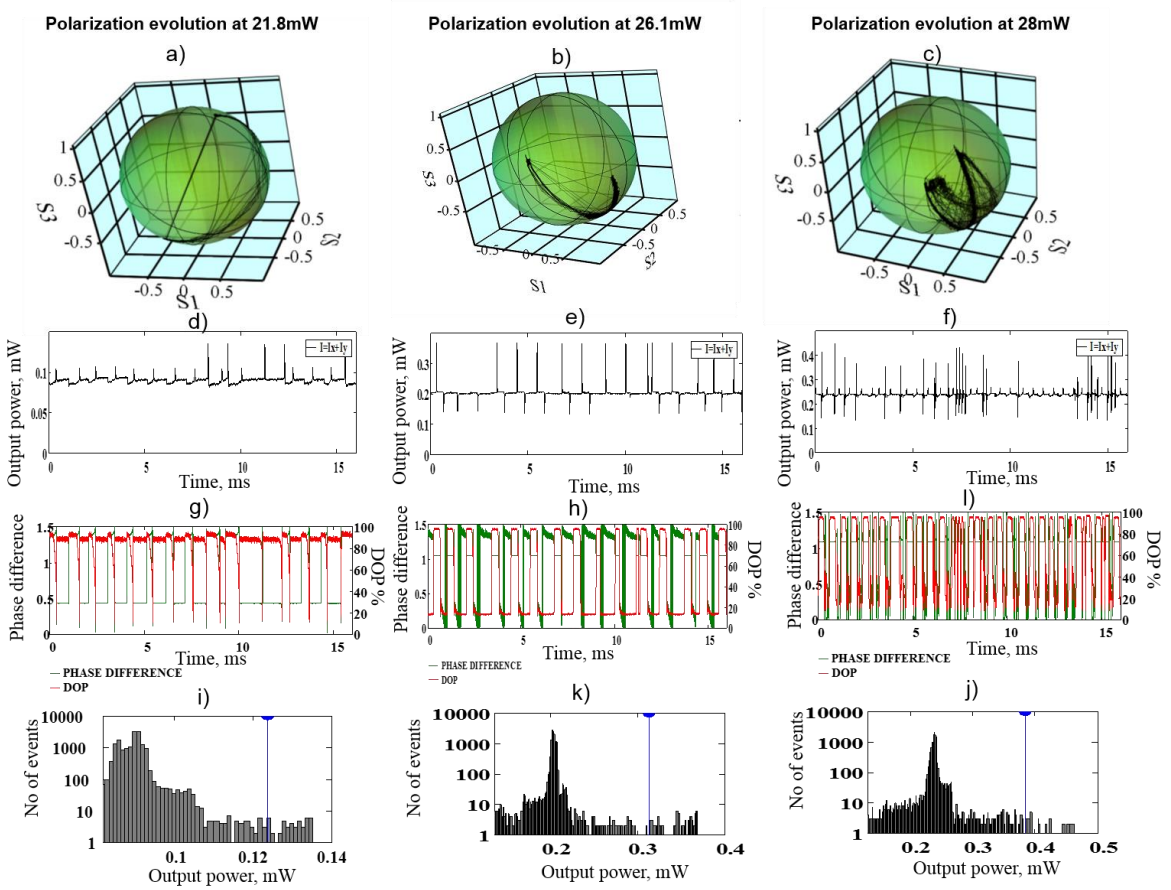

Fig. 4.24: Polarization dynamics measurements of the bright-dark RW(1 μs resolution, i.e. averaging over approximately 30 round trips, 16 slices with 1024 points per slice): (a–c) Stokes parameters at the Poincare´ sphere, (d–f) optical total power $I=I_x+I_y$ of orthogonally polarized modes, (g–l) phase difference (green) and degree of polarization (red) and (j-i) PDF histogram. Parameters pump power: 88 mA, 20 mW; 95 mA; 27 mW; and 96 mA, 30 mW respectively.

Through the above systematic experimental approach, our observations have confirmed the existence of optical BDRW events which had previously only been predicted theoretically. The PDF of all BDRW regimes have large statistical deviations from the Gaussian distribution with L-shaped on both sides of the PDF. The 3D spatiotemporal intensity dynamics analysis shows there was no sign of pulse-pulse interaction in all of the observed optical BDRW regimes and the events have emerged due to the PI as was confirmed by both the RF and optical spectra. The measurement of the polarization dynamics confirm the transfer of energy between the two orthogonal polarization states,

confirming polarization switching. The difference in the output laser regimes depends on the birefringence strength (controlled by PC1) and the coupling strength (controlled by pump power) of the two orthogonal SOPs inside the laser cavity. Therefore, the PI can be attributed as a mechanism of vector BDRW events that emerge as the result of the interaction of an incoherent coupling between the two orthogonal linear polarization components in the laser cavity. This mechanism of interaction between the two orthogonal polarization wave components generally allows energy transfer between additional degrees of the freedom; this potentially led to form this kind of vector optical RW.

4.8: Conclusions.

In addition to the pulse-pulse and soliton dissipative wave interactions mechanisms of RW emergence, we have demonstrated a new mechanism that is caused by the coherent coupling between the orthogonal SOPs. This resulted in the emergence of a new type of vector optical BDRWs (anomalous spikes-dips) that appear as a result of PI. This work is first experimental evidence of vector BDRWs that had been recently predicted by several independent theoretical studies [9-12]. We have showed that the extreme positive bright and dark optical intensity events result from MI that leads to the breaks up the CW radiation into a train of pulses. These are in forms of breathers when the pump power is within the first group which is below the polarization instability threshold power. When the pump power exceeds the power that required to excite the polarization instability (second group), the output laser pulses are also accompanied with BDRW due to the interaction of the desynchronized two orthogonal polarization by PI. The experimental results showed that BDRW breather events have formed within the first pump power group due to the MI while BDRW events in the second pump power group are formed due to PI, which causes the interaction of incoherent coupling of the two orthogonal linear polarization components that drives the laser cavity, leading to the emergence vector BDRW events.

The results can pave the way to the unlocking of the universal nature of the origin RWs and so can be of interest to a broad scientific community.

Finally, we have summarised the observed BDRW patterns in the stretched mode cavity fibre laser experiment in the flowchart as illustrated in chart 4.1. Furthermore, we can transfer our experimental results and the mechanisms to the triangle interrelation (Fig. 4.25) that is explained by N. Akhmediev et al [127] between various solutions of the NLSE. Also, we conclude with a table showing for each of these types of event, the RW pattern lifetime, its likelihood and the formation mechanisms (table 4.1).

Chart 4.1: Flowchart of all BDRW events observed in our experiment of the stretched mode-locked fibre laser.

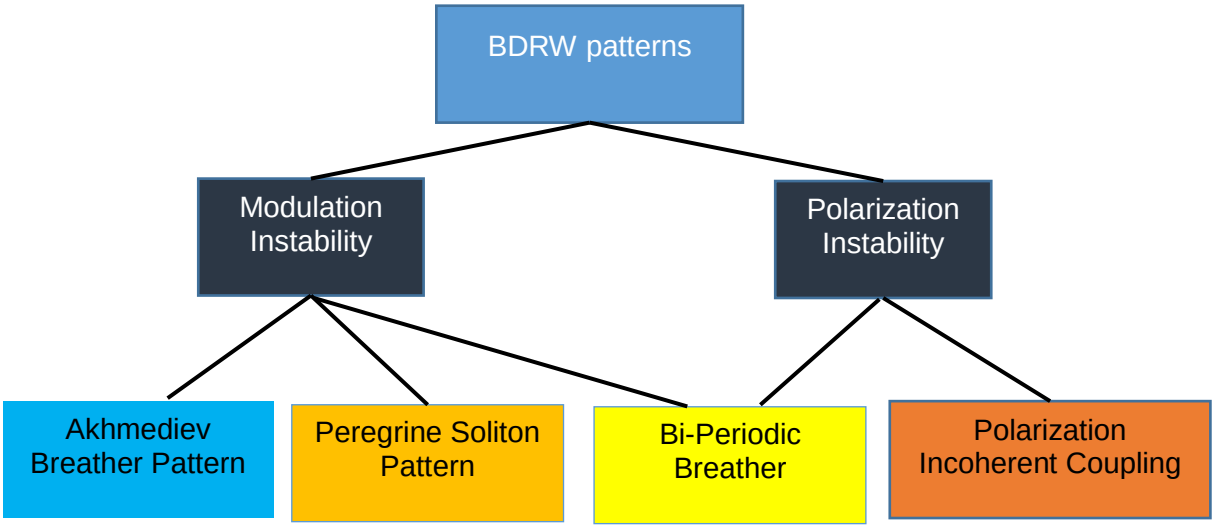

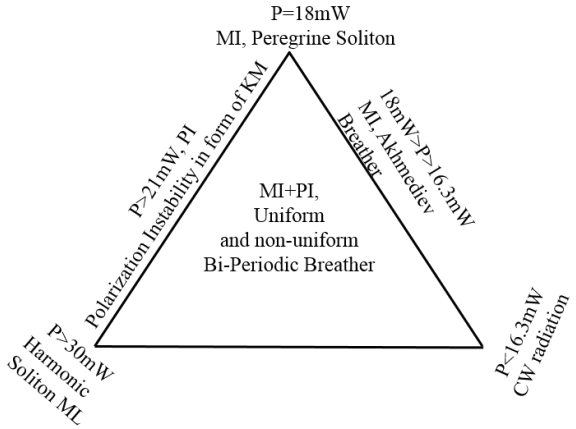

Fig. 4.25: Schematic representation of the interrelation between various RW emergence mechanisms.

Table 4.1: The observed optical BDRW patterns lifetimes and its likelihoods.

Pattern	Pump Power (mW)	Lifetime (round trips)	Bright Likelihood	Dark Likelihood	Mechanism
Akhmediev Breather	16.3	Thousands	~3.2×10^{-3},	~2.2×10^{-4}	Modulation Instability
Peregrine Breather	18	Hundreds	~3.67×10^{-4}	Nil	Modulation Instability
Uniform Bi-Periodic Breather	20	Hundreds	~2.68×10^{-2}	4×10^{-6}	Modulation and Polarization Instabilities
Non-uniform Bi-Periodic Breather	20	Hundreds	9.46×10^{-3}	Nil	Modulation and Polarization Instabilities
Polarization Incoherent Coupling	21.8	Hundreds	6.8×10^{-2}	8.4×10^{-4}	Polarization Instability
Polarization Incoherent Coupling	24.3	Hundreds	8.36×10^{-2}	1×10^{-4}	Polarization Instability
Polarization Incoherent Coupling	26.1	Hundreds	7.67×10^{-2}	2.1×10^{-5}	Polarization Instability
Polarization Incoherent Coupling	28	Hundreds	0.101	1.25×10^{-4}	Polarization Instability
Polarization Incoherent Coupling	29	Hundreds	7.46×10^{-2}	Nil	Polarization Instability

Chapter 5

Conclusions and Future Research

5.1: Conclusions

The field of nonlinear dynamics provides a good platform for the study and control of many interdisciplinary nonlinear natural phenomena; it gives a versatile and highly efficient theoretical framework that can be successful in developing an understanding of the basic features of mechanisms for generating RWs. The similarity of the propagation of water waves in the ocean system and light waves in optics systems has motivated researchers to study optical RWs in order to understand the giant waves that appear and disappear without a trace in the ocean. The close analogy between the two systems has been studied in detail both theoretically and numerically, hence, there is now the opportunity to study this natural phenomenon by means of testbed optical experiments. In particular, optical fibre systems offer great advantages in studying nonlinear dynamics because of the faster field evolution and hence the higher number of events that can be recorded. Therefore, experimental investigations have been carried out in a set of different optical systems including supercontinuum generation, Raman fibre amplifiers and lasers, and the mode-locked fibre laser. These experiments have stimulated the scientific community towards a better understanding of the RW generation mechanisms from modulation instability to soliton dissipative. Understanding the physics behind the emergence of optical RWs or intense pulses in fibre optics is crucial not only in the ocean system, but it can also be beneficial in data communication as well as offering a promising technique to generate localised intense and high output power levels in optical fibre for many applications.

Therefore, this dissertation has been devoted to an investigation of RW phenomena in optical fibre lasers. The experimental results illustrated in this thesis provide up-to-date experimental observations for the study of optical RW phenomenon and their statistics. It provides a testbed experimental system to study the optical RW emergence mechanisms

based on different instabilities such as multimode, chiral symmetry breaking, soliton rain, soliton fission, MI and polarization instabilities.

A brief discussion of the fundamental definitions and concepts of RWs were presented in the first chapter, focussing on RW emergence in the ocean; the criteria of the RW identification; followed by their emergence in different physical systems and different optical schematic systems. As well as soliton dissipative phenomenon, which is the key factor for RW generation, new types of the low threshold vector resonance multimode instability (VMMI) and chiral symmetry breaking (CSB) instabilities were explored in chapter 2 as an optical RW emergence mechanism. The desynchronization of the two orthogonal polarizations in optical fibres renders the fibre laser systems to operate in either VMMI or CSB modes and then become unstable, leading to the emerging the optical RWs. The effect of the PI have been investigated, the results of which confirmed that the PI in the optical fibres drives the laser to generate extreme waves. Therefore, both of these instabilities have been investigated in a long cavity (615m) fibre laser and realized using another fibre laser based on HiBi fibre for VMMI and spun fibre for CSB. Based on these instabilities, the testbed long cavity fibre laser has been studied with 19x19 positions of the intra-cavity and pump polarization controllers (polarization mapping). In terms of temporal classification, the observed optical RW events were classified into SORW and FORW based on the characteristic time of the autocorrelation function of the collected experimental data. Both of the SORW and FORW have been studied with polarization mapping. It was found that SORW events have a lifetime duration significantly longer than the decay time of the AF and it emerged as results of the polarization hopping between different attractors due to the incoherent coupling from the PI. This, indeed, could take place in both active and passive fibre through the polarization hole burning by means of polarization attractors. While FORW events have a lifetime duration shorter than the AF decay time; and emerged due to the results of pulse-pulse interaction and nonlinear pulses dynamics which placed in an active fibre due to nonlinearity induced by the inverse population as well as intrinsic nonlinearity in the passive part of the cavity. FORW patterns have been found in the form of lonely, twin, three sisters, crossing and accelerated pulses as well as some other RW patterns.

In the case of the formation of optical RWs that are associated with the soliton dissipative mechanism, low threshold soliton rain and soliton fission, as well as soliton interactions that led to the emergence of optical RWs have been presented in chapter 3. Using the SWCNT-SA passive mode-locked fibre laser testbed, by adjusting the pumping power and the intra-cavity birefringence, it was possible to control the appearance and disappearance of the soliton rain flow, harmonics soliton rain, soliton fission and soliton interactions that lead to the emergence of the optical RWs. These effects were all observed and investigated in chapter 3. The experimental observation of the temporal signature of soliton fission was also demonstrated in chapter 3. Clear soliton pulse fission signatures were obtained in

measurements of shot-to-shot intensity when the system is operating in a transition regime between soliton rain and chaotic emission. The spatiotemporal intensity measurements showed that soliton fission mainly occurred due to soliton interactions between co-propagating solitons with small temporal spacing, small frequency separation, and the appropriate phase difference between solitons. Also, the interaction processes between solitons inside the main pulse could be clearly captured and it was found that nonlinear soliton fission accounts for optical RW generation in this SWCNT-SA mode-locking fibre laser. This was also confirmed by the PDF statistics. Therefore, the fusion of optical solitons can be regarded as one of the mechanisms which generate optical RWs. The results showed that the fusion process is quite sensitive to the initial conditions of the pump power and intra-cavity birefringence. Strong internal modulation instability formed by intra-cavity birefringence, can trigger the laser pulse to explode into many pulses when the pump power is in the range for which fissions occur.

High HML in the same SWCNT-SA passive mode-locked fibre laser based on the acoustic-optic effect have also been demonstrated. Under different launched pump powers and appropriate adjustments of the polarization in the laser cavity, controllable HML from the first up to the 51st order has been obtained. High HML fibre lasers such as this are important in revealing the high-speed laser modulator, which is vital for fibre optic communications, all-optical clock recovery, frequency metrology and sensing applications.

In addition to pulse-pulse and soliton dissipative wave interactions mechanisms of the optical RWs emergence that are presented in chapter 2 and chapter 3 respectively, a new mechanism that is caused by the coherent coupling of the orthogonal SOP led to the emergence of a new type of bright-dark vector RWs. These waves appeared as a result of polarization instability as was demonstrated in chapter 4. In the first part of chapter 4, we studied the BDRWs that emerged as a result of MI that led to the brake up of the CW radiation into a train of pulses in the form of Akmedeive, Ma and bi-periodic breathers. This occurred when the pump power was within the first power group where it is below the PI threshold power. In the second part of chapter 4, the output laser pulses that accompany the BDRWs were studied. These arises due to the interaction between the desynchronized two orthogonal polarizations by PI when the pump power (second group) exceeds the power required to excite the PI. Therefore, incoherent coupling of the two orthogonal linear polarization components drove the laser cavity towards the emergence of vector BDRW events.

Therefore, the novelty obtained in this thesis is introduced new types instabilities (VMMI and CSB) that can drive the fibre laser to operate at a wide range of the laser dynamics including the RWs emergence. The second novelty that also obtained in this thesis is the observation for the first time the vector BDRWs in both of modulation and polarization instabilities at low pump powers. These novelties as well as the other results that presented

in this thesis have a scientific impact to pave the way to unlocking the universal nature of the emergence the RWs and so can be of interest to a broad scientific community. Also, this research can lead to new methods to generate high intensity laser pulses; an analysis of optical fibre parametric amplifiers; generate ultrafast soliton based all-optical switches and logic devices; and can improve the design of broadband supercontinuum sources.

For all of the observed optical RWs in the three experimental chapters, the long-term wave time series and the spatiotemporal dynamics for pulse-pulse, solitons interactions, MI and PI were characterized for further understanding as well as confirming the optical RW emergence mechanism. It also provides an improved understanding of the localised structures which emerge due to MI. The PDF statistical analysis of the collected data during all experiments has also confirmed the association of statistical L shape RWs exclusively to the multi-pulsing and bi-periodic breather patterns.

The role of PI (vector) effects on the formation of optical RWs is highlighted in this thesis in relation to the debate on whether polarization can be ignored or as an absolute requirement for the generation of the optical RWs events that also appeared with a probability much higher than predicted by Rayleigh or Gaussian distributions. Based on both, MMVI and CSB as well as PI, we have shown that optical RWs can be formed by both MI and PI. As MI, the PI effects also play an important role in the formation of optical RWs. These two instabilities effects can either act separately or interact in a certain way, depended on the laser configuration and the pump power level.

The main strength of these testbeds laser experiments is the possibility to precisely control the conditions and the parameters of optical RW emergence, as well as the availability of advanced data analysing techniques that permit extensive and fast optical RW statistical characterization. These results can be useful to direct or enhance the progress in other scientific areas, as well as promote the technology towards high power fibre laser for a wide range of applications.

Nevertheless, there are still many other optical experiments can be explored in the optical RW emergence for further understanding of the mechanisms operating in the optical system.

5.2: Future Research

We propose some recommendations for future work, which can be realised in the near future. Optical RW studies in both HiBi and spun fibre experiments can be performed for further observation of vector optical RWs. Optical RW machine learning could be another promising area, as this could provide real-time analysis for the emerged optical RW events and perhaps lead to predictions. In addition, an investigation of localized pulses aimed at high power generation in fibres laser should be investigated as RWs represent a promising technique for this.

References

[1] L. Draper, "'FREAK' OCEAN WAVES," *Weather,* vol. 21, pp. 2-4, 1966.

[2] S. Haver, "A possible freak wave event measured at the Draupner Jacket January 1 1995," *Rogue waves,* pp. 1-8, 2004.

[3] N. Akhmediev, A. Ankiewicz, and M. Taki, "Waves that appear from nowhere and disappear without a trace," *Physics Letters A,* vol. 373, pp. 675-678, 2009.

[4] P. C. Liu, "A chronology of freauqe wave encounters," *Geofizika,* vol. 24, pp. 57-70, 2007.

[5] G. Lawton, "Monsters of the deep," *New Scientist,* vol. 170, pp. 28-32, 2001.

[6] I. Lavrenov, "Mathematical modeling of wind waves in spatial inhomogeneous ocean," *St. Petersburg, PH Gidrometeoizdat,* 1998.

[7] I. Lavrenov, "The wave energy concentration at the Agulhas current off South Africa," *Natural hazards,* vol. 17, pp. 117-127, 1998.

[8] I. Nikolkina and I. Didenkulova, "Rogue waves in 2006–2010," *Natural hazards and Earth system sciences,* vol. 11, pp. 2913-2924, 2011.

[9] C. Kharif and E. Pelinovsky, "Physical mechanisms of the rogue wave phenomenon," *European Journal of Mechanics-B/Fluids,* vol. 22, pp. 603-634, 2003.

[10] C. Garrett and J. Gemmrich, "Rogue waves," *Phys. Today,* vol. 62, p. 62, 2009.

[11] N. Akhmediev, J. Soto-Crespo, and A. Ankiewicz, "Could rogue waves be used as efficient weapons against enemy ships?," *The European Physical Journal Special Topics,* vol. 185, pp. 259-266, 2010.

[12] E. Pelinovsky and C. Kharif, *Extreme ocean waves*: Springer, 2008.

[13] M. Hopkin, "Sea snapshots will map frequency of freak waves," ed: Nature Publishing Group, 2004.

[14] S. Perkins, "Dashing rogues: Freak ocean waves pose threat to ships, deep-sea oil platforms," *Science News,* vol. 170, pp. 328-329, 2006.

[15] W. J. Broad, "Rogue giants at sea," *The New York Times,* vol. 11, 2006.

[16] A. Hadjihosseini, J. Peinke, and N. Hoffmann, "Stochastic analysis of ocean wave states with and without rogue waves," *New Journal of Physics,* vol. 16, p. 053037, 2014.

[17] V. Ruban, Y. Kodama, M. Ruderman, J. Dudley, R. Grimshaw, P. McClintock, C. Kharif, E. Pelinovsky, T. Soomere, G. Lindgren, N. Akhmediev, A Slunyaev, D. Solli, C. Ropers, B. Jalali, F. Dias, A. Osborne, "Rogue waves–towards a unifying concept?: Discussions and debates," *The European physical journal special topics,* vol. 185, pp. 5-15, 2010.

[18] C. Bonatto, M. Feyereisen, S. Barland, M. Giudici, C. Masoller, J. R. R. Leite and J. R. Tredicce, "Deterministic optical rogue waves," *Physical review letters,* vol. 107, p. 053901, 2011.

[19] C. Kharif, E. Pelinovsky, and A. Slunyaev, "Introduction," in *Rogue Waves in the Ocean*, ed: Springer, 2009, pp. 1-10.

[20] M. Onorato, S. Residori, U. Bortolozzo, A. Montina, and F. Arecchi, "Rogue waves and their generating mechanisms in different physical contexts," *Physics Reports,* vol. 528, pp. 47-89, 2013.

[21] D. Solli, C. Ropers, and B. Jalali, "Active control of rogue waves for stimulated supercontinuum generation," *Physical review letters,* vol. 101, p. 233902, 2008.

[22] C. Lafargue, J. Bolger, G. Genty, F. Dias, J. Dudley, and B. Eggleton, "Direct detection of optical rogue wave energy statistics in supercontinuum generation," *Electronics Letters,* vol. 45, pp. 217-219, 2009.

[23] D. Peregrine, "Water waves, nonlinear Schrödinger equations and their solutions," *The ANZIAM Journal,* vol. 25, pp. 16-43, 1983.

[24] Y. C. Ma, "The Perturbed Plane-Wave Solutions of the Cubic Schrödinger Equation," *Studies in Applied Mathematics,* vol. 60, pp. 43-58, 1979.

[25] N. Akhmediev, V. Eleonskii, and N. Kulagin, "Exact first-order solutions of the nonlinear Schrödinger equation," *Theoretical and mathematical physics,* vol. 72, pp. 809-818, 1987.

[26] B. Kibler, J. Fatome, C. Finot, G. Millot, F. Dias, G. Genty, N. Akhmediev and J. M. Dudley, "The Peregrine soliton in nonlinear fibre optics," *Nature Physics,* vol. 6, p. 790, 2010.

[27] D. Solli, C. Ropers, P. Koonath, and B. Jalali, "Optical rogue waves," *Nature,* vol. 450, p. 1054, 2007.

[28] M. Shats, H. Punzmann, and H. Xia, "Capillary rogue waves," *Physical review letters,* vol. 104, p. 104503, 2010.

[29] Y. Zhen-Ya, "Financial rogue waves," *Communications in Theoretical Physics,* vol. 54, p. 947, 2010.

[30] Z. Jie-Fang, J. Mei-Zhen, H. Ji-Da, L. Ji-Hui, and D. Chao-Qing, "Dynamics of optical rogue waves in inhomogeneous nonlinear waveguides," *Chinese Physics B,* vol. 22, p. 054208, 2013.
[31] H. Bailung, S. Sharma, and Y. Nakamura, "Observation of Peregrine solitons in a multicomponent plasma with negative ions," *Physical review letters,* vol. 107, p. 255005, 2011.
[32] S. Wabnitz , *Nonlinear Guided Wave Optics A testbed for extreme waves*, Bristol, IOP, 2017. Available: http://dx.doi.org/10.1088/978-0-7503-1460-2.
[33] J. M. Dudley, F. Dias, M. Erkintalo, and G. Genty, "Instabilities, breathers and rogue waves in optics," *Nature Photonics,* vol. 8, pp. 755-764, 2014.
[34] N. Akhmediev, B. Kibler, F. Baronio, M. Belić, W.-P. Zhong, Y. Zhang*, et al.*, "Roadmap on optical rogue waves and extreme events," *Journal of Optics,* vol. 18, p. 063001, 2016.
[35] N. Akhmediev, J. M. Dudley, D. Solli, and S. Turitsyn, "Recent progress in investigating optical rogue waves," *Journal of Optics,* vol. 15, p. 060201, 2013.
[36] M. Onorato, A. R. Osborne, M. Serio, and S. Bertone, "Freak waves in random oceanic sea states," *Physical Review Letters,* vol. 86, p. 5831, 2001.
[37] A. Montina, U. Bortolozzo, S. Residori, and F. Arecchi, "Non-Gaussian statistics and extreme waves in a nonlinear optical cavity," *Physical review letters,* vol. 103, p. 173901, 2009.
[38] K. Hammani, C. Finot, J. M. Dudley, and G. Millot, "Optical rogue-wave-like extreme value fluctuations in fiber Raman amplifiers," *Optics express,* vol. 16, pp. 16467-16474, 2008.
[39] N. Tarasov, S. Sugavanam, and D. Churkin, "Spatio-temporal generation regimes in quasi-CW Raman fiber lasers," *Optics express,* vol. 23, pp. 24189-24194, 2015.
[40] A. N. Pisarchik, R. Jaimes-Reátegui, R. Sevilla-Escoboza, G. Huerta-Cuellar, and M. Taki, "Rogue waves in a multistable system," *Physical Review Letters,* vol. 107, p. 274101, 2011.
[41] C. Lecaplain, P. Grelu, J. Soto-Crespo, and N. Akhmediev, "Dissipative rogue waves generated by chaotic pulse bunching in a mode-locked laser," *Physical review letters,* vol. 108, p. 233901, 2012.
[42] A. Demircan, S. Amiranashvili, C. Brée, C. Mahnke, F. Mitschke, and G. Steinmeyer, "Rogue wave formation by accelerated solitons at an optical event horizon," *Applied Physics B,* vol. 115, pp. 343-354, 2014.
[43] K. Hammani, C. Finot, and G. Millot, "Emergence of extreme events in fiber-based parametric processes driven by a partially incoherent pump wave," *Optics letters,* vol. 34, pp. 1138-1140, 2009.
[44] K. Hammani, C. Finot, B. Kibler, and G. Millot, "Soliton generation and rogue-wave-like behavior through fourth-order scalar modulation instability," *IEEE Photonics Journal,* vol. 1, pp. 205-212, 2009.
[45] F. Arecchi, U. Bortolozzo, A. Montina, and S. Residori, "Granularity and inhomogeneity are the joint generators of optical rogue waves," *Physical review letters,* vol. 106, p. 153901, 2011.
[46] M. G. Kovalsky, A. A. Hnilo, and J. R. Tredicce, "Extreme events in the Ti: sapphire laser," *Optics letters,* vol. 36, pp. 4449-4451, 2011.
[47] J. Soto-Crespo, P. Grelu, and N. Akhmediev, "Dissipative rogue waves: extreme pulses generated by passively mode-locked lasers," *Physical Review E,* vol. 84, p. 016604, 2011.
[48] A. Zaviyalov, O. Egorov, R. Iliew, and F. Lederer, "Rogue waves in mode-locked fiber lasers," *Physical Review A,* vol. 85, p. 013828, 2012.
[49] A. F. Runge, C. Aguergaray, N. G. Broderick, and M. Erkintalo, "Raman rogue waves in a partially mode-locked fiber laser," *Optics letters,* vol. 39, pp. 319-322, 2014.
[50] J. M. Dudley, G. Genty, F. Dias, B. Kibler, and N. Akhmediev, "Modulation instability, Akhmediev Breathers and continuous wave supercontinuum generation," *Optics express,* vol. 17, pp. 21497-21508, 2009.
[51] B. Kibler, C. Finot, and J. M. Dudley, "Soliton and rogue wave statistics in supercontinuum generation in photonic crystal fibre with two zero dispersion wavelengths," *The European Physical Journal Special Topics,* vol. 173, pp. 289-295, 2009.
[52] J. M. Dudley, G. Genty, and B. J. Eggleton, "Harnessing and control of optical rogue waves in supercontinuum generation," *Optics Express,* vol. 16, pp. 3644-3651, 2008.
[53] A. Mussot, A. Kudlinski, M. Kolobov, E. Louvergneaux, M. Douay, and M. Taki, "Observation of extreme temporal events in CW-pumped supercontinuum," *Optics express,* vol. 17, pp. 17010-17015, 2009.
[54] C. Finot, K. Hammani, J. Fatome, J. M. Dudley, and G. Millot, "Selection of extreme events generated in Raman fiber amplifiers through spectral offset filtering," *IEEE Journal of Quantum Electronics,* vol. 46, pp. 205-213, 2010.

[55] L.-C. Zhao and J. Liu, "Localized nonlinear waves in a two-mode nonlinear fiber," *JOSA B,* vol. 29, pp. 3119-3127, 2012.
[56] D. V. Churkin, O. A. Gorbunov, and S. V. Smirnov, "Extreme value statistics in Raman fiber lasers," *Optics letters,* vol. 36, pp. 3617-3619, 2011.
[57] P.-H. Hanzard, M. Talbi, D. Mallek, A. Kellou, H. Leblond, F. Sanchez*, et al.*, "Brillouin scattering-induced rogue waves in self-pulsing fiber lasers," *Scientific Reports,* vol. 7, p. 45868, 2017.
[58] K. Schires, A. Hurtado, I. D. Henning, and M. Adams, "Rare disruptive events in polarisation-resolved dynamics of optically injected 1550 nm VCSELs," *Electronics letters,* vol. 48, pp. 872-874, 2012.
[59] K. Tai, A. Hasegawa, and A. Tomita, "Observation of modulational instability in optical fibers," *Physical review letters,* vol. 56, p. 135, 1986.
[60] A. Sauter, S. Pitois, G. Millot, and A. Picozzi, "Incoherent modulation instability in instantaneous nonlinear Kerr media," *Optics letters,* vol. 30, pp. 2143-2145, 2005.
[61] J. Burzlaff, "On the Generation of Optical Solitons," in *Proceedings of the Fourth European Conference on Mathematics in Industry*, 1991, pp. 219-223.
[62] A. Picozzi, M. Haelterman, S. Pitois, and G. Millot, "Incoherent solitons in instantaneous response nonlinear media," *Physical review letters,* vol. 92, p. 143906, 2004.
[63] J. M. Dudley, C. Finot, D. J. Richardson, and G. Millot, "Self-similarity in ultrafast nonlinear optics," *Nature Physics,* vol. 3, p. 597, 2007.
[64] A. Berkhoer and V. Zakharov, "Self excitation of waves with different polarizations in nonlinear media," *Soviet Journal of Experimental and Theoretical Physics,* vol. 31, p. 486, 1970.
[65] P. Grelu and N. Akhmediev, "Dissipative solitons for mode-locked lasers," *Nature Photonics,* vol. 6, p. 84, 2012.
[66] C. Xu and F. Wise, "Recent advances in fibre lasers for nonlinear microscopy," *Nature photonics,* vol. 7, pp. 875-882, 2013.
[67] M. E. Fermann and I. Hartl, "Ultrafast fibre lasers," *Nature photonics,* vol. 7, p. 868, 2013.
[68] S. Chouli and P. Grelu, "Soliton rains in a fiber laser: An experimental study," *Physical Review A,* vol. 81, p. 063829, 2010.
[69] J. M. Dudley, C. Finot, G. Millot, J. Garnier, G. Genty, D. Agafontsev*, et al.*, "Extreme events in optics: Challenges of the MANUREVA project," *The European Physical Journal Special Topics,* vol. 185, pp. 125-133, 2010.
[70] B.-L. Guo and L.-M. Ling, "Rogue wave, breathers and bright-dark-rogue solutions for the coupled Schrödinger equations," *Chinese Physics Letters,* vol. 28, pp. 110202-110202, 2011.
[71] B. Frisquet, B. Kibler, P. Morin, F. Baronio, M. Conforti, G. Millot*, et al.*, "Optical dark rogue wave," *Scientific reports,* vol. 6, p. 20785, 2016.
[72] F. Baronio, A. Degasperis, M. Conforti, and S. Wabnitz, "Solutions of the vector nonlinear Schrödinger equations: evidence for deterministic rogue waves," *Physical review letters,* vol. 109, p. 044102, 2012.
[73] L.-C. Zhao and J. Liu, "Rogue-wave solutions of a three-component coupled nonlinear Schrödinger equation," *Physical Review E,* vol. 87, p. 013201, 2013.
[74] C. Lecaplain, P. Grelu, J. M. Soto-Crespo, and N. Akhmediev, "Dissipative Rogue Waves Generated by Chaotic Pulse Bunching in a Mode-Locked Laser," *Physical Review Letters,* vol. 108, p. 233901, 2012.
[75] S. V. Sergeyev, H. Kbashi, N. Tarasov, Y. Loiko, and S. A. Kolpakov, "Vector-Resonance-Multimode Instability," *Physical Review Letters,* vol. 118, p. 033904, 2017.
[76] S. Kolpakov, H. Kbashi, and S. Sergeyev, "Dynamics of vector rogue waves in a fiber laser with a ring cavity," *Optica,* vol. 3, pp. 870-875, 2016.
[77] S. Kolpakov, H. Kbashi, and S. Sergeyev, "Slow optical rogue waves in a unidirectional fiber laser," in *CLEO: QELS_Fundamental Science*, 2016, p. JW2A. 56.
[78] H. Kbashi, S. A. Kolpakov, and S. V. Sergeyev, "Temporal scaling of optical rogue waves in unidirectional ring fiber laser," in *2016 18th International Conference on Transparent Optical Networks (ICTON)*, 2016, pp. 1-4.
[79] V. Ruban, Y. Kodama, M. Ruderman, J. Dudley, R. Grimshaw, P. V. E. McClintock*, et al.*, "Rogue waves – towards a unifying concept?: Discussions and debates," *The European Physical Journal Special Topics,* vol. 185, pp. 5-15, July 01 2010.
[80] G. Huerta-Cuellar, A. N. Pisarchik, and Y. O. Barmenkov, "Experimental characterization of hopping dynamics in a multistable fiber laser," *Physical Review E,* vol. 78, p. 035202, 2008.
[81] P. A. E. M. Janssen, "Nonlinear Four-Wave Interactions and Freak Waves," *Journal of Physical Oceanography,* vol. 33, pp. 863-884, 2003.

[82] H. T. Wist, D. Myrhaug, and H. Rue, "Statistical properties of successive wave heights and successive wave periods," *Applied Ocean Research,* vol. 26, pp. 114-136, 2004.
[83] P. Rohrmann, A. Hause, and F. Mitschke, "Solitons Beyond Binary: Possibility of Fibre-Optic Transmission of Two Bits per Clock Period," *Scientific Reports,* vol. 2, p. 866, 2012.
[84] J. P. Gordon, "Interaction forces among solitons in optical fibers," *Optics Letters,* vol. 8, pp. 596-598, 1983.
[85] F. M. Mitschke and L. F. Mollenauer, "Experimental observation of interaction forces between solitons in optical fibers," *Optics Letters,* vol. 12, pp. 355-357, 1987.
[86] A. Antikainen, M. Erkintalo, J. M. Dudley, and G. Genty, "On the phase-dependent manifestation of optical rogue waves," *Nonlinearity,* vol. 25, p. R73, 2012.
[87] R. Driben and I. Babushkin, "Accelerated rogue waves generated by soliton fusion at the advanced stage of supercontinuum formation in photonic-crystal fibers," *Optics Letters,* vol. 37, p. 5157, 2012.
[88] T. Udem, R. Holzwarth, and T. W. Hansch, "Optical frequency metrology," *Nature,* vol. 416, pp. 233-237, 2002.
[89] B. Oktem, C. Ülgüdür, and F. Ö. Ilday, "Soliton–similariton fibre laser," *Nature Photonics,* vol. 4, p. 307, 2010.
[90] D. Hillerkuss, R. Schmogrow, T. Schellinger, M. Jordan, M. Winter, G. Huber*, et al.*, "26 Tbit s−1 line-rate super-channel transmission utilizing all-optical fast Fourier transform processing," *Nature Photonics,* vol. 5, p. 364, 2011.
[91] A. Yadav, H. Kbashi, S. Kolpakov, N. Gordon, K. Zhou, and E. U. Rafailov, "Stealth dicing of sapphire wafers with near infra-red femtosecond pulses," *Applied Physics A,* vol. 123, p. 369, 2017.
[92] T. M. Fortier, M. S. Kirchner, F. Quinlan, J. Taylor, J. Bergquist, T. Rosenband*, et al.*, "Generation of ultrastable microwaves via optical frequency division," *Nature Photonics,* vol. 5, pp. 425-429, 2011.
[93] M. L. Dennis, M. A. Putnam, J. U. Kang, T.-E. Tsai, I. N. Duling, and E. J. Friebele, "Grating sensor array demodulation by use of a passively mode-locked fiber laser," *Optics Letters,* vol. 22, pp. 1362-1364, 1997.
[94] W. Sibbett, A. A. Lagatsky, and C. T. A. Brown, "The development and application of femtosecond laser systems," *Optics Express,* vol. 20, pp. 6989-7001, 2012.
[95] F. Li, P. K. A. Wai, and J. N. Kutz, "Geometrical description of the onset of multi-pulsing in mode-locked laser cavities," *Journal of the Optical Society of America B,* vol. 27, pp. 2068-2077, 2010.
[96] Z. X. Zhang, L. Zhan, X. X. Yang, S. Y. Luo, and Y. X. Xia, "Passive harmonically mode-locked erbium-doped fiber laser with scalable repetition rate up to 1.2 GHz," *Laser Physics Letters,* vol. 4, pp. 592-596, 2007.
[97] F. Amrani, A. Haboucha, M. Salhi, H. Leblond, A. Komarov, P. Grelu*, ,* F. Sanchez, "Passively mode-locked erbium-doped double-clad fiber laser operating at the 322nd harmonic," *Optics Letters,* vol. 34, pp. 2120-2122, 2009.
[98] W. Tianxing, Z. Yan, C. Mou, K. Zhou, and L. Zhang, "2.2 GHz mode locked all-fiber Erbium doped laser based on a tilted fiber grating," in *2016 15th International Conference on Optical Communications and Networks (ICOCN)*, 2016, pp. 1-3, 2016.
[99] H.-R. Chen, K.-H. Lin, C.-Y. Tsai, H.-H. Wu, C.-H. Wu, CH. Chen,YC Chi, GR Lin and WF Hsieh, "12 GHz passive harmonic mode-locking in a 1.06 μm semiconductor optical amplifier-based fiber laser with figure-eight cavity configuration," *Optics Letters,* vol. 38, pp. 845-847, 2013.
[100] S. Y. Set, H. Yaguchi, Y. Tanaka, and M. Jablonski, "Laser Mode Locking Using a Saturable Absorber Incorporating Carbon Nanotubes," *Journal of Lightwave Technology,* vol. 22, p. 51, 2004.
[101] F. Wang, A. G. Rozhin, V. Scardaci, Z. Sun, F. Hennrich, I. H. White, W. I . Milne and A. C. Ferrari, "Wideband-tuneable, nanotube mode-locked, fibre laser," *Nat Nano,* vol. 3, pp. 738-742, 2008.
[102] Z. Sun, T. Hasan, F. Torrisi, D. Popa, G. Privitera, F. Wang*, et al.*, "Graphene Mode-Locked Ultrafast Laser," *ACS Nano,* vol. 4, pp. 803-810, 2010.
[103] X. Li, W. Zou, and J. Chen, "Passive harmonic hybrid mode-locked fiber laser with extremely broad spectrum," *Optics Express,* vol. 23, pp. 21424-21433, 2015.
[104] C. S. Jun, S. Y. Choi, F. Rotermund, B. Y. Kim, and D.-I. Yeom, "Toward higher-order passive harmonic mode-locking of a soliton fiber laser," *Optics Letters,* vol. 37, pp. 1862-1864, 2012.

[105] C. S. Jun, J. H. Im, S. H. Yoo, S. Y. Choi, F. Rotermund, D.-I. Yeom*, et al.*, "Low noise GHz passive harmonic mode-locking of soliton fiber laser using evanescent wave interaction with carbon nanotubes," *Optics Express,* vol. 19, pp. 19775-19780, 2011.
[106] C. Mou, R. Arif, A. Rozhin, and S. Turitsyn, "Passively harmonic mode locked erbium doped fiber soliton laser with carbon nanotubes based saturable absorber," *Optical Materials Express,* vol. 2, pp. 884-890, 2012.
[107] K. K. Chow, "Low pump threshold CVD graphene based passively harmonic mode-locked fibre laser," *Electronics Letters 53 (5),* 330-331, 2017.
[108] J. Sotor, G. Sobon, W. Macherzynski, and K. M. Abramski, "Harmonically mode-locked Er-doped fiber laser based on a Sb 2 Te 3 topological insulator saturable absorber," *Laser Physics Letters,* vol. 11, p. 055102, 2014.
[109] Z.-C. Luo, M. Liu, H. Liu, X.-W. Zheng, A.-P. Luo, C.-J. Zhao, H. Zhang, Sh. Wen and Ch. Xu, "2GHz passively harmonic mode-locked fiber laser by a microfiber-based topological insulator saturable absorber," *Optics Letters,* vol. 38, pp. 5212-5215, 2013.
[110] L. Junsu, P. June, K. Joonhoi, J. Young Min, and L. Ju Han, "Harmonically mode-locked femtosecond fiber laser using non-uniform, WS2 -particle deposited side-polished fiber," *Journal of Optics,* vol. 18, p. 035502, 2016.
[111] Y.-C. Chen, N. R. Raravikar, L. S. Schadler, P. M. Ajayan, Y.-P. Zhao, T.-M. Lu, G. C. Wang and C. C. Zhang, "Ultrafast optical switching properties of single-wall carbon nanotube polymer composites at 1.55 μm," *Applied Physics Letters,* vol. 81, pp. 975-977, 2002.
[112] S. Y. Set, H. Yaguchi, Y. Tanaka, and M. Jablonski, "Ultrafast fiber pulsed lasers incorporating carbon nanotubes," *IEEE Journal of Selected Topics in Quantum Electronics,* vol. 10, pp. 137-146, 2004.
[113] Z. Sun, A. G. Rozhin, F. Wang, T. Hasan, D. Popa, W. O'Neill, and A. C. Ferrari, "A compact, high power, ultrafast laser mode-locked by carbon nanotubes," *Applied Physics Letters,* vol. 95, p. 253102, 2009.
[114] E. J. R. Kelleher, J. C. Travers, Z. Sun, A. G. Rozhin, A. C. Ferrari, S. V. Popov and J R. Taylor, "Nanosecond-pulse fiber lasers mode-locked with nanotubes," *Applied Physics Letters,* vol. 95, p. 111108, 2009.
[115] X. Zhao, Z. Zheng, L. Liu, Y. Liu, Y. Jiang, X. Yang and J. Zhu, "Switchable, dual-wavelength passively mode-locked ultrafast fiber laser based on a single-wall carbon nanotube modelocker and intracavity loss tuning," *Optics Express,* vol. 19, pp. 1168-1173, 2011.
[116] K. Jiang, S. Fu, P. Shum, and C. Lin, "A Wavelength-Switchable Passively Harmonically Mode-Locked Fiber Laser With Low Pumping Threshold Using Single-Walled Carbon Nanotubes," *IEEE Photonics Technology Letters,* vol. 22, pp. 754-756, 2010.
[117] T. B. Benjamin, F. R. S., "Instability of periodic wavetrains in nonlinear dispersive systems," *Proceedings of the Royal Society of London. Series A. Mathematical and Physical Sciences,* vol. 299, pp. 59-76, 1967.
[118] T. B. Benjamin and J. E. Feir, "The disintegration of wave trains on deep water Part 1. Theory," *Journal of Fluid Mechanics,* vol. 27, pp. 417-430, 2006.
[119] L. Ostrovskii, "Propagation of Wave Packets and Space-time Self-focusing in a Nonlinear Medium," *Soviet Journal of Experimental and Theoretical Physics,* vol. 24, p. 797, 1967.
[120] V. Bespalov and V. Talanov, "Filamentary structure of light beams in nonlinear liquids," *ZhETF Pisma Redaktsiiu,* vol. 3, p. 471, 1966.
[121] V. Karpman, "Self-modulation of nonlinear plane waves in dispersive media," *Soviet Journal of Experimental and Theoretical Physics Letters,* vol. 6, p. 277, 1967.
[122] T. Taniuti and H. Washimi, "Self-trapping and instability of hydromagnetic waves along the magnetic field in a cold plasma," *Physical Review Letters,* vol. 21, p. 209, 1968.
[123] C. K. Tam, "Amplitude dispersion and nonlinear instability of whistlers," *The Physics of Fluids,* vol. 12, pp. 1028-1035, 1969.
[124] A. Hasegawa, "Observation of Self-Trapping Instability of a Plasma Cyclotron Wave in a Computer Experiment," *Physical Review Letters,* vol. 24, pp. 1165-1168, 1970.
[125] S. Chen, P. Grelu, and J. Soto-Crespo, "Dark-and bright-rogue-wave solutions for media with long-wave–short-wave resonance," *Physical Review E,* vol. 89, p. 011201, 2014.
[126] S. V. Sergeyev, "Vector self-pulsing in erbium-doped fiber lasers," *Optics letters,* vol. 41, pp. 4700-4703, 2016.
[127] N. Akhmediev, J. M. Soto-Crespo, and A. Ankiewicz, "Extreme waves that appear from nowhere: on the nature of rogue waves," *Physics Letters A,* vol. 373, pp. 2137-2145, 2009.